

Device Architecture Engineering: Progress toward Next Generation Perovskite Solar Cells

Thomas Webb, Stephen J. Sweeney, and Wei Zhang*

Over the past decade, perovskite solar cells (PSCs) have quickly established themselves as a promising technology boasting both high efficiency and low processing costs. The rapid development and success of PSCs is a product of substantial research effort addressing compositional engineering, thin film fabrication, surface passivation, and interfacial treatments. Recently, engineering of device architecture has entered a renaissance with the emergence of several new bulk and graded heterojunction structures. These structures promote a lateral approach to the development of single-junction PSCs affording new opportunities in light management, defect passivation, carrier extraction, and long-term stability. Following a short overview of the historic evolution of PSC architectures, a detailed discussion of the promising progress of the recently reported perovskite bulk heterojunction and graded heterojunction approaches are offered. To enable better understanding of these novel architectures, a range of approaches to characterizing the architectures are presented. Finally, an outlook and perspective are provided offering insights into the future development of PSC architecture engineering.

witnessed over the last half century has encouraged the integration of solar technologies into both domestic and consumer electronics in addition to larger scale solar farms. It is therefore key that research continues to develop new highly efficient and inexpensive solar technologies.

Over the past decade, metal halide perovskites have emerged as a promising light harvesting material capable of increasing PCEs beyond that of conventional silicon solar cells, while remaining low cost and scalable.^[1,2] Metal halide perovskites adopt a formula of ABX_3 , where A is a small monovalent cation, such as methylammonium (MA^+) or formamidinium (FA^+), the B site is occupied by a metal cation such as Pb^{2+} , Sn^{2+} , or Ge^{2+} and the X site consists of a halide anion (Cl^- , Br^- , or I^-). The ability to produce various non-stoichiometric combinations of all three sites, imparts a high

1. Introduction


Developing low cost and efficient renewable energy sources to alleviate society's dependence on a finite supply of fossil fuels is arguably the biggest challenge of the century. Amongst a wave of emerging sustainable energy sources, solar power has stood out as a front-runner owing to the abundance of solar energy incident on the planet combined with minimal environmental impact associated with its collection. Furthermore, the rapid fall in manufacturing costs of photovoltaic (PV) technologies

degree of tunability over the perovskite band structure, ideal for matching with the solar spectrum and use in tandem applications.^[3] Moreover, solution processable perovskites exhibit a number of additional desirable optoelectronic properties such as high absorption coefficients, long diffusion lengths and a high tolerance to defects.^[4,5] Nevertheless, the performance of PSCs continues to fall short of the Shockley–Queisser (S–Q) limit. Additionally, poor stability remains a key practical limitation requiring further addressing.

Innovating and engineering of device architecture has historically played a significant role in addressing the aforementioned issues. The architectural evolution of the perovskite solar cells began in early 2009 when Kojima et al. reported intriguing synthetic organic-inorganic hybrid perovskite nanocrystals. These nanocrystals, it was found, could be used as an alternative light harvester/sensitizer in an architecture analogous to liquid electrolyte dye sensitized solar cells (DSSC) (Figure 1a). In the early work a dispersion of perovskite nanocrystals was synthesized through the combination of lead iodide and either methylammonium iodide or bromide (MAI/MABr). The fabrication of the nanocrystals was followed by spin coating the dispersion onto a mesoporous (mp)- TiO_2 electron transporting layer (ETL) scaffold. An iodide-triiodide (I^-/I_3^-) liquid electrolyte redox couple was used to facilitate hole extraction.^[6] The resultant perovskite sensitized, liquid electrolyte based solar cells showed promising light harvesting capabilities and carrier extraction dynamics enabling devices with power conversion efficiencies (PCEs) reaching 3.8%.^[6] The PCE was later improved to 6.5% using a

T. Webb, Dr. W. Zhang
Advanced Technology Institute
Department of Electrical and Electronic Engineering
University of Surrey
Guildford, Surrey GU2 7XH, UK
E-mail: wz0003@surrey.ac.uk

Prof. S. J. Sweeney
Advanced Technology Institute and Department of Physics
University of Surrey
Guildford, Surrey GU2 7XH, UK

 The ORCID identification number(s) for the author(s) of this article can be found under <https://doi.org/10.1002/adfm.202103121>.

© 2021 The Authors. Advanced Functional Materials published by Wiley-VCH GmbH. This is an open access article under the terms of the Creative Commons Attribution License, which permits use, distribution and reproduction in any medium, provided the original work is properly cited.

DOI: 10.1002/adfm.202103121

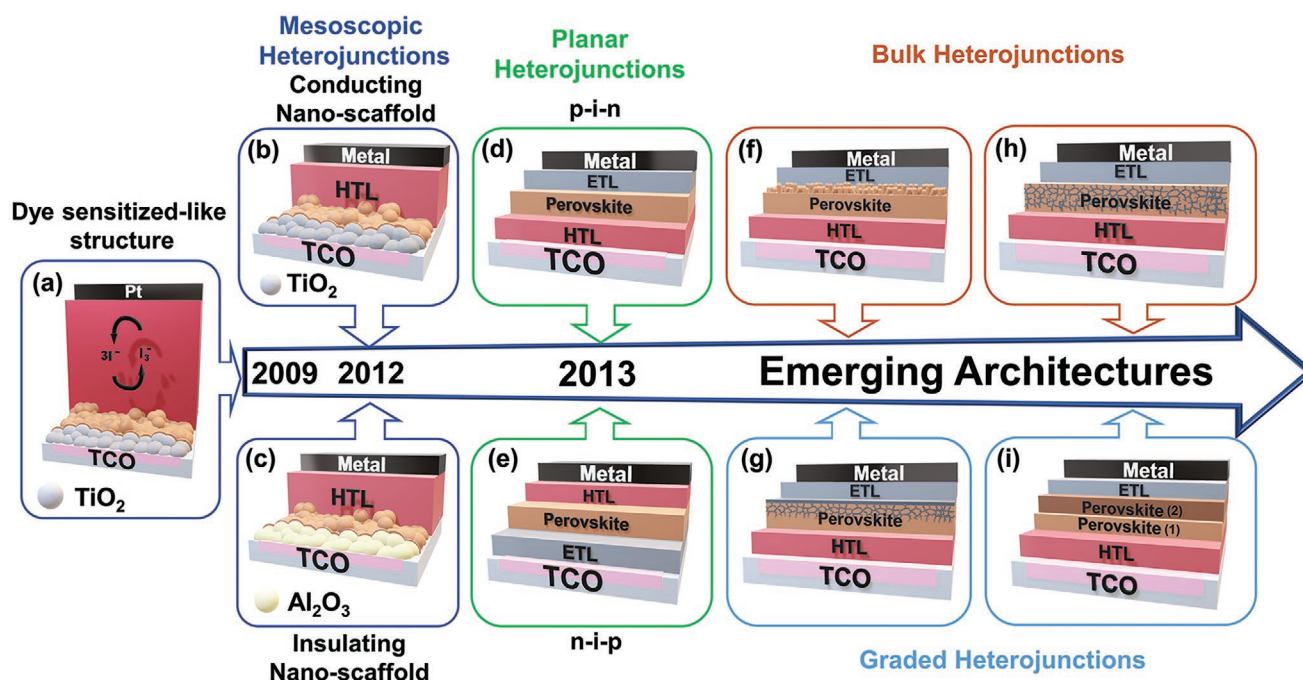


Figure 1. Timeline of the perovskite solar cell development from traditional to emerging architectures: a–e) Traditional perovskite photovoltaic architectures: a) First reported perovskite solar cell with an architecture adapted from DSSC technologies. b,c) mesoscopic structured solar cells using a solid-state HTL with the perovskite deposited on a mesoporous TiO_2 or Al_2O_3 layer, respectively. d,e) Planar heterojunction architectures in a n-i-p and p-i-n configuration, respectively. f–i) Emerging device architectures: f) nanostructured BHJ, g) perovskite: CTL BHJ, h) perovskite: CTL GHJ, i) perovskite: perovskite GHJ.

similar device architecture and an impressive external quantum efficiency (EQE) approaching 80% was recorded.^[7] The downfall of the promising early DSSC-based architecture, originated from the rapid dissolution of perovskite within the corrosive iodide based electrolyte limiting shelf life to mere minutes.^[6,7]

A key breakthrough in both the stability and PCEs of the early perovskite sensitized solar cells came from the replacement of the liquid electrolyte with the solid-state hole transport layer (HTL) 2,2',7,7'-Tetrakis[N,N-di(4-methoxyphenyl)amino]-9,9'-spirobifluorene (Spiro-OMeTAD), a material widely used in solid-state dye sensitized solar cells (Figure 1b).^[5,8,9] The transition to fully solid-state perovskite solar cells (PSCs) enabled Kim et al. to further increase the PCEs up to 9.7%, while the stability and shelf life was improved beyond 500 h in ambient conditions.^[10] The devices prepared with spiro-OMeTAD presented a significant jump in both short circuit densities (J_{sc}) and open circuit voltage (V_{oc}) cementing the transition to fully solid-state device architectures. Lee et al. simultaneously developed a novel architecture, opting to replace the n-type TiO_2 with an insulating mp- Al_2O_3 layer as a scaffold. Curiously, the $\text{MAPbI}_{3-x}\text{Cl}_x$ films fabricated on the insulating scaffold Al_2O_3 out-performed that fabricated on TiO_2 yielding champion PCEs of 10.9% and 7.6%, respectively. The surprising result offered insights into both the ability of perovskite to efficiently transport carriers and the significant impact of trap states at the sensitizer/ TiO_2 interface on the carrier densities and subsequent quasi-Fermi level splitting. The Al_2O_3 scaffold based devices consequently exhibited a notable V_{oc} improvement achieving up to 1.13 V ($E_g = 1.55$ eV), hitherto unheard of in PSCs. In light of the absence of an electron extraction layer, the structure was termed a meso-superstructured solar cell (MSSC) (Figure 1c).^[5]

Shortly after the identification of mp- TiO_2 surface trap states as a key performance loss mechanism, Ball et al. demonstrated integration of the perovskite layer into a planar heterojunction thin film stack architecture, widely used in existing PV technologies such as OPV, GaAs, CIGs, and CZTSe. To produce the thin film architectures, mp- TiO_2 was omitted in favor of a compact n-type TiO_2 layer, while a thin layer of p-type spiro-OMeTAD sandwiched the intrinsic perovskite layer, acting as a hole conductor (Figure 1d). The shift to a planar n-i-p architecture also enabled the production of PSCs at significantly reduced temperatures, both reducing the fabrication cost while also opening-up opportunities to high throughput printed electronics on flexible substrates.^[11] In a key finding, the planar heterojunction exhibited high internal quantum efficiencies (IQE) confirming the ability of perovskite thin films to behave as intrinsic layers with long lifetimes and diffusion lengths for both electrons and holes. Replacing spin coating perovskite with dual-source vapour deposition onto a compact TiO_2 ETL, Liu et al. further advanced the PSC efficiency to a record 15.4%, narrowly surpassing the previous record of 15.0% achieved from a two-step sequential deposition method.^[12,13]

Around the same time, Jeng et al. revealed the ability of the perovskite to transfer electrons into [6,6]-Phenyl-C₆₁-butyric acid methyl ester (PCBM) in a manner similar to bilayer films used in OPV technologies. Identifying poly(3,4-ethylenedioxythiophene)poly(styrene-sulfonate) (PEDOT:PSS) as an effective hole conductor, Jeng prepared a thin film planar heterojunction architecture in which the motion of the carriers was reversed through the inverting of the p and n type transporting layers. The subsequent p-i-n device produced a PCE of 3.9% (Figure 1e).^[14] Within a year, a wealth of research improved

the PCE of inverted devices to exceed 15% while also identifying the tendency of fullerene based PSCs to exhibit reduced hysteresis.^[15,16]

More recently, optimization of the composition, fabrication and passivation techniques have enabled the PCE of these established architectures to improve significantly with contemporary n-i-p and p-i-n conventional planar heterojunction structures frequently surpassing 20%. In particular, the adoption of new HTLs such as poly(triaryl amine) (PTAA) and poly(4-butyltriphenylamine) (poly-TPD) in addition to careful surface passivation of planar metal oxide ETLs has played a key role in improving p-i-n and n-i-p architectures respectively.^[17–23] Similar gains in the PCEs have also been made using the conducting nano-scaffold-based architecture, through a series of advancements and optimizations. Recent doping of mp-TiO₂ photoanodes using Li salts, has enabled a certified PCE of 24.6%.^[24,25] Devices prepared with no perovskite: perovskite lower dimensional GHJ phase. Additionally, the discovery of new TiO₂ morphologies combined with new scaffold ETLs, such as all carbon materials, has provided space for innovation in conducting mesoscopic cells.^[26–28] Nevertheless, key challenges associated with the perovskite layer, such as light management, stability and efficient carrier extraction remain. These challenges provide scope for further device performance improvement and can be tackled through innovations in the architecture of the interface above the perovskite layer.

This review looks towards possible future architectures of PSCs and addresses the recent resurgence in perovskite architecture engineering. Historically, the integration and adaptation of pre-existing technologies has been influential in enabling the rapid development of PSCs. This trend looks set to continue with increasing reports of perovskite bulk heterojunctions (BHJs) (Figure 1f,g) and graded heterojunctions (GHJs) (Figure 1h,i) previously used in thin film technologies.^[29–31] This review summarizes the recent progress of emerging device architectures, highlighting key advantages relative to conventional architectures while noting key challenges that must be addressed. To assist the integration and optimization of perovskites into these architectures, design criteria are provided and requirements where further study is required are also noted. Finally, an outlook and perspective are offered for the future work of PSC architecture engineering.

2. Perovskite Bulk Heterojunctions

2.1. Nanostructured Perovskite BHJ

The development of perovskite bulk heterojunctions (BHJs) in which a donor-acceptor interface is dispersed within the active region has already revolutionized the field of OPVs. When used in OPV structures, the architecture promotes the separation of tightly bound Frenkel excitons and facilitates transport of free carriers through the bulk and into charge transport layers (CTLs).^[32] Following in the footsteps of OPVs, the BHJ has since been adapted for use in fully inorganic quantum dot (QD) solar cells and more recently into PSCs.^[33–35] This section highlights the development of these novel bulk heterojunctions by considering nano and micro-structuring of the perovskite film as a

method to incorporate a CTL within the bulk active region. While the use of bulk heterojunction structures has historically focused on optimizing the yield of exciton separation, recent innovations in perovskite BHJs looked to address a new set of challenges such as improving light harvesting efficiencies (LHE) and suppressing recombination compared to conventional planar architectures. While the reported naming of such structures as a bulk heterojunction is arguably tenuous due to the large perovskite domain sizes compared to the fine nanometer blend in OPV, a CTL material is still located within the bulk active region and as such the architectures are here referred to as BHJs.

The potential benefits of engineering a perovskite BHJ was first identified by Yang et al. who used the BHJ terminology to describe a structure in which CTL could permeate between the large grains of perovskites. Scanning transmission electron microscopy (STEM) revealed the presence of extended vertical grain boundaries through the bulk within which spiro-OMeTAD can infiltrate. Electron beam induced current (EBIC) measurements of the device cross section reveals that efficient carrier extraction within the bulk occurs predominantly at the grain boundaries between the perovskite and HTL (Figure 2a). The formation of localized electronic fields, which lead to carrier drift, can be observed from the EBIC line profile across perovskite grain boundaries. The improved carrier collection at the interface with spiro-OMeTAD within the bulk highlights the benefits of increasing the interfacial area within the perovskite layer and expanding the region through which carriers can be driven by the electric field the built in potential (Figure 2b).^[36] The combination of large highly crystalline grains combined with more efficient carrier extraction from a diffused heterojunction, enabled PSCs with IQEs approaching 100%, improving upon the n-i-p architecture previously presented by Ball et al.^[11]

While the early predictions made by Ball et al. that planar heterojunction thin films stacks can work effectively in PSCs have since been realized, it is apparent that a carrier separating heterojunction within the bulk can improve the device performance. To date a number of highly efficient PSCs have continued to use a mp-TiO₂ ETL.^[37] While the effect of structuring the perovskite via a scaffold likely plays some role in improving efficiency, we note that PCEs produced with mp-TiO₂ significantly outperform insulating MSSC architectures and highlight the effect of carrier extraction within the bulk is key to performance rather than the effects of scaffolding. It is thus not surprising that following this early work, research has looked to maximise the IQEs through developing a range of novel bulk heterojunction architectures.

From an early stage, perovskite nanowire (NW) films have been identified as a promising approach to create an intimate donor-acceptor heterojunction, due to the simple fabrication, high density of pores and high lateral conductivity.^[38,39] The use of nanowires in a solar cell was first reported by Im et al., whereby the high aspect ratio of the perovskite NW morphology enabled formation of an intimate contact with spiro-OMeTAD subsequently improving carrier extraction at the HTL interface (Figure 2c). Time resolved photoluminescence (TRPL) measurements revealed a faster decay of excited states in the NW BHJ enabling 79% hole extraction over a 700 ps period compared to 68% extraction in a bulk sample over 2.9 ns (Figure 2d,e). Through conducting TRPL measurements

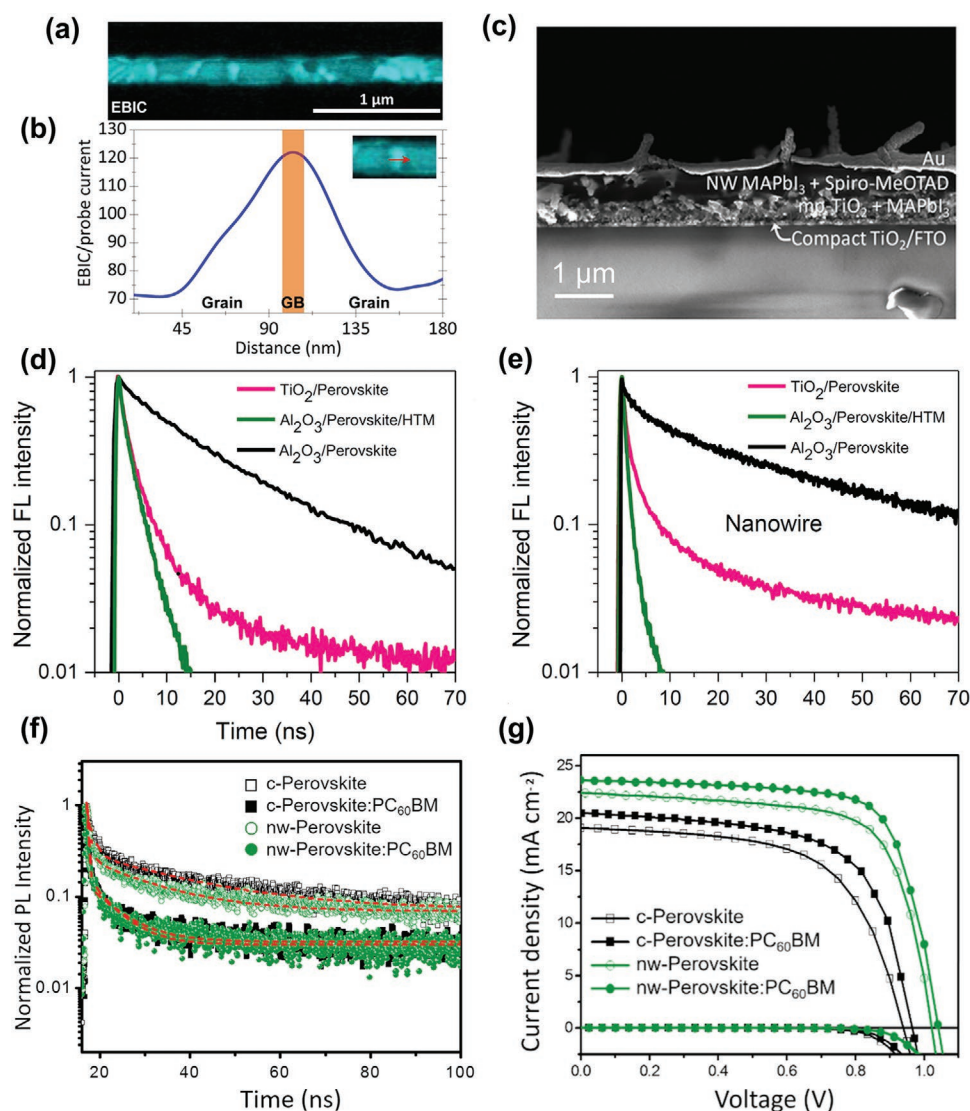


Figure 2. a) EBIC profile across a ITO/TiO₂/MAPbI₃/Spiro-OMeTAD/Ag device cross section. b) EBIC line profile across grain boundary (inset). Reproduced with permission.^[36] Copyright 2015, American Chemical Society c) Cross Section SEM image of NW PSC. d,e) TRPL decays of planar and NW perovskite films excited at 406 nm using a 11 ps pulse⁻¹. Reproduced with permission.^[38] Copyright 2015, American Chemical Society. f) TRPL decays of FTO/TiO₂/perovskite:PCBM and FTO/TiO₂/perovskite. g) *J*-*V* curves of planar and NW structured PSCs with and without PCBM in the light and dark. Reproduced with permission.^[39] Copyright 2018, Elsevier.

on films both with and without external transport layers, the effects of carrier extraction could be decoupled from intrinsic changes in non-radiative recombination, confirming that the change in lifetime could be directly attributed to enhanced carrier extraction rather than dominating effects from an increase in surface recombination. Despite the promising modification to the hole extraction kinetics, the electron extraction efficiency was hindered by the reduced contact between perovskite and mp-TiO₂, decreasing the yield of extracted photogenerated electrons from 65% to 51%. Nevertheless, the early NW PSCs exhibited a promising early PCE reaching 14.7%.^[38]

The challenge of facilitating electron injection between the NWs and TiO₂ was recently reinvestigated by Singh et al. who added PCBM directly to the perovskite precursor solution. The NW:PCBM blended films exhibited shorter TRPL lifetimes on a

TiO₂ substrate from 0.31 to 0.28 ns, highlighting the ability of the blended structures to promote carrier extraction (Figure 2f). Consequently, the PCE of NW devices increased up to 18.7%, higher than both the reported planar control and pure NW devices, yielding PCEs of 12.3% and 16.8%, respectively (Figure 2g).^[39] In an alternative approach, NW based inverted p-i-n architectures have been shown to promote fast carrier extraction at both contacts adjacent to the perovskite layer. However, the poor surface coverage of PCBM in such architecture presents a challenge in finding suitable ETLs. In a recent work, Chang et al. demonstrated a doped non-fullerene acceptor enabling a champion PCE of 18.8% in a small area devices (0.12 cm²) and impressive PCE of 15.2% in a large area devices (5.05 cm²).^[40]

More recently, strategies to produce a heterojunction within the bulk have focused on locally structuring the morphology

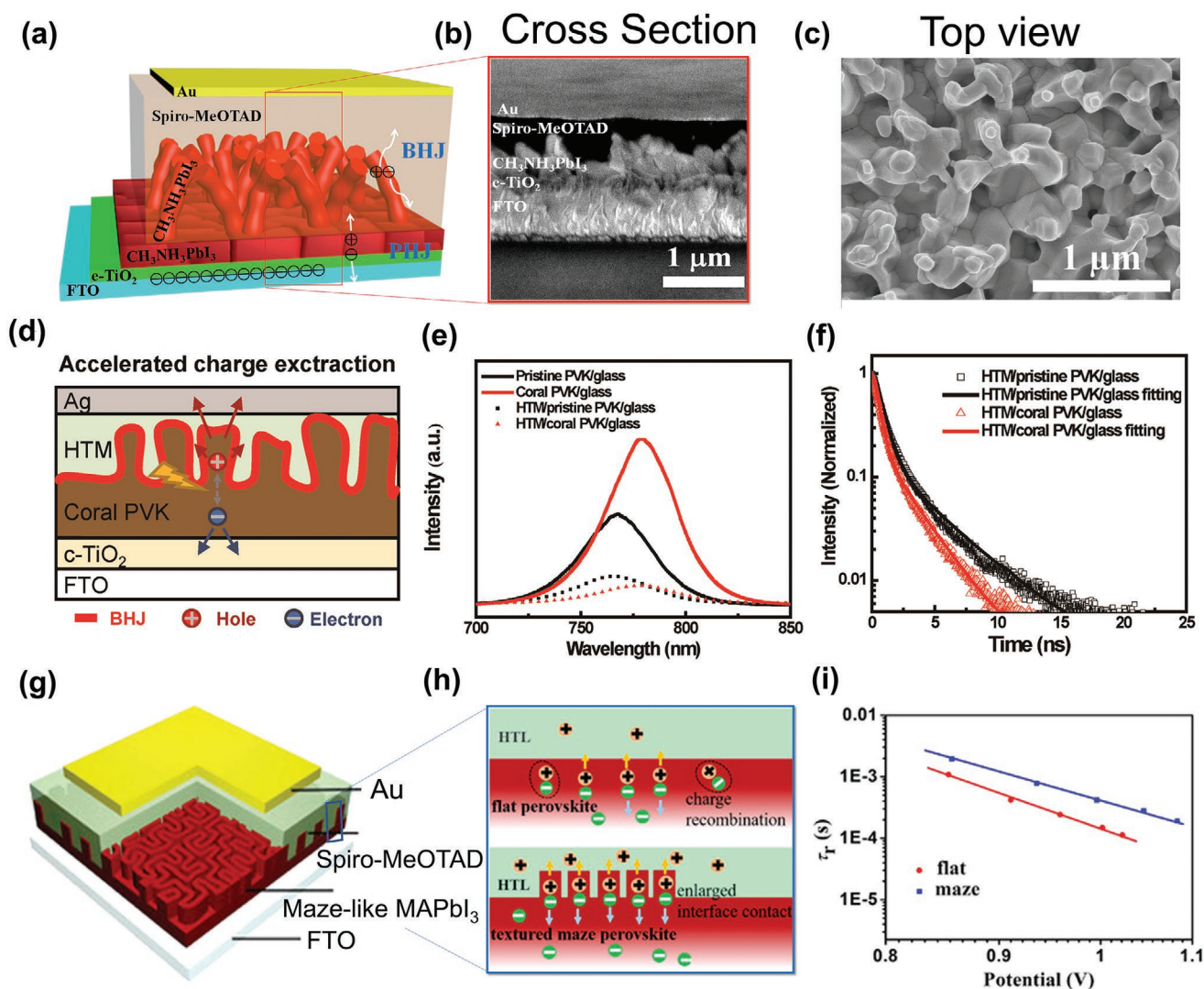


Figure 3. a) Schematic diagram of perovskite nanocoral BHJ architecture produced with a compact bottom film, carrier separation occurs at the coral/Spiro-OMeTAD interface, b) SEM images of the BHJ device cross section and surface morphology of the nanocorals, arrows point to dense underlayer. a,b) Reproduced with permission.^[46] Copyright 2017, Elsevier. c) SEM image of perovskite coral structure. Reproduced with permission.^[42] Copyright 2017, American Chemical Society. d) Schematic of carrier extraction in perovskite coral architecture. e) Steady-state PL of perovskite films with and without HTL. f) Normalized TRPL of the decays of the BHJ and PHJ. d–f) Adapted with permission.^[45] Copyright 2019, Elsevier. g) Schematic of ETL free maze perovskite BHJ architecture. h) Schematic of improved carrier separation in the BHJ compared to PHJ. i) Charge carrier lifetime as a function of voltage for PHJ and BHJs. Reproduced with permission.^[46] Copyright 2019, Copyright 2017, Elsevier.

at the perovskite top interface leaving a dense bottom layer to form a compact interface with the ETL (Figure 3a,b). The compact perovskite bottom layer also plays an essential role in preventing shunting of the device. In an early study Pascoe et al. constructed a coral BHJ on a compact perovskite film via a glucose additive method.^[41] The BHJ structure outperformed the PHJ exhibiting increased quenching and lowered series resistance from 2.79 to 1.48 Ω, due to more efficient charge extraction between the perovskite corals and a compact spiro-OMeTAD film. Within a year, a similar antenna based architecture was reported via solvent post treatment of a perovskite film (Figure 3c).^[42,43] The reported BHJ architectures exhibited improved PCEs compared to the PHJ counterparts reaching up to 17.7% in the glucose additive method, how-

ever the stability compared to the planar films was notably compromised.^[41]

More recently, Lu et al. improved both the efficiency and stability of coral structured BHJs through using a secondary cation spin coating step depositing a solution of FAI and DMF in IPA solution onto an annealed MAPbI₃ (Figure 3d). Post treatment of the films with a secondary cation solution has been shown to both reduce defects through a change in termination while improving the crystallinity as discussed in later sections. Consequently, the FAI treated devices exhibited improved stability compared to the planar control perovskite film. The result is also in good agreement with the reported absence of increased non-radiative recombination in the NW structure produced by Im et al. who also promoted anisotropic growth via combining

DMF with an organic cation.^[38,44] Accordingly, the authors report higher PL intensity in coral structured FA_{1-x}MA_xPbI₃ films on glass compared to the planar control suggesting suppressed non-radiative recombination thereby addressing the speculation of increased trapping across an enlarged interfacial area. (Figure 3e). In addition to the increased carrier density, the coral structures also exhibit a higher magnitude of PL quenching following formation of a compact spiro-OMeTAD HTL layer. The increased quenching is in good agreement with TRPL decay revealing shorter carrier lifetimes across the BHJ interface and thus faster more efficient carrier separation (Figure 3f). Consequently, the secondary growth surface coral films showcased PCEs of 19.5% improving beyond 17.2% reported for the PHJ control.^[45]

Similar reductions in non-radiative recombination and faster extraction were recently reported in MAPbI₃ films prepared with a maze-like surface morphology (Figure 3g). Concurrent with the previously discussed works, the maze morphology exhibited faster carrier extraction between perovskite and interdigitated spiro-OMeTAD exhibiting a shortening of TRPL lifetimes at the interface from 12.8 to 5.6 ns. Recombination of the carriers was investigated using intensity-modulation photovoltage spectroscopy (IMVS).^[47] Recording the carrier lifetime at varying illumination intensities revealed significantly longer lifetimes in the BHJs, owing to rapid extraction of holes across the blended perovskite/HTL interface (Figure 3h). The MAPbI₃ based ETL-free PSCs yielded an encouraging PCE of 18.5% and remarkable V_{oc} (1.08 V) and FF (77%) demonstrating the ability of the single bulk heterojunction to effectively separate carriers within the active region.^[48]

While self-assembly methods such as those discussed, have historically played a key role in forming nanostructured perovskite architectures, control of the morphology is often poor and may prove to be difficult for large area fabrication such as roll to roll printing. More recently, nano-imprinting and templating techniques have presented an alternate approach offering high levels of control over the morphology geometry, enabling optimization of key parameters such as the dimensions of perovskite structures within the film. Unlike self-assembly methods, the use of nano-imprinting is a suitable choice for large-area device fabrication and opens the door to a range of new photonic structures. Using this approach Wang et al. prepared perovskite films with a diffraction grating morphology via CD and DVD based polydimethylsiloxane (PDMS) soft stamps. Interestingly the authors found that finer spacing between troughs in the DVD compared to the CD stamp results in shortened PL lifetimes from 18.93 to 15.49 ns, both shorter than the PHJ (36.72 ns). An identical trend was also reported between grating density and recombination resistance with the finer DVD grating exhibiting less trap-based recombination owing to more efficient separation of carriers across the heterojunction (Figure 3h). Consequently, PSCs prepared using a MAPbI₃ DVD diffraction grating showed a PCE of 19.7%, V_{oc} (1.11 V), and FF (76.75%) compared to the control device with PCE 16.7%, V_{oc} (1.078 V), and FF (71.52%). The increase in FF and V_{oc} can be attributed to a combination of more crystalline grains from templated growth and improved carrier extraction dynamics in the PSC. A similar trend between an enlarged interfacial area and PSC performance has also been reported

in films patterned with cylindrical stamps. While the improved collection efficiency from the increased interface is no doubt important to improving the V_{oc}, the effect of LHE on J_{sc} also contributes to the PCE improvement and is discussed in the next section.

As discussed, the formation of a heterojunction within the bulk perovskite enables improved carrier extraction with films exhibiting increased PL quenching, reduced non-radiative recombination and reduced series resistance. Similar to the highly effective mp-TiO₂ interface, a distribution of an acceptor material within the bulk perovskite, has enabled increased PCEs benefitting from high FF and V_{oc} across a range of proof-of-concept architectures. Furthermore, the use of nanostructured interface architecture has already undergone an evolution from PCEs of 14.7% to 19.5%, through the reduction of shunts, reduction of defects at the interface and formation of a compact bottom layer with a CTL substrate. In addition to controlling the carrier extraction dynamics, the nanostructured perovskite architecture also offers new benefits in LHE.

Engineering the photonic properties of PSCs is a promising method for increasing photocurrents closer to the theoretical limit up to 26.9 mA cm⁻² in MAPbI₃.^[49] While a fraction of these losses are largely unavoidable through reflection of light at interfaces prior to reaching the perovskite layer or parasitic absorption from a CTL, there is a scope for reducing avoidable losses within the stack. In particular, this can be achieved by improving the absorbance of low energy photons. The potential of light management was recently demonstrated by Kim et al. who used a PDMS inverse opal (IO) film to modify the optical properties of a double cation PSC, which exhibited impressive photocurrents of up to 25.11 mA cm⁻². The use of a IO textured perovskite also has interesting applications in producing coloured perovskite films, useful for commercial applications such as building-integrated photovoltaics (BIPV) (Figure 4a).^[50,51] More significantly for photovoltaic performance, studies using 3D finite-difference time domain (FDTD) simulations on the IO structure has identified profound changes in the absorption profile. This is particularly evident at low photon energies where the absorbance of long wavelength photons is improved, highlighting opportunities for nanostructured perovskites to improve LHE perovskite to improve LHE, as discussed in more detail later (Figure 4b,c).^[52]

Zhou et al. investigated the use of perovskite photonic IO structures to overcome some of the key challenges of wide band gap, fully inorganic CsPbBr₃ PSCs. Films prepared using CsPbBr₃ perovskite exhibit increased exciton binding energy compared to the organic-inorganic hybrids which has been reported as high as 350 meV.^[54] Additionally, poor overlap with the solar spectrum frequently limit the J_{sc}, to below 10 mA cm⁻².^[54-56] The IO films improved the EQE through slowing incident photons (slow-photon-effect), a promising approach to improve photon absorbance around a photonic band gap (PBG) originating from the periodically changing dielectric constant of IO films.^[57] To synergistically promote the separation of excitons, the voids in the structure were further filled with CQDs. Modification from the planar heterojunction enabled photocurrents reaching 11.34 mA cm⁻² and PCEs of up to 8.2% (PHJ: 3.5%).^[58] In a follow up work, Zhou et al. replaced the CQDs with silicon quantum dots enabling

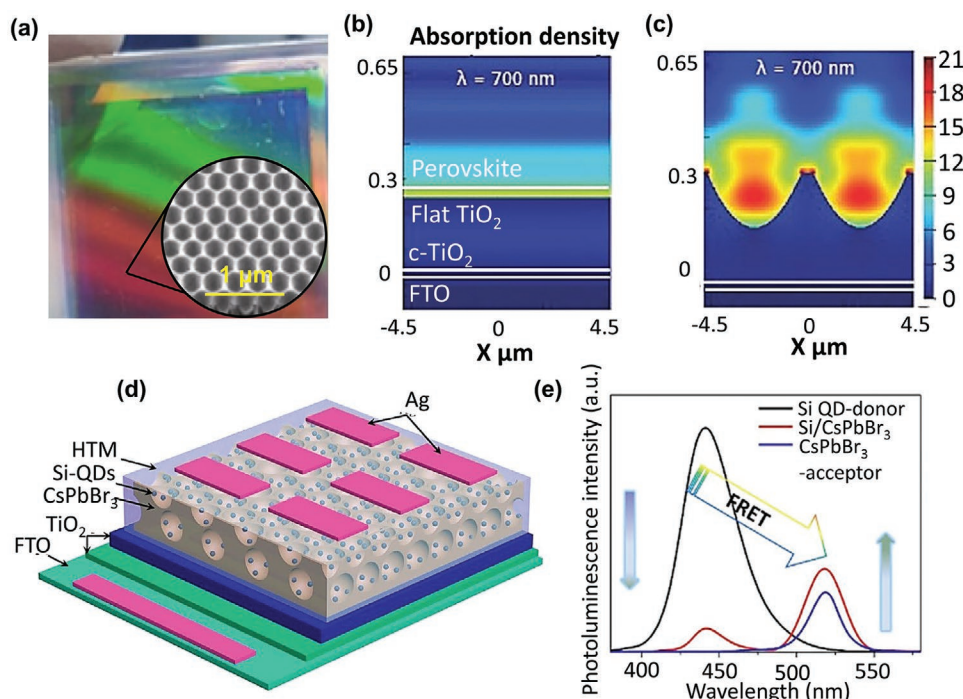


Figure 4. a) Multicoloured perovskite film fabricated using a PDMS IO film (inset). Adapted with permission.^[50] Copyright 2019, Springer Nature. b,c) Spatial profile of optical absorption at 700 nm incident light for flat and IO structures respectively. Adapted with permission.^[52] Copyright 2016, Wiley-VCH. d) Device architecture of SiQD enhanced CsPbBr₃ IO film. e) PL spectroscopy of Perovskite:Si-QD film showing FRET enhanced emission. d,e) Adapted with permission.^[53] Copyright 2019, Elsevier.

Förster resonance energy transfer (FRET) between the spectral overlaps of the semiconductors (Figure 4d–e). Consequently the improved light capture further improved the device PCE to 8.3% compared to the 3.0% control device.^[53]

Recently, intriguing whispering gallery mode (WGM) enhanced absorption has been reported by Wang et al.^[59] To create resonator cavities, the authors stamped MAPbI₃ films with a micropillar structured PDMS stamp (Figure 5a). It is pertinent to note that the use of whispering gallery photonic modes has successfully been integrated into sensitizer based photovoltaic architectures. In the established whispering gallery solar cells, photonic resonances around smooth TiO₂ microspheres can couple to the sensitizer improving the light harvesting of the solar cell at wavelengths at which resonances occur.^[60] Interestingly, the PL of the stamped MAPbI₃ WG structure did not exhibit the regularly spaced sharp characteristic modal peaks typically observed in WG structures occurring from coupling between the emitted light and resonant cavity WG modes (Figure 5b).^[60,61] While the reported WG modes are possible, the absence of resonances in optical spectroscopy make such claims difficult to validate and the impact of the approach unclear. Regardless, the cylindrical stamped PSCs exhibit a clear increase in both LHE and consequently J_{sc} upon the patterning of the perovskite film (Figure 5c).^[59]

In contrast to the WGM structures, the photonic properties of perovskite diffraction gratings are less ambiguous and can be visually confirmed through the formation of diffraction patterns upon illumination with a laser source (Figure 5d,e).^[63] The improved light scattering ability in the rear grated MAPbI₃ structure increased the J_{sc} from 21.67 to 23.11 mA cm⁻², yielding a

similar improvement in current density to the MAPbI₃ solar cells prepared with WGM structures (20.90–23.62 mA cm⁻²). EQE plots reveal a clear increase in the conversion of incident photons around the band gap while a small uniform increase is observed at wavelengths in the green region of the spectrum (550 nm), the latter of which is likely a consequence of enhanced internal quantum efficiency (IQE) previously discussed (Figure 5f). The perovskite diffraction grating was more recently investigated by Zhang et al. who modeled the cross-sectional distribution of the electric field to further understand the absorbance within the light harvesting layer. Modeling the cross-sectional electric field distribution of the planar and grated architectures revealed the breaking of planar uniform electric fields when using a textured perovskite surface, resulting in hot-spots of strengthened electronic field improving the interaction of the active layer with light via scattering. These enhancing effects are particularly pronounced at longer wavelengths close to the band gap and where light is less strongly absorbed (Figure 5g). The modeling is thus in good agreement with the experimentally observed EQE enhancements in the red region of the spectrum (Figure 5f).^[64] Similar breaking of flat absorption modes and improved absorbance has also been observed through modeling the electric fields in cylindrical stamped and IO systems (Figure 4b,c).^[52,65]

Enhancement of photon collection around the band gap is frequently reported in textured perovskite films and addresses a key challenge of photovoltaic technologies, the absorption of photons near the band edge.^[66] Marinove et al. experimentally observed that PSCs containing a smooth metal contact capable of reflecting weakly absorbed photons back within the film exhibited improved EQE at longer wavelengths ($\lambda > 600$ nm).^[67]

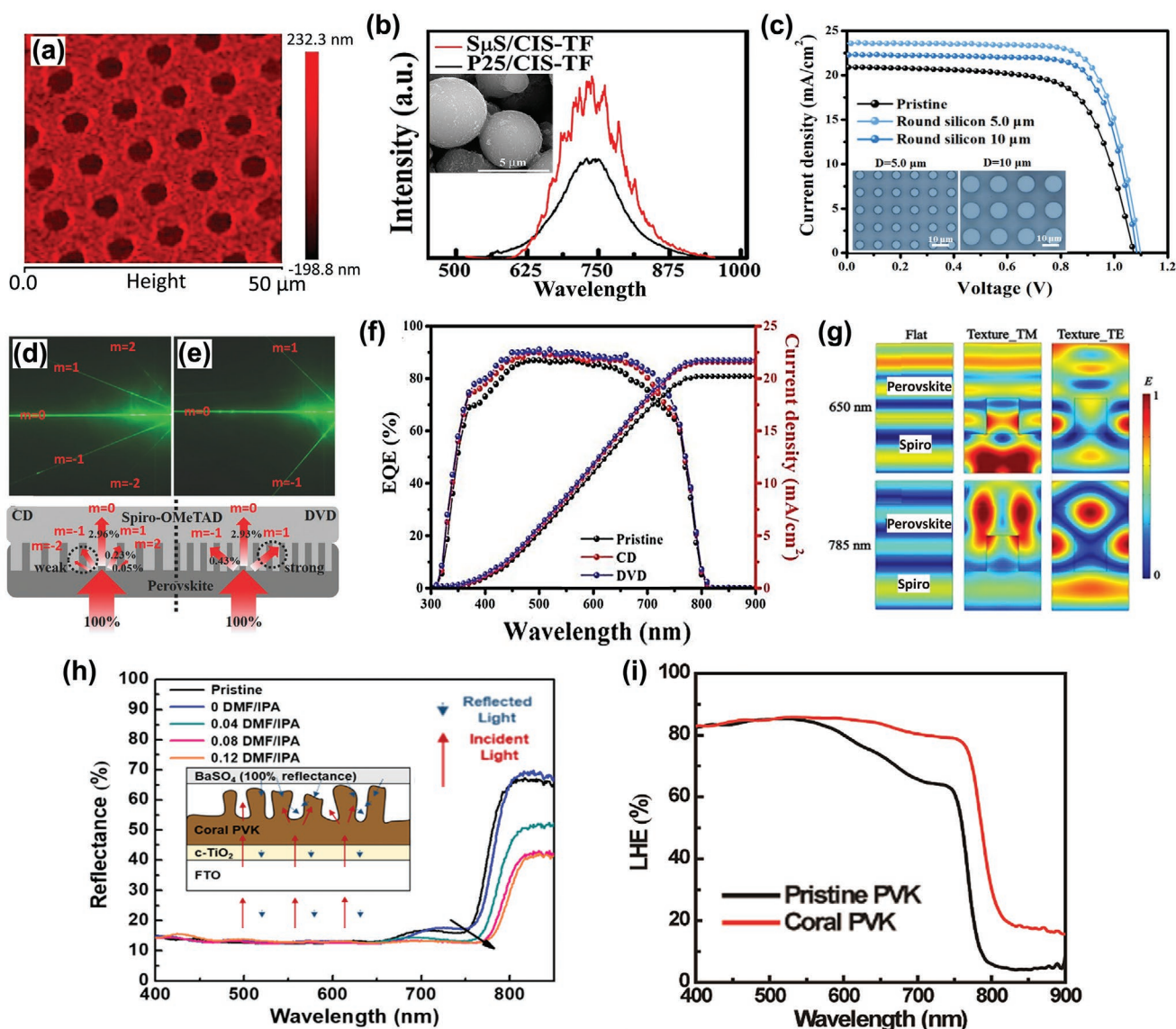


Figure 5. a) AFM image of perovskite film with micropillar imprint. b) PL of CuInS_2 sensitized $\text{S}\mu\text{S-TiO}_2$ (red) and P25-TiO_2 (black). Adapted with permission.^[61] Copyright 2019, American Chemical Society. c) J - V curves of PSC with a planar, 5 and 10 μm diameter stamped film. a, c) Reproduced with permission.^[62] Copyright 2018, Elsevier. d, e) Interaction of perovskite diffraction grating with a 532 nm laser (above) and intensities of modes (below) producing using a CD and DVD respectively. f) EQE and integrated J_{sc} of PSCs prepared with and without stamping. d-f) Reproduced with permission.^[63] Copyright 2018, Wiley-VCH. g) Normalized electric field distribution of PSCs at 650 and 785 nm for flat and diffraction grating films with TE and TM polarization. Reproduced with permission.^[64] Copyright 2020, Springer Nature. h) Reflectance spectra of coral and planar perovskite films. i) LHE spectra of coral and planar perovskite films. h, i) Adapted with permission.^[45] Copyright 2019, Elsevier.

This was found to result from additional absorbance occurring upon a second pass through the film. Upon addition of the smooth metal, incident photons which are not fully absorbed on the first pass may be absorbed following a reflection. While the reflection of photons back into the film from a reflective metal electrode is sufficient to improve the collection of low energy photons to some extent, previous works showing an increase in the perovskite reflection spectrum at long wavelengths ($\lambda > 600$ nm) suggests that such losses continue to occur.^[45,49] Early work to model the optical losses around the near infrared region have suggested a loss in J_{sc} of around 1.36 mA cm^{-2} in MAPbI_3 .^[49] However, the loss in photocurrent from non-absorbed light will vary with both perovskite compo-

sition and the perovskite thickness, with thicker films having longer optical path lengths. It is thus unsurprising that the importance of reducing optical losses around the band gap by optimizing the light in-coupling has subsequently been discussed in a number of studies.^[45,66,68,69]

While it is clear that templated and nano-imprinted nanostructures can effectively improve the collection of long wavelength photons (Figures 4b,c and 5g), similar improvements in LHE have been afforded using solution processing, such as the previously discussed coral structures. Lu et al. investigated the back reflectance of the nanostructured PSC using a highly reflective BaSO_4 layer to simulate the high reflectivity of a metal contact. The study finds that coral films exhibit a

lower fraction of reflected light which can escape the device owing to improved scattering of photons within the film. Consequently, estimates of the LHE considering both the absorbance of the films and change in reflection revealed a significant increase around the band gap (Figure 5i,j). The importance of optimizing the film to increase the yield of low energy photon collection is best demonstrated when considering the profile of the AM1.5G solar spectrum. The region of 600–800 nm, in which light is typically poorly absorbed upon a single pass of the active layer, accounts for around 33.3% of the spectral distribution in an ideal solar simulator.^[70] Effectively capturing these wavelengths is crucial for reducing J_{sc} losses. Furthermore, while a fraction of incident solar radiation incident on the earth is scattered by small molecules in the atmosphere, the actual fraction of non-coherent light is the subject of many studies and figures vary with approximations chosen. However, the total fraction of non-coherent light is considered small. Consequently, several studies have highlighted the implications of largely coherent solar radiation on photovoltaic performance highlighting a strong link between degree of texturing and photocurrent.^[71–73] Such considerations of coherence are often neglected, particularly in the design of solar simulators and published photovoltaic metrics. Nevertheless, such considerations have a fundamental impact in the real-world performance of photovoltaic technologies.

Nanostructured perovskite BHJs with rear-textured light harvesting layers have rapidly progressed in recent years, taking promising steps towards reduced photocurrent losses and light capture of weakly absorbed low energy photons. Furthermore, such strategies may be key in optimizing the real-world performance of photovoltaic devices, in particular considering the implications of coherence and angular dependence on daily averaged perovskite photovoltaic device performance. However, further effort must be devoted to understand the carrier extraction kinetics using alternative methods to PL lifetimes which are highly dependent on factors such as defect density and pump fluence. Instead, techniques such as EBIC should be considered essential in understanding the changes in carrier extraction efficiency. In addition, the use of transient absorption spectroscopy (TAS) is encouraged to probe the timescales and magnitudes of carrier separation across the interface allowing for a more detailed discussion on carrier extraction, as well as trap filling in PHJ and BHJ systems. The ability to improve LHE over a key region of the solar spectrum combined with opportunities to influence carrier transfer kinetics make nanostructured BHJs a promising frontier in PSC development and warrants further exploration and optimization witnessed in other architectures.

2.2. Blended Perovskite Bulk Heterojunctions

Blended BHJs offer a simple alternative strategy to fabricating a heterojunction within the perovskite film bulk. Through the direct addition of a CTL within the perovskite precursor prior to spin coating, a perovskite: CTL blend can be produced. As per the OPV structures, the addition of the secondary n or p-type phase allows for the decoupling of carrier transport within the bulk, while also having potentially significant effects on stability. Recently, a plethora of new BHJ blend architectures have

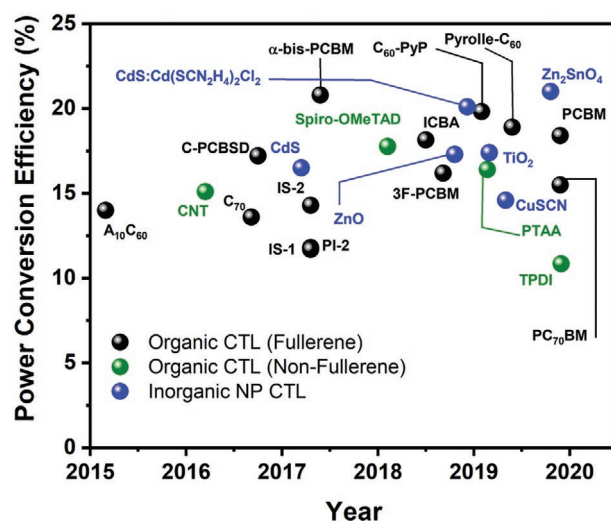


Figure 6. Upward trajectory of blended perovskite:CTL bulk heterojunctions. Highest performing device architecture using various fullerene based CTLs (black), organic non-fullerene CTLs (green), inorganic nanoparticles (NP) CTLs (blue).

emerged optimizing the carrier transport behavior, grain size and stability (Figure 6). In this section the development of such architectures is discussed.

Wang et al. first investigated the blended BHJ through addition of $A_{10}C_{60}$ ($A = CO_2COOH$), an electron accepting fullerene, into the perovskite precursor solution. The authors aimed to create a hybrid perovskite film with improved carrier separation and transport properties utilizing C_{60} as an efficient and low-loss ETL.^[74,75] X-ray diffraction (XRD) patterns of the hybrid films confirm the incorporation of $A_{10}C_{60}$ within the films (Figure 7a). PL spectra of $MAPbI_3$, $MAPbI_3:A_{10}C_{60}$, $MAPbI_3:A_{10}C_{60}/PCBM$ and $MAPbI_3/PC_{61}BM$ films revealed increased quenching in the blended films prepared with additional $A_{10}C_{60}$, owing to energetically favorable electron transfer into $A_{10}C_{60}$ within the bulk. Impedance spectroscopy techniques further substantiated the claim of efficient electron extraction, reporting a drop in charge-transfer resistance (R_{CT}) from 0.85 to 0.66 k Ω as a consequence of larger interface across which carriers can transfer. Accordingly, the series resistance was also reduced from 0.92 to 0.75 k Ω cm⁻². Ultimately, early inverted BHJ PSCs demonstrated an improvement in photovoltaic performance with an increased average PCE of 13.9% compared to an average of 11.4% in the planar control. Benefitting from improved light harvesting due to the photoactive $A_{10}C_{60}$ within the film, the BHJ device also showcased improved J_{sc} from 17.31 to 19.41 mA cm⁻² and consistently high FFs reaching up to 86.7%, sparking interest from the community.^[75]

Subsequent work has since integrated a range of electron and hole acceptors within the bulk perovskite, however the effects of the additional n- or p-type material within the film on the extraction of the carriers remains contested with multiple pathways suggested.^[76,77] The most frequently suggested mechanism of carrier extraction in the BHJ architecture is that photogenerated carriers are rapidly extracted from the perovskite grain boundaries within the bulk via an intergrain CTL network. The formation of such network has previously been suggested using high-angle annular dark-field scanning transmission electron microscopy (HAADF-STEM).^[78] Following

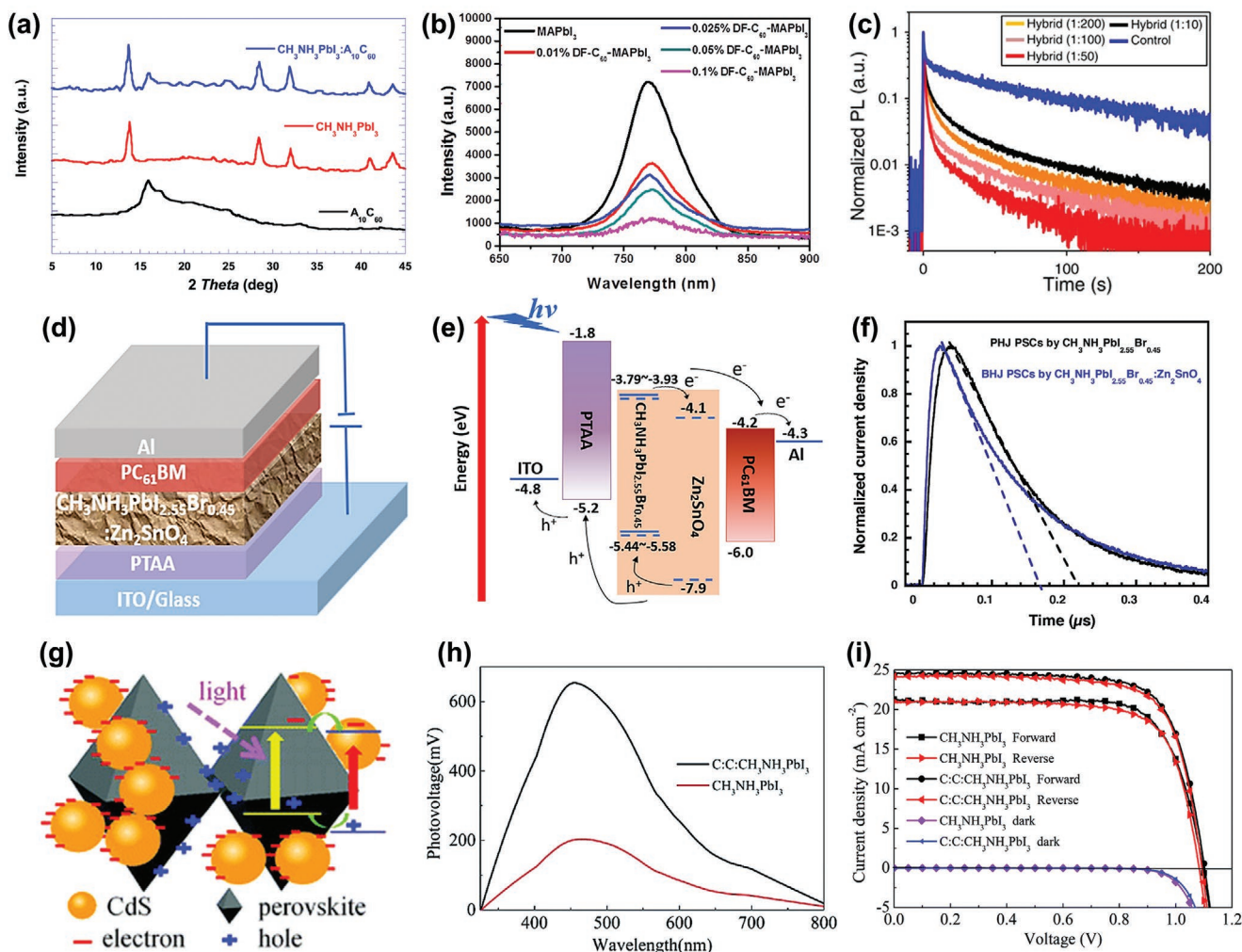


Figure 7. a) XRD of MAPbI₃:A₁₀C₆₀ blend, MAPbI₃ and A₁₀C₆₀. Reproduced with permission.^[75] Copyright 2015, Royal Society of Chemistry. b) Steady state PL of MAPbI₃ with increasing DF-C₆₀ from 0–0.1 wt %. Reproduced with permission.^[79] Copyright 2016, Elsevier. c) TRPL decay of MAPbI₃:PCBM blends with varying PCBM concentration.^[82] d) Device architecture of p-i-n MAPbI_{2.55}Br_{0.45}:Zn₂SnO₄ blended BHJ. e) Schematic of band alignments in the Zn₂SnO₄ BHJ architecture. f) Normalized photocurrent decay of MAPbI_{2.55}Br_{0.45} and MAPbI_{2.55}Br_{0.45}:Zn₂SnO₄ based PSCs. Reproduced with permission.^[90] Copyright 2019, American Chemical Society. g) Schematic of carrier separation between perovskite and CdS QDs. h) Surface photovoltage spectrum of FTO/c-TiO₂/mp-TiO₂/MAPbI₃ and FTO/c-TiO₂/mp-TiO₂/MAPbI₃:CdS: Cd(SCN₂H₄)₂Cl₂ half cells. i) J–V curves of MAPbI₃ and MAPbI₃:CdS: Cd(SCN₂H₄)₂Cl₂ based inverted PSCs. Reproduced with permission.^[91] Copyright 2018, Royal Society of Chemistry.

carrier separation at the perovskite grain boundaries, the CTL transports the carriers to a sandwiching planar CTL (Figure 1g) which in turn facilitates carrier transport to a metal electrode and out the device. This pathway for photogenerated carriers is supported by numerous accounts of steady state PL perovskite quenching in perovskite: CTL films on a glass substrate proportional to the concentration of a CTL precursor additive (Figure 7b). However, such results are not by themselves conclusive.^[75,78–81]

The steady-state PL is further supported by TRPL studies which reveal a similar trend between increasing CTL concentration and shorter lifetimes as a more extended CTL network is formed in perovskite: CTL films.^[79,81–83] However, findings by Xu et al. suggest that at high concentrations of PCBM, carrier extraction is reduced (Figure 7c). Assuming that carriers are indeed extracted through an interconnected CTL network,

such observations may be explained through the tendency of PCBM to aggregate at high concentrations, particularly in polar solvents, and therefore reduce the distribution of the required inter-grain extraction network as previously reported in OPV.^[84] It is therefore important that the concentration of a CTL is well optimized for good distribution within the perovskite layer. Additionally, fullerene CTLs have been demonstrated to intrinsically permeate between perovskite grains, beneficial for establishing the hypothesized percolated ETL network.^[15,85]

It is noteworthy when considering such a mechanism that while the hopping and polaron limited mobility of organic ETLs is orders of magnitude of lower than the crystalline perovskite films, the kinetics of electron transfer to the CTL occur on a faster timescale (<10 ps) compared to diffusion through the film (>200 ps).^[86] It is therefore likely the carriers within the BHJ films which are separated into an organic CTL may

experience reduced mobility. However, the use of planar CTL sandwich layers adjacent to the perovskite will already place limitations on the overall flow of carriers through the PSC, via limiting the mobility and thus reducing any bottlenecks which may arise within the film.^[74] Furthermore, recent work by Jiménez-López et al. suggests that the formation of a C₆₀ layer can improve the slow electron transfer into TiO₂, preventing charge accumulation at the interface and reducing hysteresis.^[87] Additionally, probing TRPL lifetimes of a TiO₂/perovskite:fullerene interface has revealed similar fast carrier extraction kinetics, further suggesting mobility of electrons through the blended CTL is not detrimental to performance.^[83]

It has also been suggested that the dispersion of an inter-grain CTL can act to trap carriers, particularly in the case where a connected inter-grain network isn't be formed.^[76] Unfortunately, frequently used methods to characterize the composition such as XRD and ToF-SIMS offer little insight into the extent of CTLs to aggregate and permeate between grains. However, this challenge may again present opportunities for EBIC and high resolution TEM to image the formation of CTL channels and probe the carrier extraction efficiency between grains. It is highly likely that such isolated regions of CTL form and to some extent will be largely unavoidable varying from one CTL to another. However, formation of interconnected inter-grain transport networks may be encouraged through good control of the additive concentration as discussed, and tuning of CTL functional groups to form interactions with perovskite grains.^[88] Crucially, direct comparisons between BHJ and PHJ have repeatedly highlighted superior FF, V_{oc} and PCE in the blended structure, suggesting that the contribution of trapping from isolated blended CTL phases, if it occurs, is overall insignificant in well optimized architectures. Contrastingly, it has also been suggested that the presence of CTL states within the perovskite band gap may promote de-trapping of shallow perovskite surface trap states, increasing the carrier mobility of the perovskite phase.^[77,89] Further work is required to elucidate the key mechanisms and produce clearer design criteria.

While unlikely, the formation of carrier extraction bottlenecks from the blended perovskite: CTL hybrids can be addressed through a range of higher mobility inorganic nanoparticle (NP) CTLs such as CuSCN, ZnO, Zn₂SnO₄, and TiO₂. The ability to tune the mobility of either electrons or holes independently opens new doors to engineering balanced carrier extraction.^[92–94] Recently Xu et al. investigated blending high mobility Zn₂SnO₄ nanoparticles (NPs) within the perovskite structure (Figure 7d,e). The films prepared with Zn₂SnO₄ exhibited a fast photocurrent decay decreasing from 205 to 175 ns which highlights significantly faster carrier extraction in the PSC prepared with Zn₂SnO₄ (Figure 7f). The results were further corroborated with short circuit limited current (SCLC) measurements revealing a fourteen-fold increase in electron mobility, significantly larger than the increase in hole mobility which could be attributed to reduced trap density, in agreement with the formation of beneficial n-type channels. The champion MAPbI_{2.55}Br_{0.45}:Zn₂SnO₄ device showcased promising photovoltaic parameters in the inverted architecture reaching a PCE (21.1%), V_{oc} (1.1 V), J_{sc} (23.3 mA cm⁻²), and FF (82%), a clear improvement compared to the champion control device

with PCE (18.74%), V_{oc} (1.06 V), J_{sc} (22.23 mA cm⁻²), and FF (79%).^[90]

Zhu et al. took the method a step further by combining CdS and Cd(SCN₂H₄)₂Cl₂ CTL additives within the MAPbI₃ bulk to facilitate the separation of both electrons and holes, respectively. In a novel synthesis, cadmium chloride hydrate was reacted with thiourea and CdS QDs within the perovskite precursor yielding a MAPbI₃:CdS:Cd(SCN₂H₄)₂Cl₂ film. Surface photovoltage spectroscopy of MAPbI₃ and MAPbI₃:CdS:Cd(SCN₂H₄)₂Cl₂ half cells prepared on FTO/TiO₂ substrates revealed a significantly more positive surface photovoltage in the BHJ film as a result of efficient extraction of electrons through CdS into TiO₂ while holes were retained within the p-type Cd(SCN₂H₄)₂Cl₂ phase within the perovskite surface (Figure 7f). The PCEs of PSCs prepared containing both p-type and n-type CTL phases outperformed the previously reported for MAPbI₃:CdS based devices (PCE = 16.5%), reaching up to 20.1% in a MAPbI₃:CdS:Cd(SCN₂H₄)₂Cl₂ system.^[91,95] Such approaches may offer a new route to more precisely engineer balanced carrier extraction, a requirement of high efficiency PSCs.

In addition to facilitating carrier extraction from the bulk perovskite, the permeation of an additive acceptor material within the bulk perovskite also offers new opportunities to optimize the device performance through intimate passivation of traps within the film. Previously, Shao et al. suggested that PCBM may naturally diffuse to some extent from the interface into the perovskite bulk (Figure 8a–c). However, the depth to which PCBM can intrinsically penetrate into the film remains unclear.^[15] Addition of the CTL directly within the perovskite precursor solution presents opportunities to encourage uniform dispersion between grains within the bulk active region enabling deeper passivating interactions (Figure 8d,e).^[82] In this section, the ability of the blended CTL to reduce the trap density in the films through direct passivating within the bulk is discussed before looking at the effects on highly crystalline grain growth during crystallization, important for reducing point defects and trap states.

It has been frequently reported that in the case of electropositive point defects Lewis base functional groups can passivate through donation of electrons to electron-deficient sites.^[96,97] Likewise negatively charged point defects can be mitigated through the presence of Lewis acid groups such as fullerenes, whereby excess electrons can be withdrawn from the perovskite (Figure 8f).^[98,99] Fabricating zwitterion CTLs containing both Lewis acid/base groups within the perovskite precursor is a promising approach to effectively passivate both positive and negative point defects.^[100] Wu et al. demonstrated this strategy using a donor-acceptor π conjugated molecule [D- π -A] borrowed from organic photovoltaics, resulting in an 80 meV improvement in V_{oc} and an increase in PCE from 18.2% to 20.1%.^[101]

Alternatively, synergistic passivation of both positive and negative point defects can be achieved through the combination of multiple CTLs as demonstrated by Zhang et al. who combined N-(4-bromophenyl)thiourea (BrPh-ThR) within the perovskite precursor solution and bis-PCBM within the anti-solvent treatment to incorporate both functionalities into the perovskite thin films. Through conducting SCLC measurements of the passivated films, the authors reveal that films

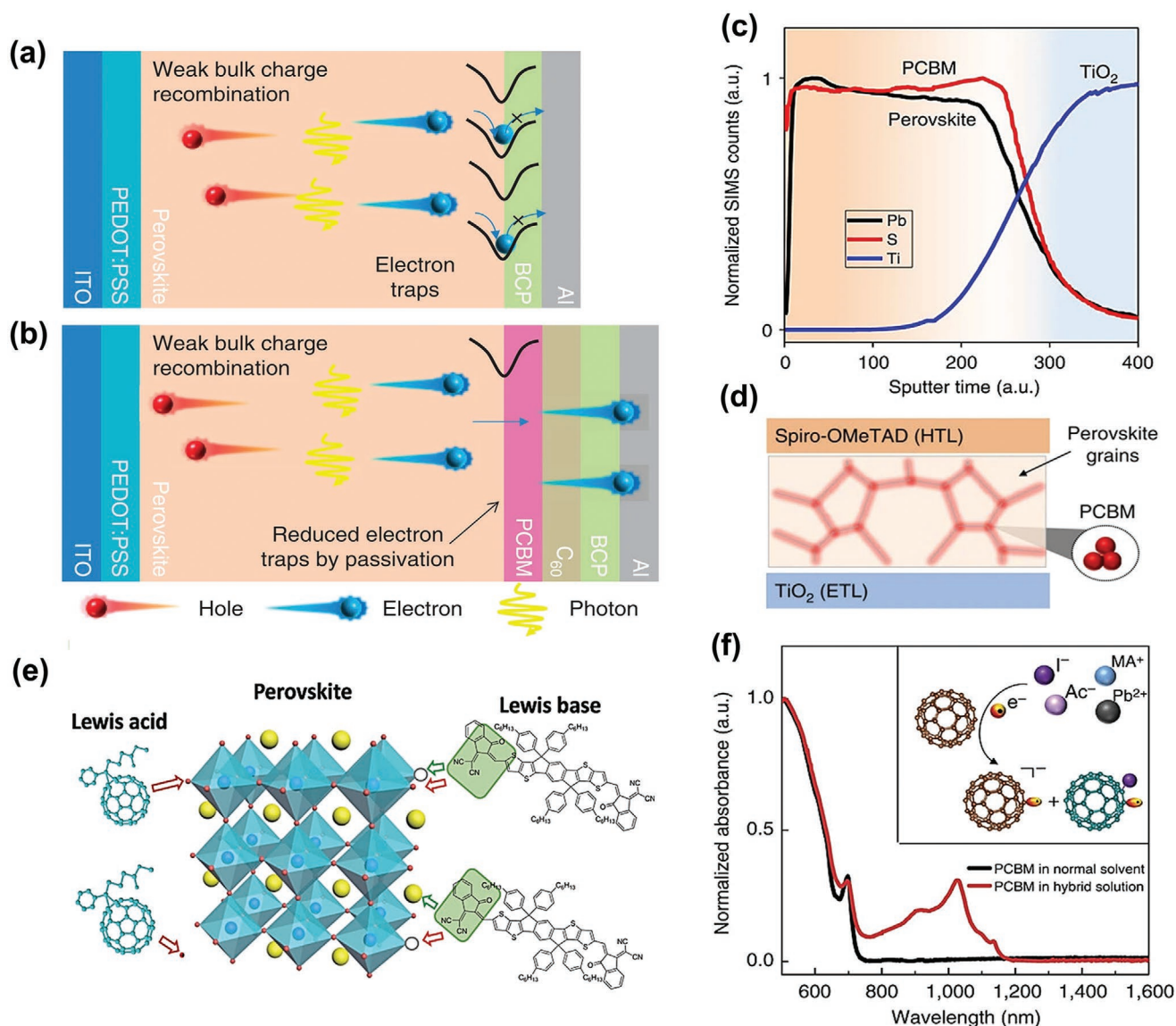


Figure 8. a,b) Schematic of reduced surface trapping in films prepared without and with PCBM respectively. Reproduced with permission.^[15] Copyright 2014, Springer Nature. c) ToF-SIMS data of perovskite:PCBM BHJ film. d) Schematic of PCBM accumulating between grains in a perovskite:PCBM film.^[82] e) Interactions between passivating species and accessible point defects at the perovskite grain boundaries. Adapted with permission.^[77] Copyright 2018, Wiley-VCH. f) UV-Vis data of perovskite:PCBM and PCBM solutions revealing PCBM radical peak around 1 μm , (inset) mechanism of iodide/PCBM interaction.^[82]

prepared using both Lewis acid and base revealed a reduced density of trap states from 17.67×10^{15} to $4.76 \times 10^{15} \text{ cm}^{-3}$ improving hole mobility from 9.26 to $20.91 \text{ cm}^2 \text{ V}^{-1} \text{ s}^{-1}$. The champion devices exhibited a clear improvement in PCE in the synergistically passivated system from 19.3% to 21.7% and negligible hysteresis.^[102] In recent years, fullerenes have become increasingly established as a useful passivating Lewis acid in bulk heterojunction architectures offering key additional benefits such as functional group tunability, suppressing hysteresis and increased electronic stability.^[103] Furthermore, the presence of fullerenes within the perovskite precursor has also been identified to suppress recombination occurring from deep Pb-I anti-sites via interactions between the point defects and PCBM. The additional iodide ion has been shown

to interact strongly with PCBM leading to the formation of a PCBM radical species, identifiable via a characteristic peak in the UV-vis spectrum (Figure 8g).^[82]

In addition to reducing trapping through defect passivation, addition of a CTL within the perovskite precursor has also been demonstrated to promote the formation of larger and more crystalline perovskite grains thus intrinsically reducing the trap density within the films. During the growth of perovskite:CTL films, the addition of the additive introduces additional low energy heterogenous nucleation sites resulting in larger grains with higher crystallinity (Figure 9a–d). To form the optimal grain size the number of nucleation sites must be optimized. Zhu et al. investigated the crystallinity in the blended BHJ architecture using a MAPbI₃:C₆₀-PyP BHJ system. In the study,

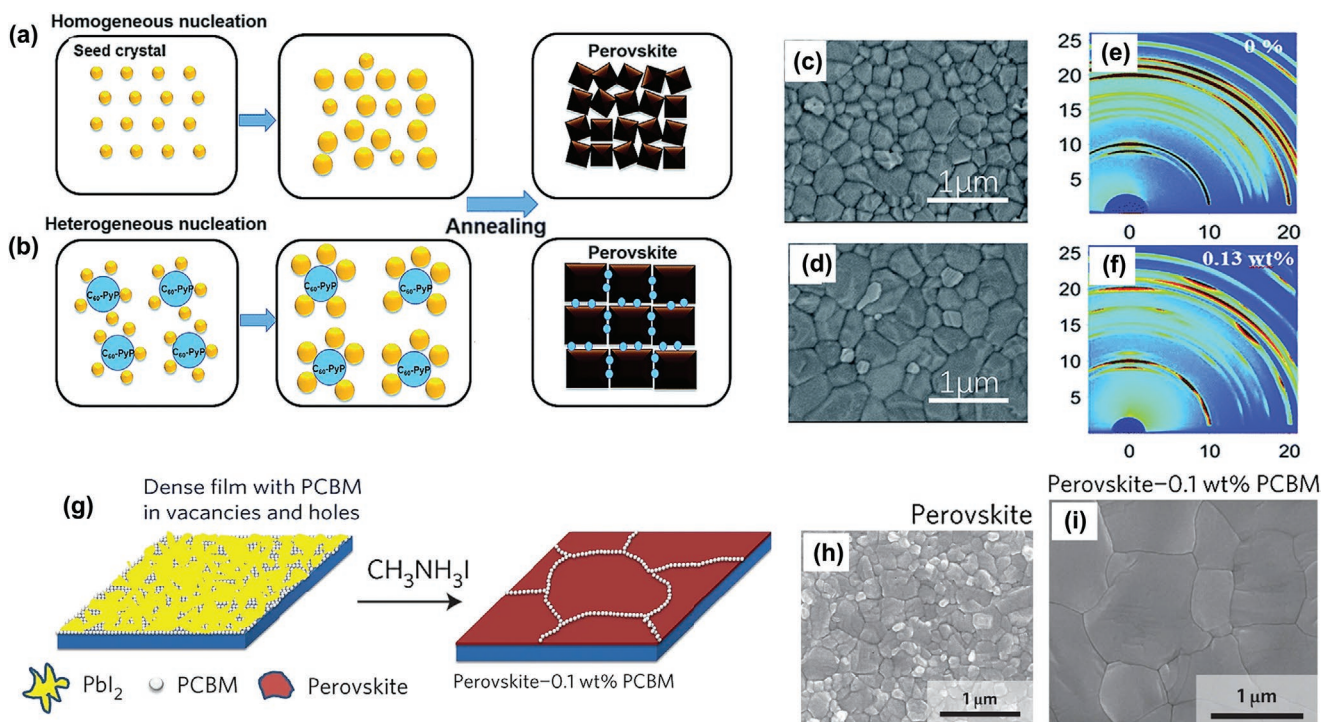


Figure 9. a,b) Schematic of homogenous and heterogenous perovskite nucleation respectively. c,d) SEM images of perovskite grains in a pristine perovskite and perovskite:C₆₀-PyP films, respectively. e,f) 2D GIXRD patterns of pristine perovskite and perovskite:C₆₀-PyP film respectively. Adapted with permission.^[83] Copyright 2019, Royal Society of Chemistry. g) Schematic of two-step BHJ formation via a PbI₂:PCBM films. h,i) SEM images of two-step fabricated using PbI₂ and PbI₂:PCBM films, respectively. Adapted with permission.^[99] Copyright 2016, Springer Nature.

SEM revealed larger grains in the perovskite films prepared using the fullerene additive. Furthermore, a more ordered arrangement of grains was identified through the presence of discrete Bragg spots (110) in 2D-GIXRD scans of MAPbI₃:C₆₀-PyP. The same spots have since been identified in the MAPbI₃:PCBM system, and are beneficial for out-of-plane carrier transport (Figure 9e,f).^[83,104] While less common than the one-step, two-step fabrication of a BHJ has also been reported in which PCBM is introduced to the PbI₂ solution revealing an analogous trend between grain size and concentration of CTL (Figure 9g-i).^[99,105] The increased grain size coupled with improved carrier extraction using a PCBM CTL in the two-step method enabled an increase in PCE from 11.4% in the PHJ to 16.0% in the BHJ.

Finally, we discuss the impact of blending of a CTL acceptor within the bulk perovskite on PSC stability. Perovskite films prepared with a BHJ frequently reported enhanced stability compared to planar heterojunctions.^[79,104,106] One explanation for the enhanced stability is the presence of hydrophobic CTLs between grains plays an important role of preventing the ingress of oxygen and water between grains (Figure 10a).^[79,104] Another explanation detailed by Liu et al. suggests the change in perovskite surface morphology may also play a key role in improving stability with large grains reducing the number of defects and reactive sites on the perovskite lattice.^[104] While the addition of hydrophobic CTLs between grains will suppress moisture ingress to some extent within the perovskite, the distribution of the additives through the film leads to an averaged rather than concentrated fraction of hydrophobic spe-

cies at the interface which prevents the formation of a hydrophobic barrier as later discussed in the graded structures. Comparing the stability of a MAPbI₃:PCBM BHJ under varying degradation conditions it is evident that while the addition of a hydrophobic species between grains reduces the degradation in high humidity conditions (90%). The formation of a perovskite:PCBM blends also affords the structure improved stability under illumination (25 °C; 20% RH) however the origins of such stability has yet to be investigated within the literature (Figure 10b).

To rationalize the improvement in stability under illumination we note a potentially key secondary mechanism yet to be discussed in the literature enabling enhanced tolerance to oxygen via the reduction of superoxide (O₂⁻) yield. Formation of superoxide has been shown to occur from energetically favorable electron transfer between photoexcited perovskite states and the lowest unoccupied molecular orbital (LUMO) of oxygen (-3.75 eV). The destructive O₂⁻ is then able to diffuse between grains and break down the perovskite surface forming PbI₂, I₂ and an organic amine (Figure 10c).^[107] Aristidou et al. demonstrated that when perovskite films were prepared on TiO₂ substrates rather than insulating Al₂O₃, superoxide yield was suppressed (Figure 10d). This was attributed to the introduction of a faster competing pathway to deplete excited states via transfer into the mp-TiO₂ (Figure 10e,f).^[108]

The shortening of perovskite:PCBM PL lifetimes has been discussed previously, in which the carriers are more rapidly extracted from the perovskite film (Figure 7b,c). This observation

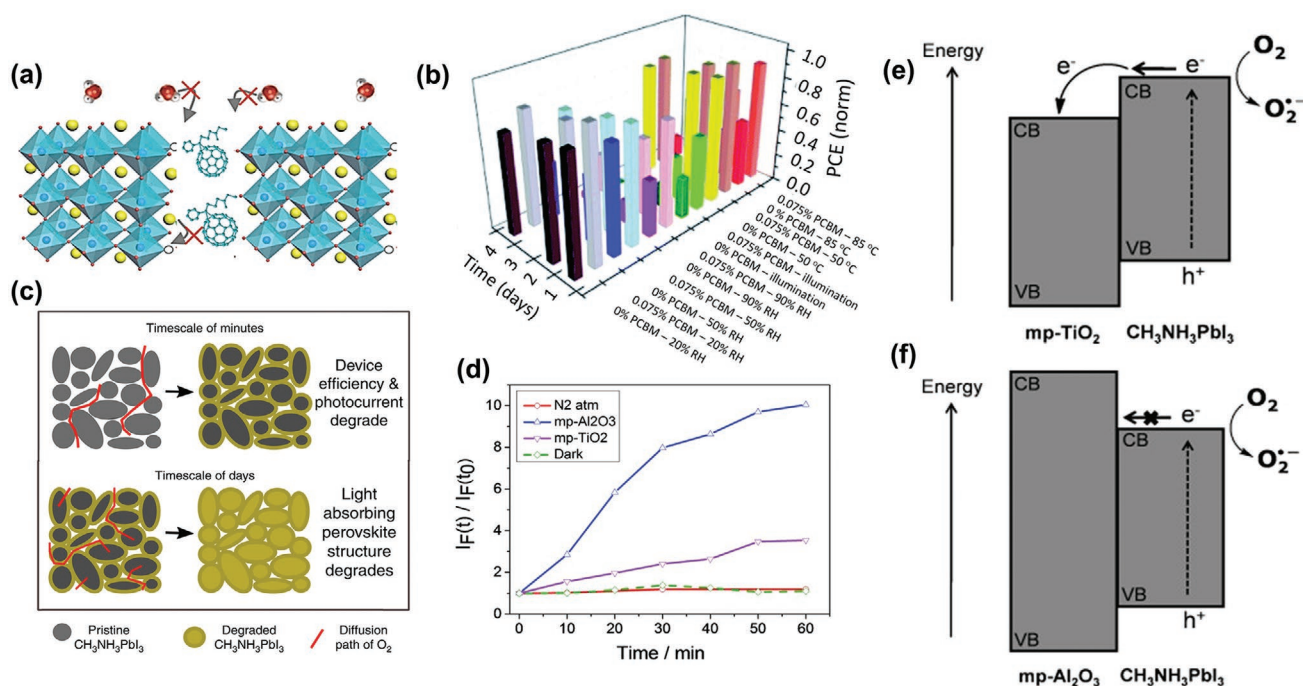


Figure 10. a) Schematic of PCBM blocking the infiltration of water molecules between grains. Adapted with permission.^[77] Copyright 2018, Wiley-VCH. b) Degradation of perovskite and perovskite:PCBM (0.075%) films under various conditions. Adapted with permission.^[104] Copyright 2019, Royal Society of Chemistry c) Path of oxygen ingress in perovskite leading to degradation of the film via superoxide (O_2^-) formation.^[107] d) O_2^- yield via tracking fluorescence quenching of a hydroethidine O_2^- probe solution. e,f) Energetics of O_2^- formation via oxidation of perovskite excited state deposited on e) mp-TiO₂ and f) insulating Al₂O₃. Reproduced with permission.^[108] Copyright 2015, Wiley-VCH.

will have important implications for the ability of carrier injection into the O_2 LUMO to kinetically compete with rapid carrier extraction into the bulk CTL. The yield of highly destructive superoxide formation is thus likely reduced and affords the structures greater tolerance to oxygen in the presence of light. Furthermore, Lin et al. revealed the formation

of O_2^- could be reversed back to oxygen in the presence of fullerene-based acceptors due to a lower lying LUMO in the CTL.^[109] A potential mechanism is proposed (Figure 11) to explain the improved tolerance to oxygen under illumination and stimulate further work into understanding superoxide yields in BHJs.

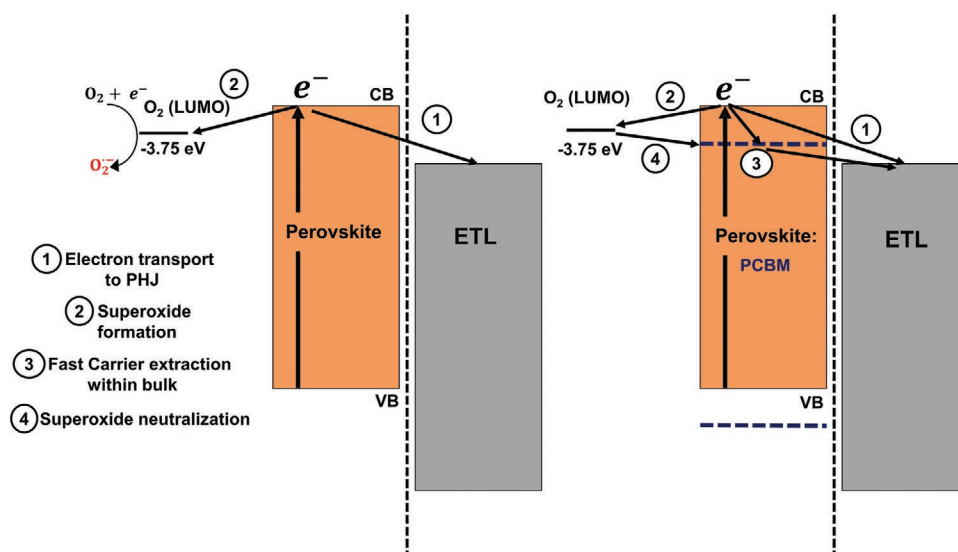


Figure 11. Proposal of mechanism of superoxide (O_2^-) formation in a perovskite/ETL planar heterojunction. In the BHJ film (right) competing pathways to deplete the perovskite photoexcited state (3) reduce the number of carriers with lifetimes long enough to form superoxide. Superoxide may then be neutralized by oxidation with the low lying PCBM LUMO.

We note that the formation of perovskite:CTL BHJs remains at an early stage of development with a series of unknowns still shrouding the exact carrier transport mechanisms. Further work should investigate key parameters such as the ability of CTL to form inter-grain CTL network. More specifically, further understanding is needed on the importance of mobility matching carriers and network formation between the blended and sandwiching CTLs to ensure effective transport from the active layer to the metal contact. Surprisingly, BHJ have exhibited remarkably high resistance to shunting despite the hypothesized formation of an intergrain network. The origin of this resistance to the formation of shorts through the device requires further investigation and possible optimization with insulating blocking layers.

Reviewing the available literature on various CTL materials, inorganic NPs have emerged as the most promising candidate for further optimization into high efficiency devices with PCEs beginning to exceed 20%.^[90,91] This value can be further improved through further optimization of the device such as the perovskite composition and further optimization of the NP composition and size, in addition to optimizing balanced carrier extraction. While yet to reach the PCEs showcased by inorganic NPs, the ability to functionalize organic CTLs offers opportunities to both stabilize and intimately passivate the perovskite films that can be further exploited.

3. Perovskite Graded Heterojunctions

3.1. Blended Perovskite Graded Heterojunctions

Grading of the band gap energies is a promising route for improving the performance of photovoltaics and has been widely discussed across a range of mature photovoltaic technologies such as $\text{CuIn}_{1-x}\text{Ga}_x\text{Se}_2$ (CIGS), $\text{Cu}_2\text{ZnSn}(\text{S}_x\text{Se}_{1-x})_4$ (CZTSSe), silicon and group III–V inorganic semiconductors. Recently, PSCs prepared with a CTL concentration gradient within the perovskite layer have been identified as a promising approach to influence the band edge grading and tune the electric fields within the light harvesting region (Figure 1h). While potentially ambiguous, the films prepared with CTL in the antisolvent are considered a different architecture to the established planar thin film stacks owing to the distribution of the CTL within the film rather than a planar interface. For the same reason, the graded structures are considered separate from surface treatments which predominantly modify the surface of a planar interface rather than forming a localized graded heterojunction in the bulk.

To form a grading effect within the active region, a CTL is dissolved within a perovskite antisolvent solution which is subsequently deposited during the washing stage of a one-step perovskite fabrication method (Figure 12a).^[110] The resultant CTL distribution has been characterized using ToF-SIMS and EDX mapping revealing a compositional gradient of additive increasing steadily from towards the top interface (Figure 12b,c).^[110–114] Similar to the un-graded BHJ structure, the GHJ architecture promotes an increase in grain size and crystallinity while also enabling intimate passivation of point defects within the perovskite film.^[77,115] However, the ability to manipu-

late the band energetics within the film to modify the carrier collection is a key advantage of the GHJ and opens the door to new opportunities in band gap engineering of PSCs, following in the footsteps of mature PV technologies.^[110,113,114,116,117] In this section, comparisons are first made between the similarities of the graded and un-graded (BHJ) approaches, such as the formation of large crystalline grains and stability improvements, before providing a discussion on the early progress into the new opportunities afforded by band gap engineering in GHJ architectures through forming a CTL concentration gradient such as the replacement of less stable HTLs.

Similar to the precursor modified BHJ previously discussed, addition of a CTL material within the perovskite anti-solvent washing step promotes formation of large, highly crystalline perovskite grains (Figure 12d,e).^[119–121] Unlike the BHJs, the delayed introduction of the CTL during the antisolvent washing means that the CTL has a reduced ability to influence the nucleation of the perovskite. Instead, the ability to form large crystalline grains in graded perovskite films is attributed to the ability of the graded CTL to extend beyond, and thereby encapsulate the perovskite layer prior to annealing. The formation of a thin CTL layer covering the perovskite during the perovskite annealing acts to slow the release of solvents, slowing the growth and dramatically increasing the perovskite grain size (Figure 12f,g).^[118] Consequently, films prepared with a graded CTL exhibit a striking resemblance to perovskite films fabricated with annealing occurring after deposition of a planar PCBM layer (Figure 12h,i).^[115,118]

The choice of antisolvent used to prepare GHJs was investigated by Ha et al. who identified surprising variations between various antisolvents and the properties of the graded heterojunction. Upon changing the PCBM-antisolvent solution from chlorobenzene to toluene the extent to which the CTL gradient extend out the perovskite and form a capping layer was revealed to increase from 50 to 60 nm, respectively. The formation of a thicker PCBM surface layer using a toluene solvent system more effectively slowed the release of DMF and DMSO during perovskite annealing and growth, yielding larger perovskite grains compared to the GHJ prepared using chlorobenzene. However, by forming larger perovskite grains using toluene, the extent to which PCBM can be spatially distributed within the perovskite bulk was significantly reduced.^[119] Consequently, the perovskite films prepared with smaller grains and an extended graded region via chlorobenzene:PCBM antisolvent washing outperformed the PSCs prepared with toluene:PCBM antisolvent washing, achieving PCEs of 16.4% and 13.8%, respectively. Interestingly, the addition of a thin PCBM layer further improved the chlorobenzene:PCBM based film, reaching PCEs of up to 18.3% in the inverted architecture.^[115]

In addition to increasing the grain size, the high concentration of CTL at the top perovskite interface in GHJ PSCs, also presents opportunities to form a hydrophobic barrier within the PSC, affording increased tolerance to moisture. Using this strategy, Niu et al. demonstrated that a range of commercially available CTLs such as ITIC, PCBM and DTS(FBTTh₂)₂ can significantly improve the hydrophobicity of perovskite films. Conducting contact angle measurements, the authors observed an increase in contact angle at the perovskite water interface from

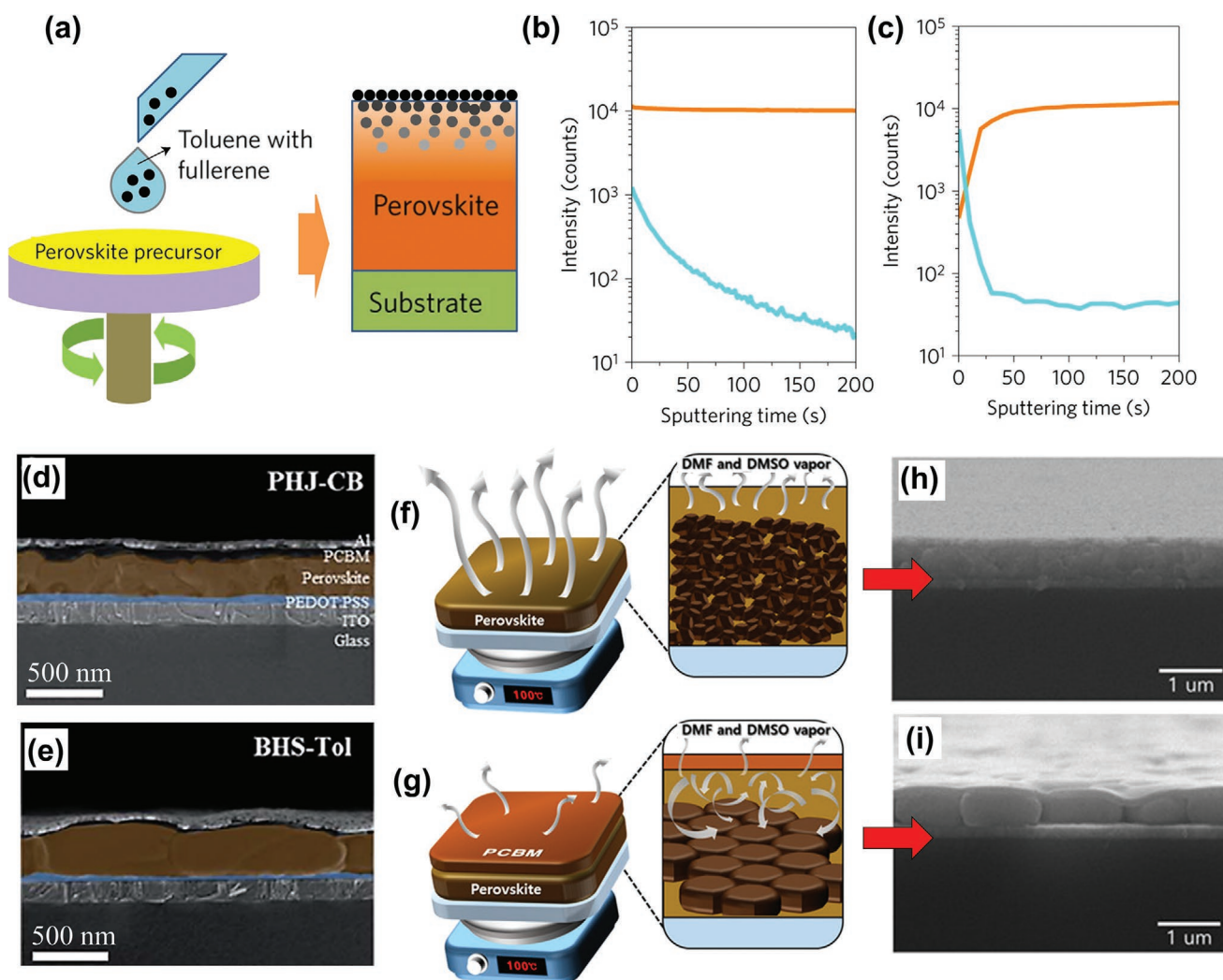


Figure 12. a) Schematic of GHJ formation via addition of a fullerene within a toluene antisolvent washing solution.^[110] b,c) ToF SIMS profiles of perovskite:PCBM GHJ and perovskite/PCBM PHJ respectively. Reproduced with permission.^[110] Copyright 2016, Springer Nature d,e) Cross sectional SEM images of PSCs formed with a perovskite/PCBM PHJ and perovskite:PCBM GHJ respectively. Adapted with permission.^[115] Copyright 2019, Royal Society of Chemistry. f) Conventional perovskite annealing process allowing rapid release of DMF and DMSO. g) Annealing of perovskite post PCBM deposition slowing release of DMF and DMSO. h,i) Cross sectional SEM of perovskite films prepared annealing with and without a PCBM layer, respectively. Adapted with permission.^[118] Copyright 2017, American Chemical Society.

58.7° to 111.9° in the graded architecture as the water seeks to reduce contact with the increasingly hydrophobic perovskite film.^[77]

Alternatively, stability can be further improved through functionalizing fullerenes to afford impressive control of the perovskite surface hydrophobicity in GHJ architectures. Using this approach, Fu et al. modified C₆₀ fullerenes with polyethylene glycol (PEG) to create a highly hydrophobic graded perovskite layer. Dissolved in chlorobenzene and deposited during the perovskite spin coating step, the modified fullerene-based PSCs exhibited greater stability than the pristine control samples, retaining impressive 86% of initial PCE after 40 days in ambient conditions (25 °C; 60% RH) compared to a PCE of 0% after 35 days in the control. Interestingly, the modified fullerene devices exhibited improved stability compared to the much discussed perovskite:PCBM graded PSCs which retained around 60% of their initial PCE after 40 days in the

same conditions.^[121] Contrastingly, Xu et al. opted to increase the hydrophobicity of a fullerene to create an amphiphilic CTL capable of both coordinating to the perovskite, passivating defects, while synergistically repelling moisture from the hydrophobic fullerene tail. The multipurpose fullerene additives effectively improved the stability enabling devices to retain 98.4% of initial PCEs in a high humidity (25 °C; 80% RH) environment after 300 h, over 10% higher than the control.^[111]

Complimenting improvements to the stability, the ability to modify the band gap in GHJ architectures is a key advantage in comparison to BHJ architectures and affords new opportunities in PSC engineering and optimization.^[110,113,114,116,117] In PV technologies such as CIGS and CZTSe, devices constructed with the additional built-in potential promote self-driven carrier separation within the perovskite layer and improve spectral overlap thereby enhancing the photocurrent.^[29,30,122–124]

Additionally, the formation of back surface fields has proven an effective strategy in silicon PV to increase V_{oc} and FF through creating regions of highly localized band grading around the contacts. The localized electric field directs minority carriers away from the interface reducing non-radiative recombination.^[125,126] Recently, the formation of perovskite GHJ architectures has been identified as an approach to enable early studies into perovskite band gap grading. Wu et al. first suggested that the formation of graded CTL heterojunctions may improve the charge collection efficiency and reduce recombination in PSCs. Probing the band structure of the perovskite:PCBM graded architecture through UV photoelectron emission spectra (UPS) revealed VB edges of 5.99 and 5.48 eV for pristine MAPbI₃ and PCBM films, respectively. Interestingly, through varying the

PCBM concentration in the antisolvent solution, an almost linear response between the VB drop and the extent of PCBM grading was recorded (Figure 13a). Combined with no change in the optical band gap, the authors identified a combined lowering of the perovskite VB and CB edges proportional to PCBM concentration, ideal for promoting carrier drift at the interface (Figure 13b). Consequently, the work clearly identified the ability of CTLs to manipulate the perovskite band structure as a function of composition, a key observation. Ultimately, large area PSCs (1.022 cm²) prepared with a GHJ outperformed those with PHJ, exhibiting a remarkable improvement across all photovoltaic parameters from PCE of 11.3%, J_{sc} (17.90 mA cm⁻²), V_{oc} (0.93 V), and FF (69%) to PCE of 18.2%, J_{sc} (21.98 mA cm⁻²), V_{oc} (1.08 V), and FF (79%).^[110]

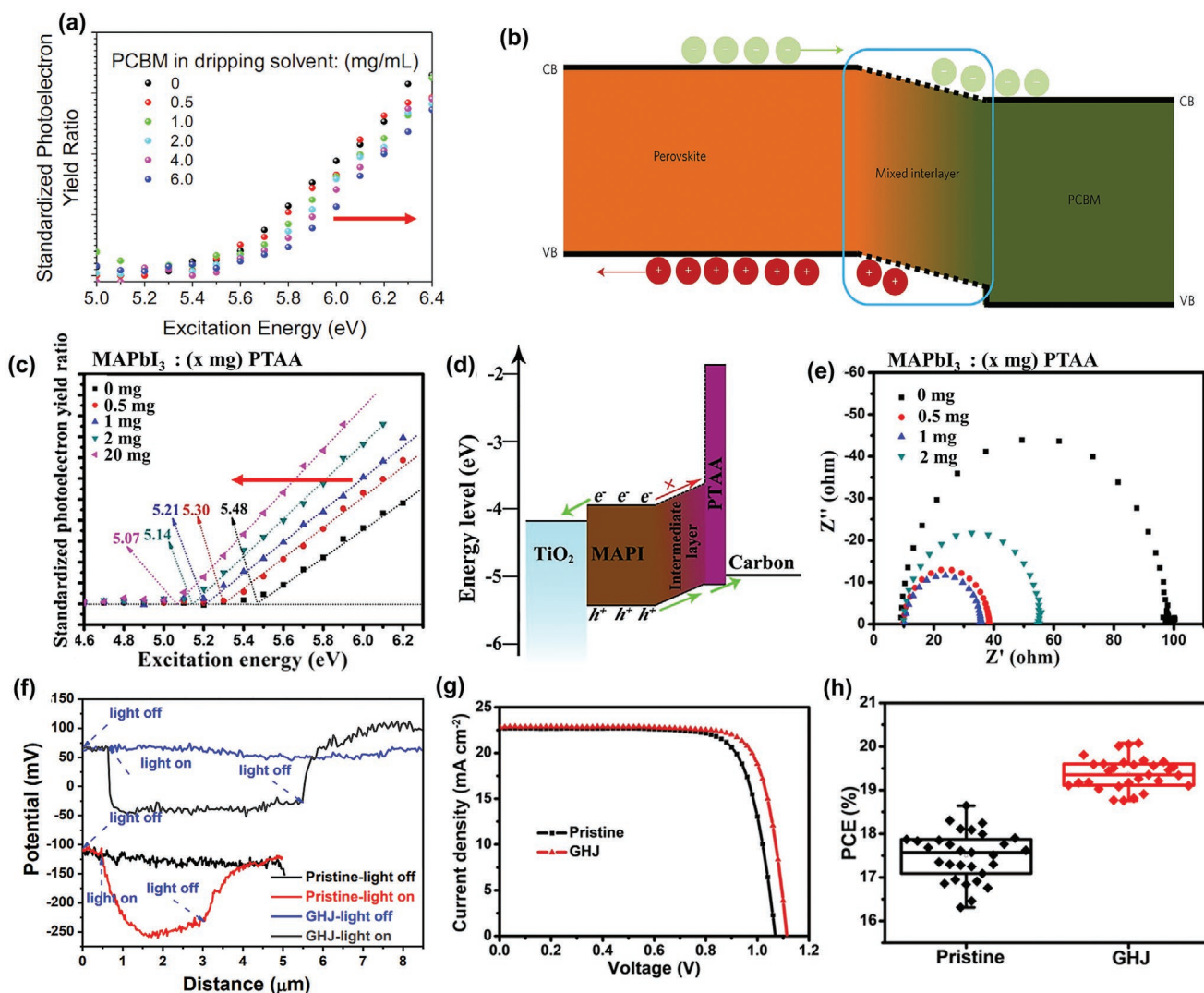


Figure 13. a) UPS data of perovskite:PCBM films with varying PCBM concentrations from 0 to 6 mg mL⁻¹. b) Schematic of perovskite band edges shifting with increasing PCBM concentration in the GHJ architecture. Adapted with permission.^[110] Copyright 2016, Springer Nature. c) UPS data perovskite:PTAA films formed with varying concentrations of PTAA. d) Band energies of the PSC prepared with MAPbI₃:PTAA GHJ. e) EIS spectra with Nyquist plots of with different concentrations of graded PTAA. Adapted with permission.^[114] Copyright 2018, American Chemical Society. f) Line scans of the surface potential of pristine control perovskite and perovskite formed with a PTAA GHJs with lights on and off. g) J–V curves of PTAA graded GHJ and PHJ. h) Statistical data of PCEs of devices prepared with and without a PTAA GHJ. Reproduced with permission.^[116] Copyright 2018, Wiley-VCH.

Ma et al. further probed the effects of ETL graded heterojunctions on the behavior of carriers, replacing PCBM in favor of IDIC, a Lewis basic non-fullerene acceptor. The formation of a IDIC graded region towards a MAPbI₃/PCBM planar interface assisted electron drift across the perovskite film, enabling faster carrier extraction from the PSC relative to the planar heterojunction. Consistent with the formation of a carrier directing back-surface field, TPV measurements revealed an extended photovoltage decay in graded PSCs, owing to reduced recombination and higher carrier mobility. Devices prepared with additional IDIC grading outperformed the MAPbI₃ control improving average PCE from 15.5 to 17.9%.^[127]

More recently, Xu et al. modified the fabrication method of GHJ PSCs using a two-step process. Combining the PCBB-OEG with the methylammonium iodide solution prior to dropping onto a PbI₂ film, the authors produced a graded composition of CTL within the perovskite film.^[111] In good agreement with the previously discussed studies, addition of the fullerene led to lowering the surface potential of the modified perovskite film. Consequently, impedance measurements on the complete devices identified reductions in both charge transfer and series resistance, facilitating an improvement in FF from 70% in the PHJ to 80% in the GHJ. Ultimately, the fullerene graded MAPbI₃ based PSCs exhibited improved performance compared to a planar MAPbI₃ control device yielding PCEs of 20.2% and 16.7%, respectively. Notably, the improvement in carrier transport and extraction increased the FF from 70% in the PHJ to 80% in the GHJ.

In an interesting approach, Zhang et al. incorporated α -bis-PCBM to the antisolvent washing solvent to form a graded ETL layer in an n-i-p architecture.^[78] While it could be expected the presence of a ETL in close proximity to the HTL spiro-OMeTAD layer would increase non-radiative recombination and shunt the device, curiously the PSCs exhibited significantly improved performance. In particular, the devices exhibited fast electron extraction into the graded fullerene CTL and a reduction in series resistance. Like the role of an additional drift current, the proximity of the CTL to the HTL interface is effective in reducing the electron concentration towards the HTL interface via spatially separating the carriers. In doing so non-radiative recombination is decreased. The early graded heterojunctions showcased PCEs of 20.8%, 19.9%, and 18.8% in perovskite films prepared with α -bis-PCBM, PCBM and no grading, respectively.

Simultaneously, several studies have also attempted to grade spiro-OMeTAD within the perovskite as a more intuitive approach to form graded n-i-p PSCs. Fabrication of spiro-OMeTAD GHJs present a challenge compared to fullerenes owing to the detrimental impact of hygroscopic Li dopants on the perovskite film stability. Consequently, the dopant-free spiro-OMeTAD graded perovskites are most often prepared.^[128,129] Using this approach, Chen et al. incorporated undoped spiro-OMeTAD directly into the antisolvent forming a p-type CTL within the perovskite film. While the films produced did not require a second HTL layer fabrication step and simplified the PSC fabrication, the absence of dopants limited PCEs to just 13.2%, improving to 15.5% upon further addition of poly(methyl methacrylate) (PMMA) to the antisolvent solution. Spin coating a secondary planar Li-doped spiro-OMeTAD film on an undoped perovskite: spiro-OMeTAD GHJ ena-

bled Tu et al. to further optimize the PCEs of the devices. In this work, the authors measure TRPL lifetimes of the spiro-OMeTAD graded perovskite to reveal that hole extraction occurs from perovskite into the graded spiro-OMeTAD within the active region. The PSCs prepared using the graded spiro-OMeTAD perovskite reached PCEs of up to 19.1%, significantly outperforming the PHJ control of 16.8%.^[113] It is likely that the addition of a sequential doped spiro-OMeTAD layer above the undoped graded region plays a key role in promoting high efficiency with Li ions previously reported to diffuse between perovskite grain boundaries from a planar layer.^[130] Recently, Taherianfard et al. demonstrated a novel alternative approach to grade Li doped spiro-OMeTAD within the perovskite thin film via a acetonitrile (ACN) solvent treatment which acts to dissolve the upper layer of perovskite. The solvent modified graded heterojunctions report a PCE of up to 19.7%.^[131]

As an alternative to spiro-OMeTAD, poly(triaryl amine) PTAA has also been identified as a promising p-type material for producing GHJs. Like the work of Wu et al. on PCBM GHJs, Han et al. observed a reduction in the VB energy as a function of PTAA concentration, further highlighting how the incorporation of CTLs within the perovskite layer locally modifies the energetics of the perovskite film (Figure 13c). The formation of an upward gradient in the band edges promotes the drift of holes towards the carbon electrode while directing electrons away reducing recombination at the interface (Figure 13d). Impedance spectroscopy conducted on the devices revealed significantly improved carrier transport in the GHJ with resistance significantly lowering with additional PTAA (Figure 13e). Furthermore, the authors also reported a similar trend conducting SCLC measurements, identifying an enhancement of hole mobility with increasing PTAA concentration, significantly reducing recombination within the film. Completing the device with a carbon electrode doctor-bladed onto the PTAA capped perovskite and Au metal contact, the authors reported a champion PCE of 13.0% compared to the 10.3% reference cell. KPFM studies further confirmed the formation of a graded region when adding PTAA to the antisolvent, noting a reduced surface potential in the p-type graded film (Figure 13f). Investigating the recombination mechanisms in the graded and ungraded film, the authors reveal negligible changes in bimolecular recombination. However, photovoltage against illumination intensity plots revealed significantly reduced trap-assisted recombination in the graded architecture. Accordingly, PSCs prepared using the PTAA GHJ exhibited an improved V_{oc} from 1.07 to 1.11 V (Figure 13g). These improvements enabled the double cation GHJs to improve PCE from 18.6% in the control up to 20.0% in the PTAA graded architecture (Figure 13h).

Most recently, Li et al. investigated using functionalized polymers in an approach to eliminate the need for spiro-OMeTAD, which is known to limit device stability, within the PSCs while retaining high photovoltaic performance. Through functionalizing a polybithiophene (PBT) base polymer with additional electron rich oxygen and fluorine groups (PBTFO), the authors effectively encourage passivating interactions between the Lewis basic thiophene, fluorine and oxygen groups, with Pb²⁺ cations of the perovskite evidenced through a combination of Raman and X-ray photoelectron spectroscopies.

Consequently, the PTBFO yielded a promising champion PCE of 22.1% with low photovoltage losses ($V_{oc} = 1.22$ V with respect to $E_g = 1.60$ eV) compared to 19.0% using a spiro-OMeTAD PHJ. In addition to improving photovoltaic parameters, the undoped PTBFO significantly improved stability retaining 92% of initial PCEs (20.3%) after a period of 500 h under illumination in ambient conditions (unencapsulated; 25 °C; 20–60% RH; 100 mW cm⁻²) compared to spiro-OMeTAD which degraded PCEs to 4.1% within 100 h. The authors thus highlighted a promising strategy in developing stable, efficient and undoped alternatives to spiro-OMeTAD while highlighting the promise of developing new GHJ structures.^[132]

The fabrication of graded heterojunctions via addition of CTL within an antisolvent treatment has a profound effect on the photovoltaic characteristics of PSCs (Table 1). Like the BHJ, addition of a CTL within the perovskite films reduces density of trap states within the film via the formation of larger and grains and intimate passivating interactions. Such reductions in trap state density in GHJs have frequently been identified using a range of techniques such as XPS, thermal admittance spectroscopy and SCLC.^[77,112,127] The formation of localized back surface field-like structures further reduces the non-radiative recombination within the films through spatially separating carriers at the interface where the largest density of trap states are located. In addition to the impressive performance, the formation of GHJs is also a promising new direction for the development of new HTLs suitable for use with PSCs which offer greater stability than spiro-OMeTAD and higher PCEs than carbon electrodes-based devices. Alternatively, grading of the band gap has also been recently reported using non-CTL species capable of interaction with the Pb²⁺ 4f orbitals forming a gradient in the band edges, reporting PCEs of up to 22.1%.^[133,134] From these works, it is evident that formation of GHJ makes a compelling case for simple engineering of the perovskite band energetics enabling synergistic passivation of the perovskite through highly crystalline perovskite grains and self-driven carrier separation, while also addressing key practicalities such as stability.

3.2. Perovskite:Perovskite Graded Heterojunctions

The formation of perovskite:perovskite graded heterojunctions within the absorber layer of PSCs has recently gained significant attention as a strategy to produce PSCs with high PCEs. To form the perovskite:perovskite GHJ, a secondary compositionally varied perovskite material is deposited sequentially upon a primary perovskite substrate (Figure 1i). Controlling the composition in this way represents a useful method to facilitate engineering of the band gap, resembling the composition grading previously used in mature photovoltaic technologies.^[29,122] Several methods have so far been used to implement the secondary perovskite film and form the desired grading effect. This section begins by first discussing QD GHJ approaches (Figure 14a,b) which are leading the way in quantum dot solar cells before discussing recent progress in secondary perovskite thin films (Figure 14c). Finally, the recent breakthroughs in device efficiency and stability achieved using 2D/quasi 2D GHJ PSCs are discussed.

Amongst the earliest of approaches in producing graded perovskite heterojunctions, perovskite quantum dots have become a useful building block for producing highly controlled GHJs in PSCs (Figure 14a). The ability to exert control over the band gap and particle size has made QDs ideal for creating compositionally complex graded architectures. This can be achieved by either casting the dots onto a perovskite thin film as an interfacial layer or by using a layer-by-layer deposition of QDs directly onto a CTL with varying QD composition for each layer (Figure 15a). The latter of these approaches was investigated by Bian et al. who created a perovskite film with a gradient in composition from CsPbBr₂I to CsPbI₃ through spin coating sequential layers of QDs. The formation of band grading within the film played two key roles first improving the J_{sc} through addition of a narrower band gap perovskite phase (Figure 15b). Second, the V_{oc} of the films was improved owing to enhanced carrier separation. Optimization of the thickness ratio of the layers enabled a PCE up to 14.4% for a 300 nm:300 nm, when the heterojunction was located in the center of the CsPbI₂Br:CsPbI₃ active layer.^[140]

More recently, this approach was revisited by Zhao et al. who confirmed that forming a heterojunction at the center of the light absorbing layer was optimal for PCE performance. Such reports suggests that a central heterojunction may be a superior approach to the back surface field-like structure, however further theoretical work is required to verify the optimum heterojunction location within the active region. TAS measurements conducted on the central QD GHJ interface revealed that fast electron transfer occurs between the wide band gap CsPbI₃ (697 nm) to Cs_{0.25}FA_{0.75}PbI₃ (728 nm) on the order of 600 ps. (Figure 15c). The PSCs prepared using the CsPbI₃(QD):Cs_{0.25}FA_{0.75}PbI₃(QD) GHJ showcased a remarkable PCE 17.4% surpassing the record PCE for a pure QD solar cell of 16.6%.^[141]

Recently, the use of the layer-by-layer approach to produce compositionally graded perovskite films has become a promising strategy for the fabrication highly efficient quantum dot solar cells with PCEs reaching up to a record 17.4%.^[141,146] However, the champion PCEs of the layer-by-layer QD GHJ architecture continues to fall short of the high PCEs recorded using bulk perovskite thin films which frequently surpass 20%. The additional losses in the pure QD solar cells are a result of resistive interfaces between QDs. These challenges can be overcome by using a perovskite thin film rather than a pure QD film for either one or more of the perovskite layers (Figure 14b).^[143–145,147,148]

Early attempts to produce a perovskite QD heterojunction on a thin film substrate were conducted by Cha et al. with limited success observing a modest improvement in FF from 61% to 72%. Subsequent works identified the use of CsPbX₃ QDs as promising for producing high efficiencies using the architecture.^[149,150] A key breakthrough in improving the efficiency was realized by Zai et al. who modified the fabrication process to incorporate perovskite CsPbBr₃ QDs into the antisolvent washing stage prior to annealing (Figure 15d). Upon contact with the wet perovskite film the quantum dots lose structural integrity and diffuse within the films. The diffusion of QDs into the planar film induced a compositional gradient within the perovskite film, which has since been observed

Table 1. Summary of photovoltaic parameters of perovskite GHJs (in **bold**) and the reference PHJs.

GHJ/PHJ device structure	J_{sc} [mA cm ⁻²]	V_{oc} [V]	FF	PCE [%]
ITO/NiO _x /FA _{0.85} MA _{0.15} Pb(I _{0.85} Br _{0.15}) ₃ :PCBM/Nb-TiO ₂ /Ag	21.9	1.08	0.79	18.7 ^[10]
ITO/NiO _x /FA _{0.85} MA _{0.15} Pb(I _{0.85} Br _{0.15}) ₃ /Nb-TiO ₂ /Ag	17.9	0.93	0.68	11.3 ^[10]
ITO/PEDOT:PSS/MAPbI ₃ :PCBM/PCBM/AI	23.7	0.96	0.76	17.7 ^[15]
ITO/PEDOT:PSS/MAPbI ₃ /PCBM/AI	17.0	0.92	0.74	11.2 ^[15]
ITO/PEDOT:PSS/MAPb _{0.5} Sn _{0.5} I ₃ :DF-C ₆₀ /C ₆₀ /Bis-C ₆₀ /Ag	23.6	0.68	0.69	11.0 ^[35]
ITO/PEDOT:PSS/MAPb _{0.5} Sn _{0.5} I ₃ /C ₆₀ /Bis-C ₆₀ /Ag	21.6	0.52	0.65	8.0 ^[35]
FTO/c-TiO ₂ /mp-TiO ₂ /Cs _{0.05} FA _{0.79} MA _{0.16} :Spiro-OMeTAD/Spiro-OMeTAD/Au	23.0	1.09	76.4	19.2 ^[31]
FTO/c-TiO ₂ /mp-TiO ₂ /Cs _{0.05} FA _{0.79} MA _{0.16} /Spiro-OMeTAD/Au	22.6	1.05	73.9	17.8 ^[31]
FTO/TiO ₂ /Cs _{0.06} FA _{0.78} MA _{0.16} PbI _{0.85} Br _{0.15} :Spiro-OMeTAD/Spiro-OMeTAD/Au	23.0	1.10	0.76	19.1 ^[13]
FTO/TiO ₂ /Cs _{0.06} FA _{0.78} MA _{0.16} PbI _{0.85} Br _{0.15} /Spiro-OMeTAD/Au	22.1	1.07	0.71	16.8 ^[13]
FTO/NiO _x /MAPbI ₃ :PTAA/Carbon	21.4	1.02	0.59	13.0 ^[14]
FTO/NiO _x /MAPbI ₃ /PTAA/Carbon	20.5	1.01	0.50	10.3 ^[14]
FTO/TiO ₂ /Cs _{0.2} FA _{0.8} PbI _{2.75} Br _{0.15} :PTAA/Spiro-OMeTAD/Au	22.8	1.15	0.79	20.0 ^[16]
FTO/TiO ₂ /Cs _{0.2} FA _{0.8} PbI _{2.75} Br _{0.15} /Spiro-OMeTAD/Au	22.7	1.07	0.77	18.6 ^[16]
FTO/Li-NiO _x /MAPbI ₃ :iDIC/PCBM/BCP/Ga ₂ O ₃ /Ag	21.0	1.12	0.76	17.9 ^[27]
FTO/Li-NiO _x /MAPbI ₃ /PCBM/BCP/Ga ₂ O ₃ /Ag	19.8	1.09	0.71	15.5 ^[27]
FTO/TiO ₂ /Cs _{0.05} MA _{0.81} FA _{0.14} PbI _{2.55} Br _{0.45} :Pc/Spiro-OMeTAD/Au	22.2	1.16	75.4	19.3 ^[36]
FTO/TiO ₂ /Cs _{0.05} MA _{0.81} FA _{0.14} PbI _{2.55} Br _{0.45} /Spiro-OMeTAD/Au	21.80	1.13	71.0	17.5 ^[36]
FTO/TiO ₂ /MAPbI ₃ :PTB7:ITIC/Spiro-OMeTAD/MoO ₃ /Au	24.2	1.10	76.0	20.0 ^[12]
FTO/TiO ₂ /MAPbI ₃ /Spiro-OMeTAD/MoO ₃ /Au	21.3	1.08	73.0	16.7 ^[12]
ITO/NiO _x /Cs _{0.1} FA _{0.7} MA _{0.2} PbI _{3-x} Br _x :C ₆₀ -PEG/PCBM/BCP/Ag	20.5	1.04	81.7	17.4 ^[21]
ITO/NiO _x /Cs _{0.1} FA _{0.7} MA _{0.2} PbI _{3-x} Br _x :PCBM/PCBM/BCP/Ag	19.3	1.03	77.3	15.7 ^[21]
ITO/NiO _x /Cs _{0.1} FA _{0.7} MA _{0.2} PbI _{3-x} Br _x /PCBM/BCP/Ag	19.0	1.01	75.4	14.4 ^[21]
ITO/PTAA/MAPbI ₃ :PCBB-OEG/PCBM/AI	23.2	1.05	0.78	19.6 ^[11]
ITO/SnO ₂ /Cs _{0.05} FA _{0.81} MA _{0.14} PbI _{2.55} Br _{0.45} :PBT/Au	23.0	1.20	0.74	20.3 ^[32]
ITO/SnO ₂ /Cs _{0.05} FA _{0.81} MA _{0.14} PbI _{2.55} Br _{0.45} :PBTf/Au	23.3	1.21	0.75	21.2 ^[32]
ITO/SnO ₂ /Cs _{0.05} FA _{0.81} MA _{0.14} PbI _{2.55} Br _{0.45} :PBTfO/Au	23.0	1.22	0.79	22.1 ^[32]
ITO/SnO ₂ /Cs _{0.05} FA _{0.81} MA _{0.14} PbI _{2.55} Br _{0.45} /Au	22.5	1.14	0.74	19.0 ^[32]
FTO/TiO ₂ /CsPbI ₃ (QD):PBDB-T/PTAA/MoO ₃ /Ag	15.1	1.22	0.75	13.8 ^[37]
FTO/TiO ₂ /CsPbI ₃ (QD)/PTAA/MoO ₃ /Ag	14.0	1.22	0.77	13.1 ^[37]
FTO/TiO ₂ /FAPbI ₃ (QD):PBDB-T/PTAA/MoO ₃ /Ag	16.7	1.12	0.71	13.2 ^[37]
FTO/TiO ₂ /FAPbI ₃ (QD)/PTAA/MoO ₃ /Ag	14.0	1.12	0.74	11.6 ^[37]
ITO/NiO _x /CsPbI _{3-x} Br _x :6TIC-4F/ZnO/C ₆₀ /Ag	17.7	1.16	0.79	16.1 ^[38]
ITO/NiO _x /CsPbI _{3-x} Br _x /ZnO/C ₆₀ /Ag	17.0	1.10	0.74	13.9 ^[38]
FTO/Mp-TiO ₂ /Cs _{0.06} MA _{0.17} FA _{0.83} PbI _{2.52} Br _{0.48} :CNT/Carbon	18.9	1.00	0.71	13.5 ^[39]
FTO/Mp-TiO ₂ /Cs _{0.06} MA _{0.17} FA _{0.83} PbI _{2.52} Br _{0.48} /Carbon	18.0	0.90	0.6	11.6 ^[39]
FTO/c-TiO ₂ /mp-TiO ₂ /(FA _{0.81} MA _{0.19} PbI _{2.55} Br _{0.45} :α-bis-PCBM/Spiro-OMeTAD/Au	23.9	1.12	0.74	20.8 ^[78]
FTO/c-TiO ₂ /mp-TiO ₂ /(FA _{0.81} MA _{0.19} PbI _{2.55} Br _{0.45} :PCBM/Spiro-OMeTAD/Au	23.7	1.11	0.73	19.9 ^[78]
FTO/c-TiO ₂ /mp-TiO ₂ /(FA _{0.81} MA _{0.19} PbI _{2.55} Br _{0.45} :α-bis-PCBM/Spiro-OMeTAD/Au	23.3	1.09	0.71	18.8 ^[78]
FTO/c-TiO ₂ /MAPbI ₃ :PCBM/Spiro-OMeTAD/Au	21.5	1.07	0.75	18.4 ^[77]
FTO/c-TiO ₂ /MAPbI ₃ :ITIC/Spiro-OMeTAD/Au	22.0	1.07	0.75	19.0 ^[77]
FTO/c-TiO ₂ /MAPbI ₃ :DTS/Spiro-OMeTAD/Au	21.8	1.07	0.74	18.3 ^[77]
FTO/c-TiO ₂ /MAPbI ₃ :DR3T/Spiro-OMeTAD/Au	22.2	1.08	0.75	19.2 ^[77]
FTO/c-TiO ₂ /MAPbI ₃ /Spiro-OMeTAD/Au	21.0	1.06	0.74	17.5 ^[77]

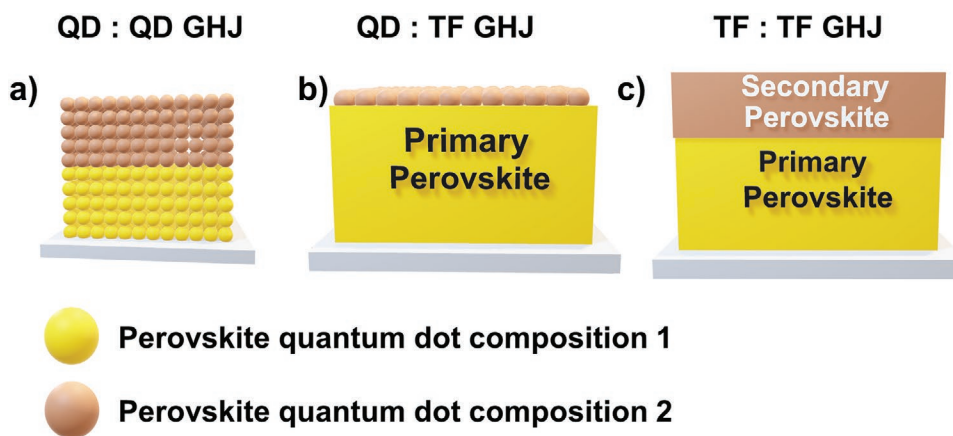


Figure 14. Representation of perovskite: perovskite graded heterojunctions prepared using a) a quantum dot: quantum dot heterojunction, b) a perovskite thin film: quantum dot heterojunction, and c) a perovskite thin-film: thin film heterojunction.

using both ToF-SIMS and angle-resolved XPS (AR-XPS) data (Figure 15c).^[143,144] The QD induced composition gradient was found to reduce the work function at the treated surface, blocking electrons from reaching the HTL while encouraging hole drift (Figure 15e). The carrier transport was investigated using intensity-modulated photocurrent spectroscopy (IMPS) and TPC revealing faster and more efficient hole extraction in the PSCs. In a key observation, the authors report that device PCE was only improved when perovskites with different band gaps were used highlighting the importance of grading effect. Through optimizing the method of QD application, the authors fabricated PSCs with promising PCEs of up to 20.5% compared to the control (17.9%) (Figure 15f).^[143]

Further study and optimization of the architecture found that following the diffusion of Cs-based QDs into the film, the density of mid-gap and shallow traps states could be reduced, owing to the presence of Cs cations.^[144] Additionally, it was found that the ligands used in preparing perovskite QDs self-assemble into a passivating oleic acid layer on MAPbI₃ film surface (Figure 15g). The ligand monolayer afforded the perovskite films enhanced tolerance to water through creating a hydrophobic barrier at the perovskite surface while passivating surface defects on the film (Figure 15h). More recently, Zhang et al. optimized the distribution and coverage through opting for a perovskite nanowire (NW) dispersion. Replacing 0D CsPbBr₃ nanocrystals (NC) for NWs enabled a more uniform grading and diffusion of the secondary perovskite additive species, identified through KPFM scans of the surface. The improvement in coverage led to a PCE increase from 17.4% in the control to 17.6% and 21.4% using NC and NW respectively (Figure 15j).^[145]

Using QD interlayers as a strategy to grade the perovskite composition has rapidly advanced in recent years enabling the fabrication of solar cells with PCEs frequently surpassing 21%.^[144,145,151] While advancements made in optimizing the architecture have been impressive, the additional required synthesis of the perovskite QDs can increase the complexity and thus cost of fabrication for future applications. Instead, IPA solutions containing the relevant cations can be used in the place of QD solutions for a similar and cheaper method for producing the secondary perovskite layer (Figure 14c).

Cho et al. pioneered such a strategy, replacing the QD solution in favor of a FABr/IPA solution which was spin coated onto a FA_{0.85}MA_{0.15}PbI_{2.55}Br_{0.45} film producing secondary perovskite growth of a localized FA⁺/Br⁻ rich phase (Figure 16a,b).^[152] XRD patterns revealed films prepared with the secondary FABr step exhibit reduced PbI₂ as the surface FAPbBr₃ phase is formed (Figure 16c). Measuring the change in band gap at the surface using Kubelka–Munk reflectance revealed a minor shift of 14 meV (Figure 16d).^[148,149] Nevertheless, the graded architectures formed PSCs with superior photovoltaic performance, compared to the untreated planar heterojunction devices with PCEs increasing from 18.7 to 20.5% and a champion PCE of 21.3% (Figure 16e).

More recently, Luo et al. identified the high photovoltages made possible using GHJs could be used as an approach to improve the photovoltage in inverted p-i-n PSCs.^[153–155] In a similar reported mechanism to Cho et al., residual PbI₂ was targeted with a guanidinium bromide (GABr) cation solution to form a smooth wide band gap (WBG) perovskite interlayer, improving photovoltaic performance (Figure 16f). Unlike previous studies, the authors effectively used transient absorption spectroscopy (TAS) to elucidate the behavior of the carriers within the graded perovskite layer. Probing the graded films from the WBG side, a clear redshift in the energy of the transient excited state was observed. This can be attributed to the engineered drift of the photogenerated carriers into the narrower band gap perovskite in the graded films. In the non-gradient control film, no such shift in TAS was observed (Figure 16g,h). The authors thus demonstrate the ability of the device architecture to facilitate self-drive carrier separation via a graded band gap using a secondary perovskite growth approach. Combined with a more n-type film, enabling trap filling, the inverted GHJ PSCs successfully increased the average V_{oc} from 1.10 to 1.20 V, yielding a champion PCE of 21.5%.^[153]

The formation of grading in the film was further reported by Chen et al. who used cross-sectional KPFM measurements to understand the shift in electric field across the PSC architecture. Interestingly, ITO/PTAA/perovskite/PCBM/BCP/Ag devices pinpointed dual depletion regions at the n-i and i-p interfaces (Figure 16i).^[156] In such systems, the dual depletion regions acts as a pair of diodes in series, creating a bottleneck in the

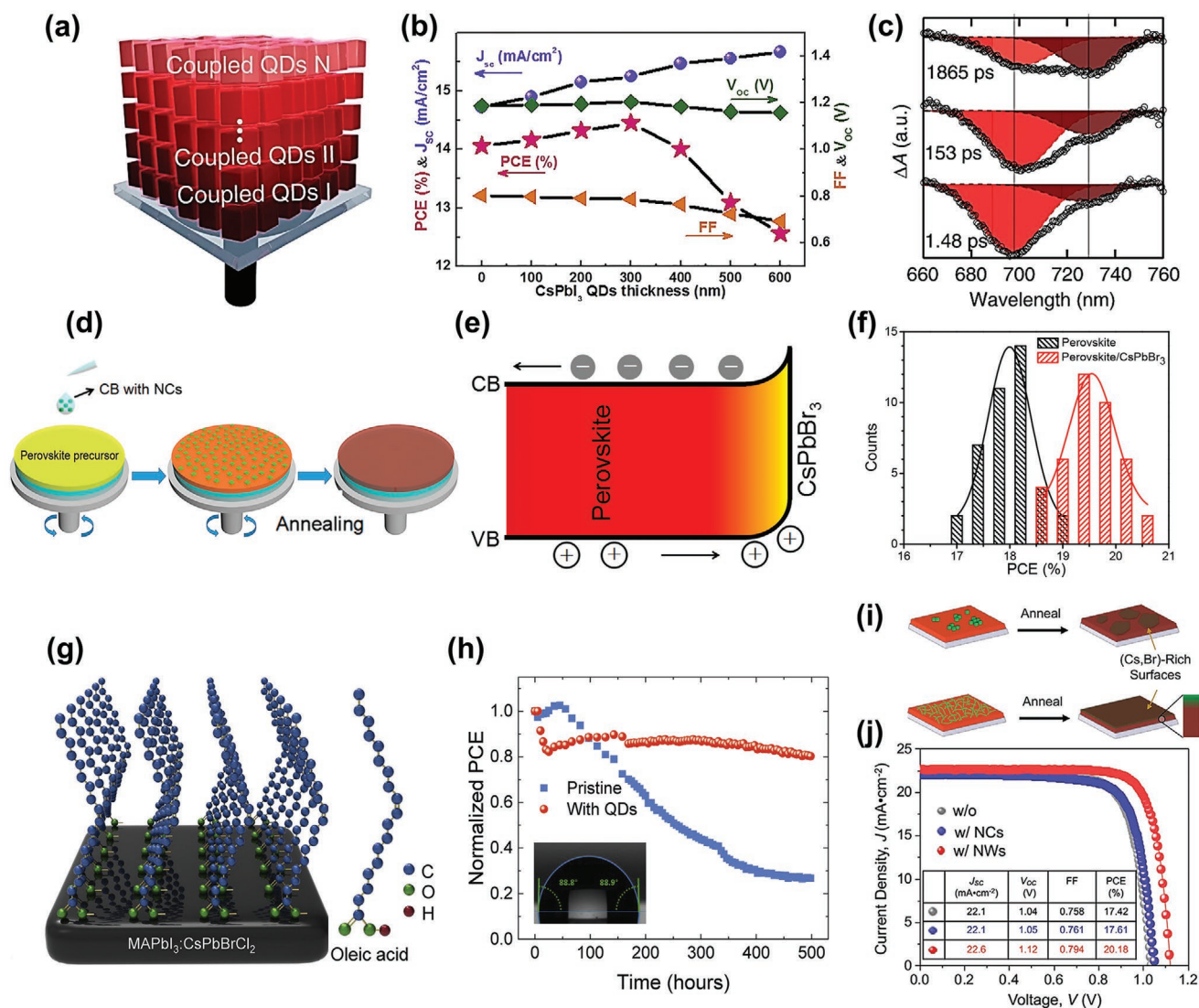


Figure 15. a) Schematic of compositionally varied Perovskite QD film.^[142] b) Photovoltaic parameters of PSCs prepared with varying thickness of CsPbI₃ formed on a 300 nm CsPbI₂Br film. Reproduced with permission.^[140] Copyright 2018, Elsevier. c) TAS of CsPbI₃:Cs_{0.25}FA_{0.75}PbI₃ film excited from the CsPbI₃ side, bleaching at 697 and 728 nm correspond to carriers in CsPbI₃ and Cs_{0.25}FA_{0.75}PbI₃ phases.^[142] d) Fabrication of perovskite QD modified films prior to annealing. e) Band grading in perovskite:CsPbBr₃ (QD) film. f) PCE statistics of PSCs prepared with and without graded CsPbBr₃ QD layer. Reproduced with permission.^[143] Copyright 2018, American Chemical Society. g) Coordination of carboxylic acid groups of Oleic acid following CsPbBrCl₂ QD treatment. h) Normalized PCE of MAPbI₃:CsPbBrCl₂(QD) and MAPbI₃ based PSCs, (Inset) contact angle between CsPbBrCl₂ (QD) treated MAPbI₃ and water. Reproduced with permission.^[144] Copyright 2019, Elsevier i) Schematic of distribution of graded CsPbBr₃ NC and NW on MAPbI₃ film. j) J–V curve of perovskite films prepared with CsPbBr₃ NWs, NCs, and a MAPbI₃ control. Adapted with permission.^[145] Copyright 2019, Wiley-VCH.

equivalent circuit and reducing the photovoltage.^[157,158] Upon addition of a GABr solution, the electronic field distribution was transformed, revealing an extended single dominant junction located at the graded interface promoting improved V_{oc} and FF (Figure 16i).

In a promising and highly innovative adaptation to the architecture, Sun et al. replaced the secondary organic cation solution with SnI₂ for the dripping treatment producing a novel FA_{1-x}MA_xPb_xSn_{1-y}X₃ compositionally graded structure.^[159] The FA_{1-x}MA_xPb_xSn_{1-y}X₃ films exhibited a pronounced band grading, varying from 1.53 eV at the bottom Pb rich film, to 1.27 eV in the top 50 nm where Sn-rich secondary perovskite phases were formed (Figure 14c). In addition to promoting carrier drift through the active region, the addition of a low band gap tin

perovskite phase also increases the capture of lower energy photons. Devices prepared using the APb_xSn_{1-x}X₃ graded architecture showcase highly promising photovoltaic parameters reaching V_{oc} (1.14 V), J_{sc} (25.9 mA cm⁻²), FF (72.6%), and PCE of (21.4%) improving upon the FA_{0.85}MA_{0.15}PbCl_xBr_yI_{3-x-y} control device; V_{oc} (1.11 V), J_{sc} (23.9 mA cm⁻²), FF (73.3%), and PCE (19.4%). Remarkably, the graded device significantly outperformed non-graded mixed tin-lead binary FA_{1-x}MA_xPb_xSn_{1-y}X₃ perovskites reported in the literature, highlighting the opportunities in band gap engineering through the device.^[160] The profound effect of the graded approach on carrier separation and transportation was further demonstrated through producing CTL-free PSCs, in which effective carrier separation must occur within the absorber bulk. The graded CTL-free

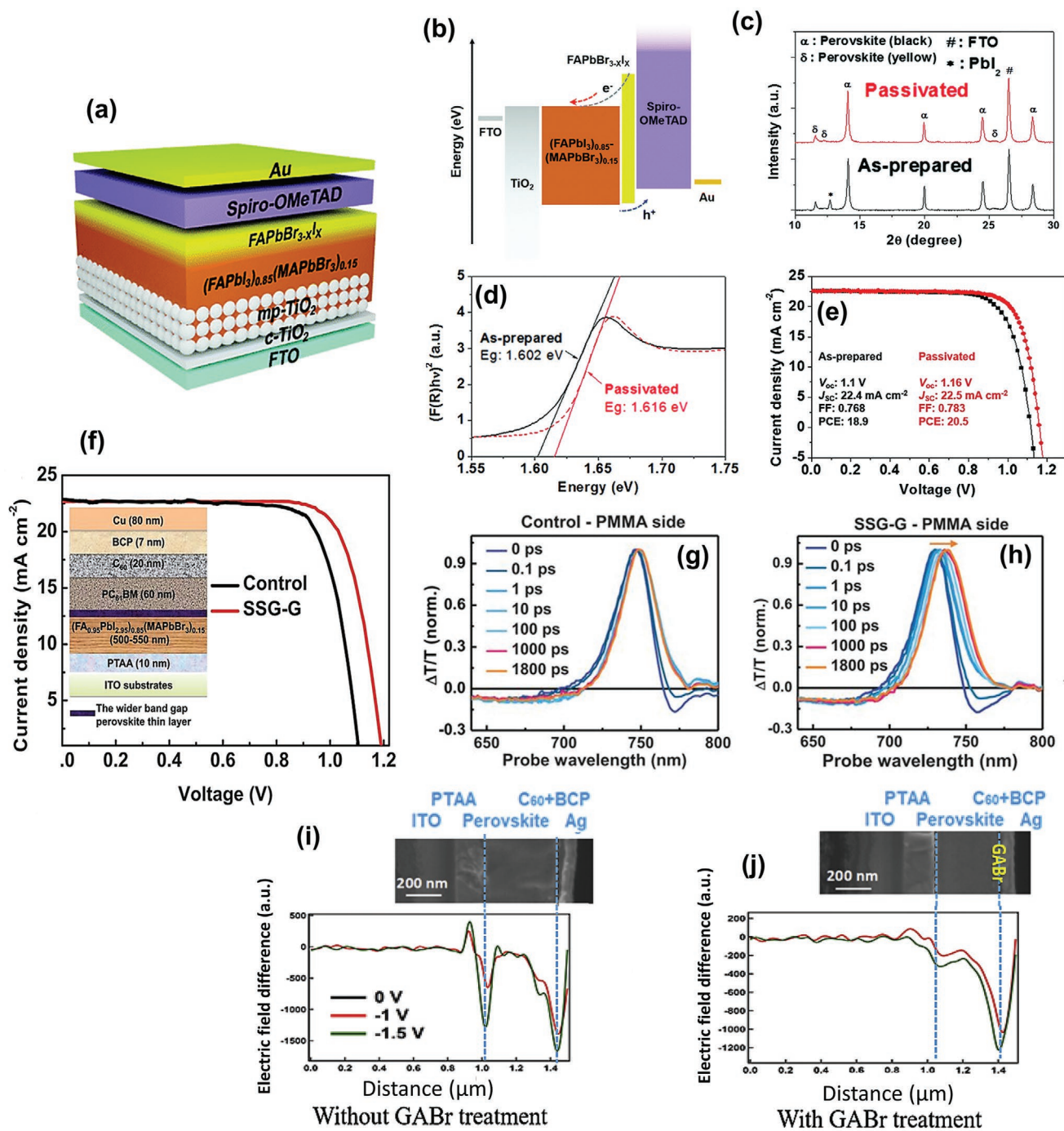


Figure 16. a) Schematic of GHJ device architecture via formation of a FABr rich layer. b) Band gap alignment in the GHJ architecture highlighting the separation of electrons and holes at the back surface. c) XRD of films with and without FABr treatment showing d) Band gap of perovskite film surface calculated using Kubelka Munk method. e) J - V curves of PSCs prepared of FABr GHJ and control FA_{0.85}MA_{0.15}PbI_{2.55}Br_{0.45} film. Reproduced with permission.^[152] Copyright 2017, Royal Society of Chemistry. f) J - V curves of p-i-n films with and without GHJ using GABr secondary solution growth (SSG). g,h) TAS of films prepared of non-graded and graded band gap films excited from the top surface with a 400 nm laser. Adapted with permission.^[153] Copyright 2018, American Association for the Advancement of Science. i,j) Electric field distribution as a function of depth within p-i-n PSCs without and with GABr treatment through cross section KPFM. Adapted with permission.^[156] Copyright 2019, Elsevier.

devices showcased an impressive PCE of up to 10.3%, highlighting the self-driven carrier separation.^[159]

Recently, significant progress has been made developing the thin film graded heterojunctions via engineering the dimensionality of the primary and secondary perovskite to optimize

device performance and stability. Like the lead-tin graded structure, the dimensionally graded structures can offer a high magnitude of band gap grading between the two perovskite components, owing to the tuneable quantum confinement of the carriers within the 2D phase. Early work by Hu

et al. investigated such an approach combining PEAI with MAI as a secondary perovskite solution, forming a 20 nm lower-dimensional Ruddlesden-Popper (RP) 2D phase.^[161] XPS revealed a favorable VB alignment between the 2D perovskite layer and spiro-OMeTAD and large offset in CB to extract holes while blocking electron recombination at the interface and reducing shunting. Such observations have more recently been confirmed using TAS measurements of the 2D/3D interface, enhancing the hole injection into spiro-OMeTAD.^[162] The early PEAI secondary growth devices improved the PCE from 13.6% in the control reference to 16.8% in the graded structure, notably higher than pure 2D devices at the time.^[161]

Optimization of both the organic cation choice and processing parameters quickly led to the reports of higher efficiency devices. Testing a series of phenylalkylamines, Wang et al. identified high performance using Benzylamine (BA), observing a significant increase recombination resistance from 114 to 741 Ω in the graded films. Ultimately device PCE improved upon a control of 14.2% up to 19.2%.^[163] More recently Cho et al. achieved a PCE of 20.1% using a phenylethylamine (PEA) based lower dimensional secondary perovskite reporting favorable hole extraction into the 2D PEA₂PbI₄ layer, decreasing the TRPL decay lifetime.^[164] Like the work of Wang, the authors reported an increase in recombination resistance. Further analysis varying the excitation fluence to manipulate the carrier density between 10^{15} – 10^{17} revealed no significant change in the recombination dynamics of the films.^[164] The findings therefore suggest the influence of the 2D layer on reducing recombination is influenced by encouraging rapid carrier extraction and separation of electrons and holes at an improved interface rather than the passivation of trap states on the film surface. Interestingly, it has also been suggested that the same PEA₂PbI₄ interlayer can effectively improve the device performance efficiency in inverted architectures via forming a thin potential barrier and blocking back recombination between the perovskite and ETL layer (Figure 17a). Using this architecture, Bai et al reported a 70 meV improvement in the photovoltage however the reduction of potential within the active region led to an expected drop in drift current reducing the J_{sc} from 22.5 to 21.8 mA cm⁻².^[165] Further work to minimize recombination losses across the interface using the inverted 2D graded architecture has explored the use of *n*-butylammonium bromide (*n*-BA) to form the potential barrier at the interface.^[166] The *n*-BA prepared devices, like those of Bai, highlight a double-edged sword in which current density and fill factor can be sacrificed to improve the photovoltage at an overall cost to the PCE. Nevertheless, the *n*-BA devices produced with a potential barrier can minimize voltage losses sufficiently to exceed 90% of the open circuit voltage limit in the Shockley-Queisser model, achieving an impressive V_{oc} of 1.31 V ($E_g \approx 1.72$ eV) (Figure 17b). Moreover, by decreasing the thickness of the inversely graded layer the authors highlight an optimal secondary cation process in which a thinner 2D perovskite barrier may be constructed to act as a buffer to mitigate back recombination while also allowing a high fraction of electrons to tunnel through the interface. Ultimately such approaches can offer improvements to the device PCE in the inverted architecture.

Jiang et al. further added to the discussion on the use of dripping PEAI solution as a perovskite treatment, identifying that the effects on device performance vary significantly with annealing temperature.^[167] In a key observation, the authors

reported that 2D perovskite phases were formed following annealing, with higher temperatures promoting the formation of the 2D PEA₂PbI₄ phase. Consequently, the role of the large organic cation treatment is highly dependent on the annealing conditions. In addition to temperature, recent works have also highlighted the link between concentration and formed 2D phases.^[162] In the absence of annealing, PEAI molecules act to passivate iodine vacancies on the surface (Figure 17c), reducing trapping and improving device performance affording a champion device with parameters V_{oc} (1.16 V), J_{sc} (24.9 mA cm⁻²), FF (81.4%), and an impressive PCE of 23.5% (Figure 17d). The ability of large alkylamine and ammonium salt molecules to passivate surface defects, in the absence of annealing, has since been identified in a number of further studies.^[155,169,170] Curiously, samples in which the films were annealed and formed a PEA₂PbI₄ secondary film exhibited a lower PCE of 20.5%, owing to reduced passivating interactions on the surface. Contrastingly, very recent work by Yoo et al. presented a device prepared using a 2D alkylammonium bromide passivation layer which was subsequently annealed at 100 °C. The dimensionally graded PSC achieved a remarkable certified PCE of 25.2%.^[171] This ambiguity has led to a number of key questions in producing dimensionally graded perovskite layers. In particular it is crucial that key factors such as annealing temperature, thickness and the band edge alignment are better understood to find a optimal processing procedure. It is our expectation that a synergistic approach to improving the interface is optimal, which both looks to reduce the number of trap states via molecular passivation while also promoting self-driven carrier separation at the interface.

As discussed, a number of studies have demonstrated that a 2D secondary perovskite layer can improve the perovskite absorber layer through engineering the band gap and passivation effects. Interestingly, a recent work by Jung et al, that wide band gap perovskite interlayers could also be used to open the door to new opportunities in CTL choice.^[168] In an unexpected result, the authors found the addition of a *n*-hexyl trimethyl ammonium bromide (HTABr) lower dimensional secondary perovskite layer transformed the charge transporting properties of poly(3-hexythiophene) P3HT (Figure 17e). Specifically, the addition of the HTABr perovskite phase promotes a preferential orientation of P3HT polymers significantly improving the typically poor mobility from 10^{-5} to 0.1 cm² V⁻¹. Furthermore, the HTABr layer acts synergistically to reduce recombination at the surface and yield longer photolifetimes, reducing losses in the V_{oc} . The devices prepared with a HTABr dramatically improved the performance of P3HT based cells, increasing the PCE from 15.8% to a highly impressive 23.3%, paving the way for further device engineering with P3HT (Figure 17f). Finding stable alternatives to spiro-OMeTAD has become a key challenge in perovskite architectural engineering, with materials such as carbon pastes recently gaining attention as previously discussed.^[172] In addition to the promising PCE recorded using P3HT, the unencapsulated devices exhibit excellent stability, retaining 80% initial efficiency over an excess of 1000 h in 85% humidity. The findings are an excellent example how varying the perovskite composition through the device can open new routes to innovating new architecture, in addition to enhancing more traditional architectures.

The use of perovskite:perovskite graded architectures has also emerged as a new hope into finding methods of improving

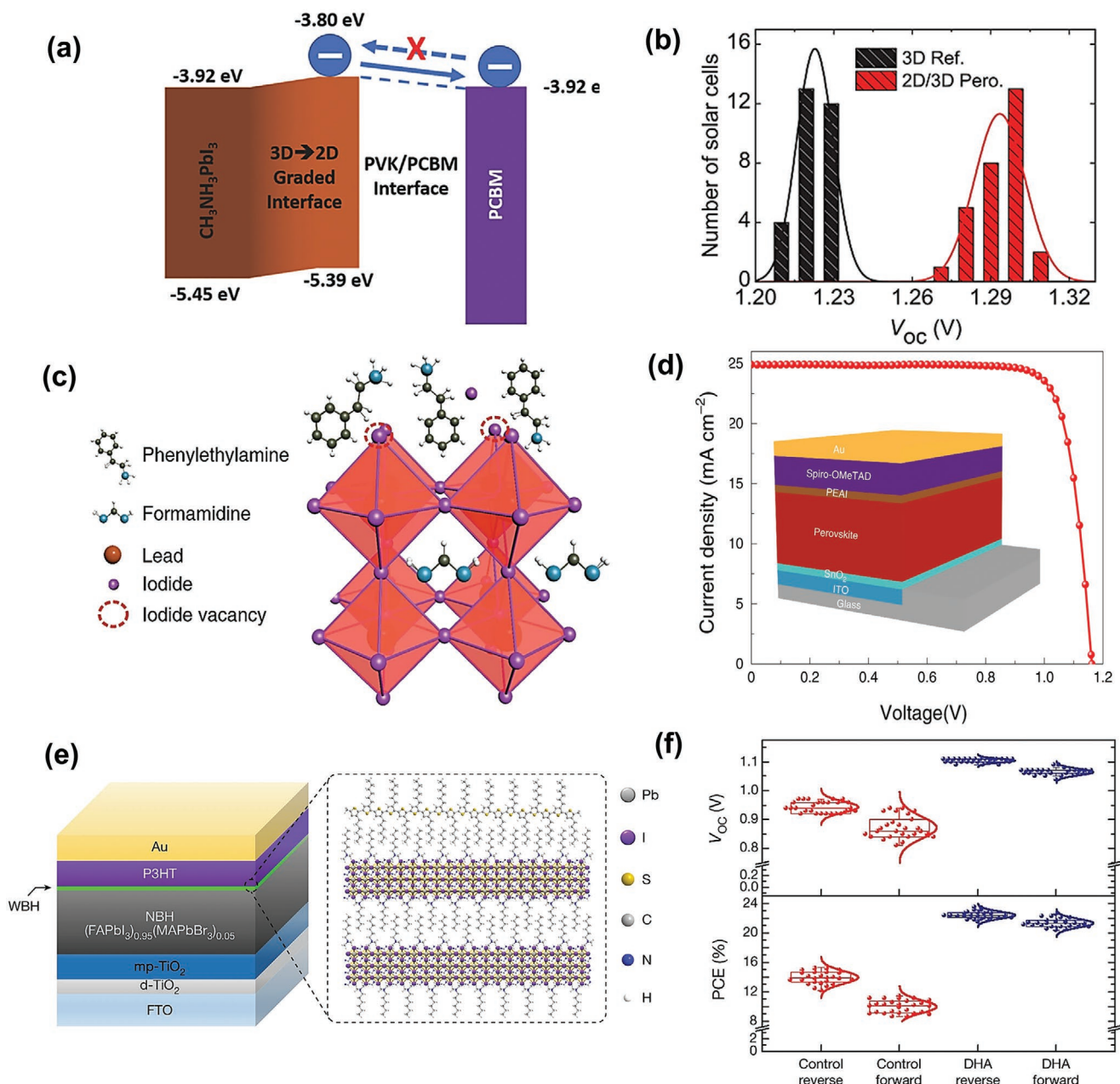


Figure 17. a) Schematic of band gap grading in the perovskite layer. Reproduced with permission.^[165] Copyright 2017, Wiley-VCH. b) V_{oc} statistics on 48 PSCs with and without *n*-BABr grading ($E_g = 1.72$ eV). Reproduced with permission.^[166] Copyright 2019, Wiley-VCH. c) Passivating interaction between PEAI molecules and point defects on the perovskite lattice. d) *J*-*V* curve of champion PSC using 20 nm PEAI without formation of a 2D layer (23.56%). Adapted with permission.^[167] Copyright 2019, Springer Nature. e) Device architecture of highly efficient P3HT-based graded PSCs. f) Device statics of 27 control and double-layered halide architecture (DHA) PSCs. Reproduced with permission.^[168] Copyright 2019, Springer Nature.

the PSC stability, a key challenge in perovskite optoelectronics. It has been well established that replacing a small organic cation in favor of a larger and more hydrophobic cation affords the perovskite greater tolerance to moisture mediated degradation through preventing the washing-out of soluble A-site cations.^[173,174] While the stability of the first reported lower dimensional films comprised entirely of purely lower dimensional perovskite absorber layers typically exceeds that of conventional 3D perovskite compositions, the efficiency is typically reduced

owing to a non-ideal band gap and poor overlap with the solar spectrum.^[175] Nevertheless, when used as an interfacial layer the hydrophobic GHJ can also form a moisture barrier, capable of protecting the base perovskite film comprised of more soluble cations better tolerance to ambient conditions, while synergistically improving performance (Figure 18a).

In addition to moisture tolerance, films prepared with benzylamine treatments have been shown to exhibit improvements in phase stability over extended periods in ambient conditions

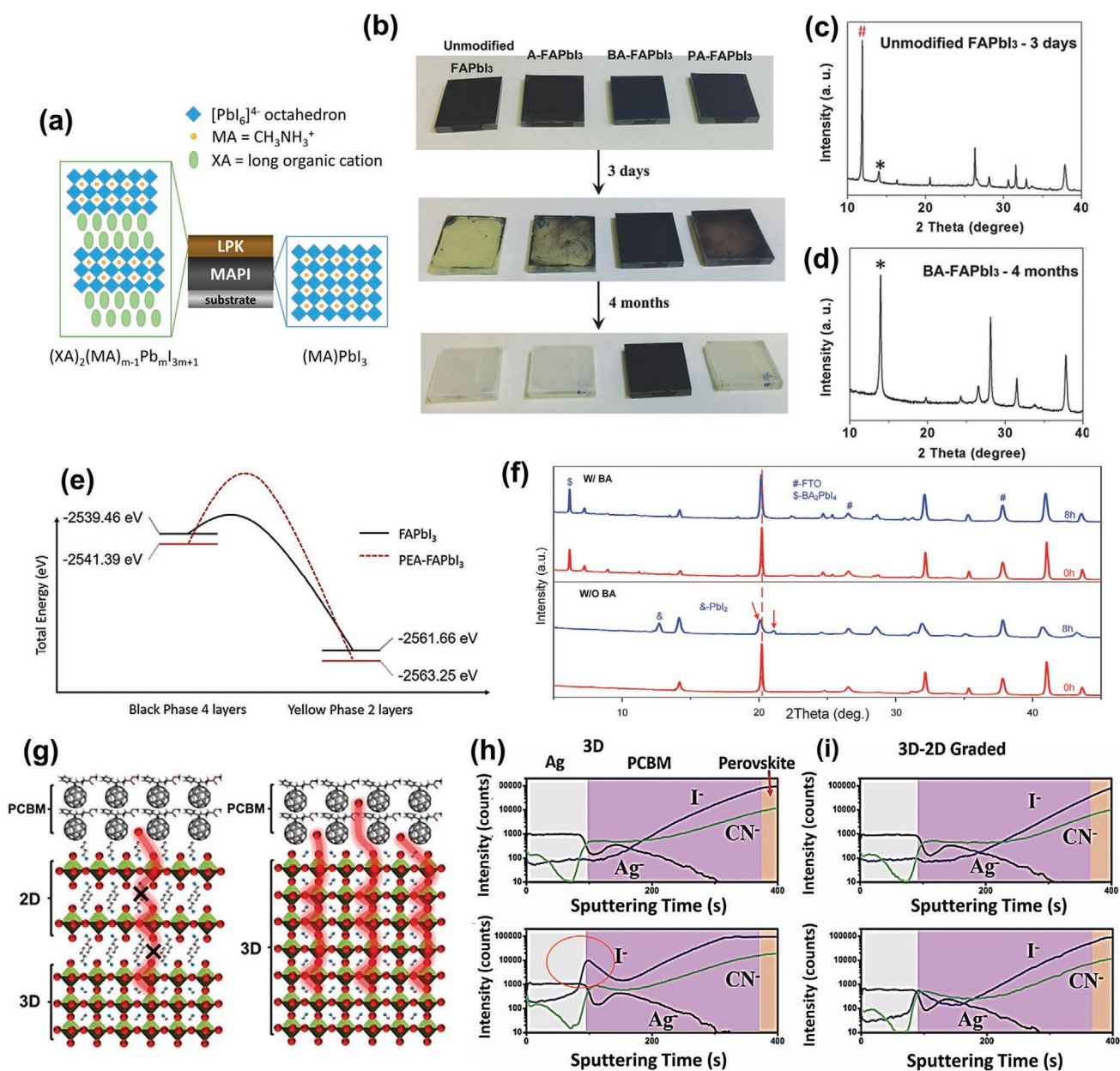


Figure 18. Effects of 2D GHJ on stability. a) Schematic of formation of 2D RP graded perovskite. Reproduced with permission.^[161] Copyright 2016, American Chemical Society. b) Images of FAPbI₃, A-FAPbI₃, BA-FAPbI₃, PA-FAPbI₃ after exposure to ambient conditions (50% RH) after 3 days and 4 months. c, d) XRD patterns of FAPbI₃ and BA treated FAPbI₃ following exposure to ambient conditions (50% RH). Reproduced with permission.^[163] Copyright 2016, Wiley-VCH. e) DFT thermodynamic analysis of the energies of δ -FAPbI₃ from black FAPbI₃. Reproduced with permission.^[176] Copyright 2016, Wiley-VCH. f) XRD patterns of Cs_{0.15}FA_{0.85}PbI_{2.19}Br_{0.81} with and without graded BA surface layer before and after aging with a 50 W white LED and heating at 85 °C for 8 h. Reproduced with permission.^[178] Copyright 2017, Wiley-VCH. g) Mechanism of iodine release suppression through the formation of a compact 2D layer. Reproduced with permission.^[179] Copyright 2018, American Chemical Society. i, j) ToF-SIMS of PSCs prepared with a graded 2D layer and without when fresh and after 80 °C heating for 12 h. Reproduced with permission.^[165] Copyright 2017, Wiley-VCH.

(Figure 18b). Key to the improved stability of the graded heterojunctions processed on formamidinium substrates is the reported ability of BA to effectively suppress the formation of the photoinactive and destructive yellow hexagonal δ -FAPbI₃ phase (Figure 18c,d).^[163,176] DFT calculations have since corroborated the result, suggesting that π - π stacking of the phenyl rings acts to lock the lattice unit and raise the energy barrier

to the degradation species formation (Figure 18e).^[176] Further details on the effect of a BA₂PbI₄ secondary perovskite layer on the device stability was offered by Zhou et al. who revealed films with a secondary BA perovskite layer exhibited significantly reduced phase separation in mixed halide perovskite films following thermal aging (Figure 18f). While not stated explicitly it is likely that similar locking of the lattice raises the energy

barrier to ion migration as previously reported in strained mixed halide systems.^[177] Upon imaging the perovskite surface following the same thermal degradation, the authors further note that the BA layer also prevents the opening of voids within the perovskite film which can catalyse the degradation through the formation of reactive point defects and releasing iodine out the perovskite layer.^[178]

Release of the halide constituents from perovskite thin films during degradation have been identified to encourage further degradation of the perovskite material while also reacting adversely with spiro-OMeTAD and metal contacts such as silver, forming silver iodide.^[180] Lin et al. investigated the effect of a 2D phase on the stability of the perovskite/spiro-OMeTAD interface. In a key observation the authors noted that formation of a MAPbI₃ film with *n*-BA (*n*-butylamine) formed a compact *n*-BA₂PbI₄ layer which can effectively block volatile MA⁺ and I₂ release from the perovskite (Figure 18g).^[179] Suppression of iodine release via a 2D interlayer has since been directly observed conducting ToF-SIMS on aged PEA treated MAPbI₃ films (Figure 18h,i).^[165] The application of a graded 2D layer has interesting implications on tackling perovskite device stability, tackling the origins of degradation both internal and external.

Ultimately, the breakthroughs in stability of 2D secondary growth perovskites combined with high hydrophobicity enabled Grancini et al. to produce 2D/3D GHJ perovskite solar cells which retained >100% efficiency over a period of 500 days.^[181] To improve the stability spiro-OMeTAD was replaced with a carbon slurry HTL. The printed graded 2D/3D films PSCs yielded a modest champion efficiency reaching 12.71% in a single cell and 11.2% when combined to form a 10 × 10 cm² module. To conduct the stability measurements, the PSCs were kept heated at 55 °C under 1 sun illumination for 24 h a day following sealing with glass in an ambient atmosphere to protect from mechanical stress on the device. The study highlights two highly encouraging breakthroughs, first, when combined with stable CTLs the production of PSCs with long shelf-lives required for commercialization is feasible using a stable 2D/3D GHJ perovskite film. Second, the use of printing techniques to fabricate the devices in the work is highly encouraging that GHJ device architectures are suitable for commercial high throughput and large area production using role to role methods.

In recent years, a wealth of studies have identified the formation of perovskite:perovskite GHJs as a highly promising direction for future PSC optimization and development. The diversity in the graded perovskite heterojunction has led to three sub-architectures evolving (Figure 14a). Amongst these architectures formation of layer-by-layer QD films (Figure 14a) represents a useful tool in creating highly controlled systems for probing the underlying physics of the architectures. Furthermore, the ability to prepare perovskite QDs as a stable ink enables opportunities in higher efficiency printed devices. Progressing from quantum dots, the spin coating of additional organic species to grow secondary perovskite phases has emerged as a simple low-cost architecture with profound implications on stability and efficiency. Amongst these secondary cations, the use of large hydrophobic organic cation has stood out as a clear forerunner PSCs with performance reaching 25.2%. It is becoming ever clearer that the use of

graded 2D–3D perovskite active layers is key to producing the highest efficiency devices. However, ambiguities within the use of the architecture remain. First, it is important to better understand the mechanics of charge extraction through the 2D layer such that the observed improvements to efficiency in both regular and inverted architectures can be rationalized. To do this a better understanding of the tendency of the perovskite: perovskite to form a type I or II heterojunction must be better understood. Second, the formation of quasi 2D/3D phases raises the question whether the graded region itself is subject to grading through the *n* value (width of the quantum well) as observed frequently in pure RP perovskite phases.^[182–184] Finally It is also notable that while the devices discussed display a clear improvement on the controls presented, great care should be taken when comparing to a control with a different composition, in particular the absence of Cs⁺ cations. Future investigative studies into the importance of band gap grading should look to prepare controls with as close as possible composition to the final modified device to isolate the significance of the grading effect, rather than the compositional change.

4. Characterization Methods of Novel Architectures

As with any emerging technology identifying useful measurement techniques to understand the underlying mechanisms is essential. Universal to all the previously discussed architectures, the need for detailed and accurate characterization is of high importance to answer key questions such as the extent to which the grading depth of a graded structure affects overall performance. We therefore present a collection of useful characterization techniques which are suitable for understanding first the composition variation and electrical properties of BHJ and GHJ PSCs. Such characterization may be used universally between architectures.

While well-established measurements such as SEM, XRD have a key role to play in the characterization of these structures, changes to the architecture within the perovskite layer rather than at an interface have presented a challenge that must be overcome, namely developing minimally invasive methods of probing the bulk. In addition, exposing the perovskite using etching techniques such as sputtering can change the chemical environment influencing parameters such as the valance band edges. In this section, we discuss methods useful for characterizing the compositions and electronic properties of the perovskites in these novel architectures. In particular, we highlight the importance of measuring the properties of a perovskite film by minimizing the impact of beam damage, and reducing where possible changes to the local chemical environment during measurement.

4.1. Composition Characterization

Characterizing the chemical composition as a function of depth within the perovskite films is crucial in understanding the material properties of bulk and graded perovskite heterojunctions. Depth resolved ToF-SIMS (Figure 19a) has become a popular method of characterizing the distribution of the additives

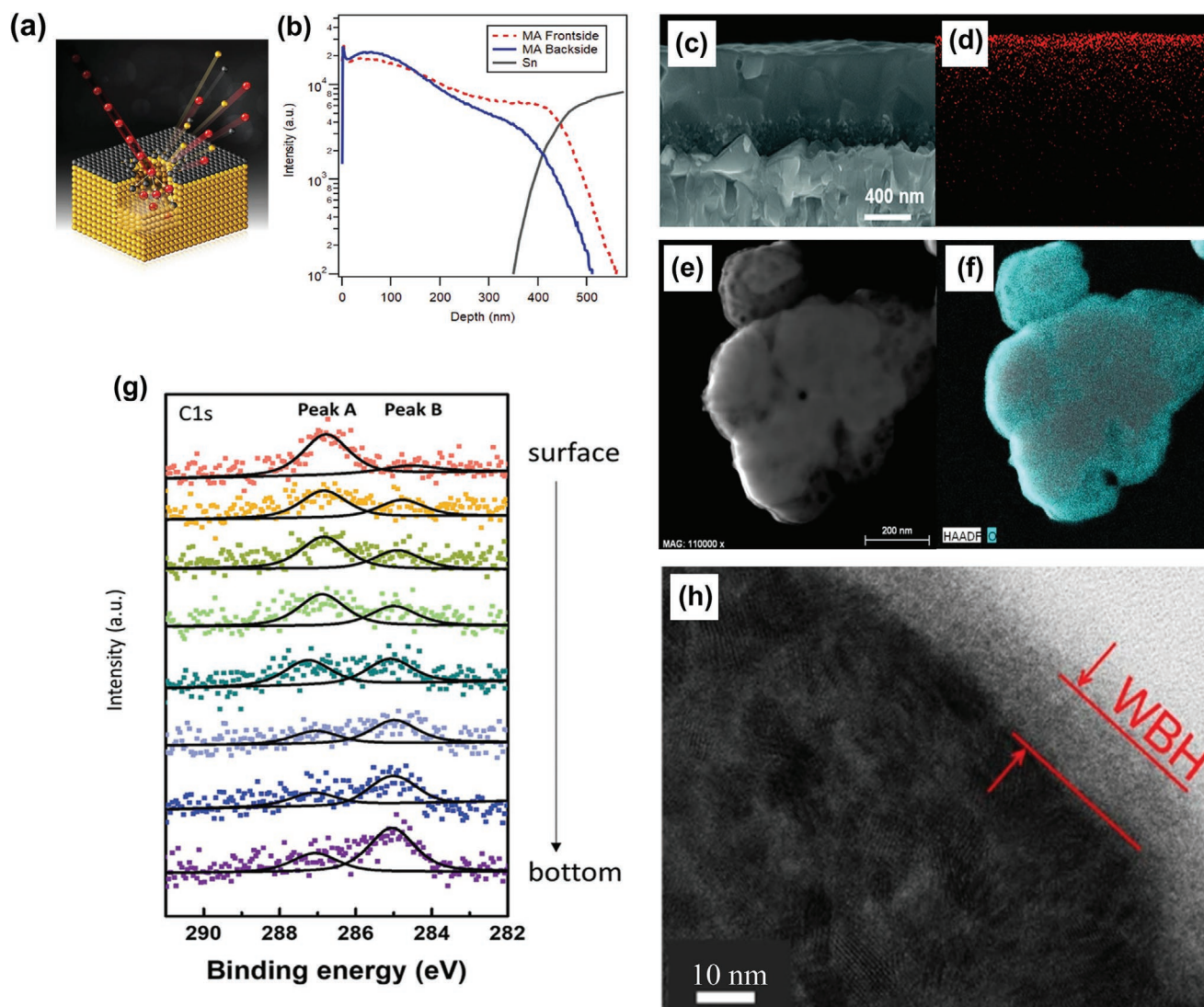


Figure 19. a) Representation of TOF-SIMS probing the sample composition (yellow) via impact with a high-energy primary-ion beam (red). Primary-ion beam damaged leads to mixing of atomic layers and leads to potential artifacts (arrows). b) TOF-SIMS beam damage based artifacts of delaminated methylammonium perovskites film measured from both sides. Reproduced with permission.^[186] Copyright 2019, American Chemical Society. c) Cross section SEM image of GABr graded perovskite heterojunction, d) EDX image of Br grading across a FABr graded heterojunction. Reproduced with permission.^[152] Copyright 2017, Royal Society of Chemistry. e) HAADF-STEM image of perovskite: α -bis-PCBM GHJ grain. f) Oxygen map indicating PCBM location on a perovskite: α -bis-PCBM GHJ grain via STEM coupled EDX measurement. Reproduced with permission.^[78] Copyright 2017, Wiley-VCH. g) XPS depth profiles of a perovskite film on PCBM film peak B is represents PCBM identified via a reference sample.^[187] h) HRTEM image of thin wide band gap perovskite interlayer.^[168] Copyright 2019, Springer Nature.

and perovskite cations within the perovskite bulk.^[110,185,186] It is critical however, before making conclusions on the composition profile of a film that consideration has been made for the presence of beam damage from the sputter process. The effects of sputtering on the composition profile was recently highlighted by Harvey et al. who observed gradient like profiles in organic cation as an artifact of beam damage (Figure 19b).^[186] To this extent extra care should be taken to confirm films are truly exhibiting graded behavior and are not exhibiting such beam damage. This can be ensured via reducing sampling rates where possible to ensure primary ion damage is cleared or using a gas cluster ion beam (GCIB) sputter. 3D tomography is a useful additional tool that can be coupled in parallel with the ToF-SIMS measurement offering lateral resolution and can

assist convincingly demonstrating the distribution of an additive via improved visualization.

Cross-sectional Energy Dispersive X-ray Spectroscopy (EDX/EDS) mapping is an alternative characterization technique that has been used to aid confirmation of graded profiles.^[112,127,152] When coupled to a scanning electron microscope and in the absence of charging effects, a composition map can be constructed through spatially mapping elements across a surface. This approach is particularly powerful in cases where a signature element can be tracked and used as a marker, for instance tracking fluorine signals following coating of fluorinated CTL within a perovskite film or a unique halide in a cation solution for secondary growth perovskite layers (Figure 19c,d).^[106,152] For higher resolution measurements, EDX techniques can be

further combined with STEM enabling compositional analysis on the nanoscale. Such measurements are highly useful in forming convincing visualization of the diffusion of additive within a perovskite film largely avoiding any inaccuracies associated with beam damage from sputter-based techniques. Additionally, the use of EDX coupled with STEM has been recently used to offer evidence for the formation of conductive CTL networks in BHJs through tracking the oxygen signal associated with PCBM (Figure 19e,f). Tracking oxygen is frequently used as a marker for PCBM, however sufficient care must be taken to avoid exposure to atmospheric oxygen which rapidly adsorbs to the film affecting the measurement interpretation. This can be removed via degassing under vacuum or through the heating of samples.

X-ray photoelectron spectroscopy (XPS) depth profiling is another option for confirming the results of ToF-SIMS profiles. In addition to tracking the composition of chosen heteroatoms through their relative integrated peak intensities, XPS combined with etching offers additional information, probing relative shifts of the binding energy of key orbitals, such as the Pb^{2+} 4f orbital, as a function of depth. This may be particularly useful in understanding the deep passivating interactions within the bulk of the active layer and the origin of band gap grading. This method was also effectively used by Zai et al. who replaced etching with minimally destructive angle-resolved XPS (AR-XPS) to probe the ratio of Br/I within a shallow depth in a locally graded perovskite:CsPbBr₃ QD perovskite film.^[143] The biggest drawback of XPS however comes from the significantly reduced sensitivity compared to ToF-SIMS measurement. However, work by Zhong et al. recently effectively demonstrated the technique using a GCIB sputter to track PCBM through a perovskite film comparing the C1s orbital enabling further insights such as passivation effects within the film (Figure 19g).^[187]

Identification of potentially ultra-thin layers of secondary growth thin perovskite layers poses a key challenge to understanding the latter architectures discussed. This difficulty has directly led to the ambiguity as to the extent of *n* value grading of RP phases when used as a post fabrication treatment. In such situations grazing-incidence wide angle X-ray scattering (GIWAXS) combined with Grazing-incidence X-ray diffraction (GIXRD) are useful techniques for understanding how the crystal phase changes through the active layer. Through adjustments of the incident x-ray source angle, the depth of diffraction within the film can be controlled to enable a depth resolution enabling crystallographic characterization of ultrathin perovskite phases.^[168,188] It is useful to note that the depth of such measurements is highly dependent on perovskite composition and does not necessarily vary linearly with omega.^[188] Alternatively, high resolution transmission electron microscopy can be used to image the formation of 2D perovskite layer offering accurate insights into the thickness which cannot be readily achieved using simple profilometry (Figure 19h).^[168]

4.2. Band Edge and Carrier Extraction Characterization

To effectively engineer band gap grading within the perovskite layer, it is imperative that effective methods are available

to understand the band edge energies and carrier dynamics through the film. The challenge of conducting such measurements has often left studies lacking the clear data required to make convincing arguments on the behavior of carriers within the architecture. To this extent cross-sectional KPFM has been widely used as a useful method for elucidating the band profiling and consequent electric fields through measuring the contact potential between the work functions of a known tip and a perovskite film. A range of methods have been reported for ensuring precise cleaving through the device such as tension breaking,^[189] focused ion beam (FIB) cleaving^[190] and additional FIB polishing to ensure a smooth cross section.^[156] The use of focused ion beam milling to polish the sample is preferable to mechanical strain based cleaving methods due to the improved smoothness of the cross section. Such methods also enable retention of device functionality without the implantation of Ga⁺ impurities as demonstrated by Bergmann et al.^[191]

In addition to KPFM, EBIC is an effective method to characterize and identify the presence space charge regions within perovskite films. The use of EBIC within the literature has yet to reach its full potential and offers useful opportunities in the identification of CTL network formation in perovskite:CTL BHJs. The presence of such networks could also be complemented using high-resolution transmission electron microscopy (HRTEM) across device cross-sections combined with electron energy loss spectroscopy (EELS), offering an alternative to STEM-EDX for high resolution element mapping between grain boundaries.^[36]

EBIC is also required in nanostructured bulk heterojunctions to further substantiate the claims of increased carrier separation across an extended heterojunction within the bulk. The benefits of the increased heterojunction will likely depend heavily on the formation and passivation of an increased number of surface states. Nevertheless, through conducting EBIC maps of the cross section it may be possible to compare the carrier extraction efficiency between nanostructured and planar interfaces. While both time resolved and steady state PL have featured heavily in the arguments for enhanced carrier separation the results are highly sensitive to factors such as changes in thickness, absorption coefficient, pump fluence, and trapping and more definitive supplementary characterization is further required. Such techniques include ultra-fast optical spectroscopies such as TAS, capable of probing both the magnitude and timescale of hole transfer at an interface via tracking polaron transient signals.^[192]

Understanding the behavior of the band energies through the perovskite can also be achieved using minimally invasive methods utilizing angle-resolved measurements. Angle resolved hard x-ray photoelectron Spectroscopy (AR-HAXPES) offers an alternative approach to surface based photoelectron spectroscopy enabling non-invasive probing of the valence band energy of the bulk perovskite as a function of depth. This technique was recently used by Kanda et al. who probed the band edge energies up to 40 nm within the perovskite bulk. However, the high energy of the hard X-ray photons (4000 eV) necessitates access to a synchrotron X-ray source, significantly increasing the cost and time of measurements.^[193] Alternatively AR-XPS can offer similar insights into the band energies albeit at reduced resolution around the valence minimum. Nevertheless, previous studies have reported valence band energies using XPS characterization.^[161,194,195]

5. Perspective and Outlook

All four of the discussed emerging device architectures have undergone impressive transformations in PCE since first being reported. Amongst these, layered 2D and quasi-2D graded heterojunctions stand out as particularly promising improving in PCE from 16.0% to 25.2% over a 4-year period. Complimenting the remarkable rise in PCEs, the architectures also offer new opportunities in tackling stability, which has enabled the printed fabrication of PSC modules with a shelf life exceeding a year in ambient conditions.^[181] We therefore expect both the PCE and stability of the 2D and quasi 2D GHJs to continue their ever-increasing trajectory. Furthermore, the lower dimensional graded heterojunctions present a promising candidate to become a highly stable, efficient, and scalable complete commercial technology. Despite exhibiting lower PCEs than the other discussed approaches, nanostructured perovskite interfaces have opened a new approach into engineering the interaction between the perovskite absorber and light utilizing photonic structures. The photonic architecture approaches appear particularly promising in the field of all inorganic perovskite photovoltaics, with BHJ architectures producing amongst the highest reported J_{sc} and PCE values. This is particularly interesting in the use of fully inorganic perovskites, where key device performance parameters such as current can be significantly improved through advanced light management and efficient carrier separation. This may in future help produce stable inorganic perovskites with a wide band gap suitable for tandem applications.

Alternatively, the addition of CTLs into the perovskite to form either a GHJ or BHJ imparts key benefits to the film particularly through enhanced passivation and stability. However, many key questions remain over the architectures such as: to what extent can conductive CTL networks form within a perovskite film and how localized do CTL grading effects occur within the perovskite film.

Both questions can be addressed through expanding the range of characterization techniques beyond time-resolved and steady state PL, which alone are often insufficient evidence for the discussed points. More convincing arguments can be structured around direct measurements of phenomena such as probing electron transfer through a graded film through transient pump-probe techniques. Finding minimally invasive methods of measuring the band edge energies through the films has presented a key challenge to many of the discussed structures. A shift in approach towards angle-resolved measurements are encouraged for gaining insights how material properties change within the active region as a function of depth without changing the chemical environment of the bulk perovskite.

The recently emerging architectures may also present opportunities in the design of third generation photovoltaics which look to surpass the S-Q limit. Intraband cooling of high energy vibrationally excited states following excitation with high-energy photons is a key loss mechanism across all conventional photovoltaics. However, recent studies have suggested that rapid transfer of electrons between perovskite and fullerene interlayers, combined with unusually slow hot carrier cooling, may enable extraction of high energy vibrationally excited elec-

trons on timescales faster than intraband relaxation to the band edges.^[87,196] The formation of photonic structures such as IO infiltrated by fullerenes could enable ultra-thin perovskite thin films capable of efficiently capturing high fractions of light via the slow photon and scattering effects while also enabling ultra-fast carrier separation and short diffusion to metal contacts.^[87] We therefore expect that future innovations in the device architecture may present new opportunities to achieving efficiencies beyond the Shockley–Queisser limit.

Alternatively, the S-Q limit can be overcome through fabrication of multi-junction tandem photovoltaic devices. The merits and key challenges of such devices have recently been discussed in detail in previous publications.^[3] In the work the importance of light management to reduce optical losses was highlighted as a significant factor in the further improving of tandem architectures. In particular, the need for texturing to improve the collection of long wavelength photons was emphasised as important for improving the tandem solar cell (TSC) overall performance. This is perhaps of greatest significance in all-perovskite tandem solar cells which typically comprise a wide band gap lead based film and a narrower lead/tin binary perovskite. The reduced absorption of the lead/tin conventionally requires a thick top cell perovskite to capture a sufficient fraction of the light for effective current-matching between cells. However, such requirements for the tin-based layer thickness ($>1 \mu\text{m}$) make the cell susceptible to losses from the high concentration of trap states associated with tin perovskites.^[197,198] Effective light management from the use of a nanostructured bulk heterojunction may offer an effective solution enabling a thinner lead/tin layer reducing recombination and trapping losses within the top cell. In addition to reducing the optical losses, increasing the $V_{oc,deficit}$ of the wide band gap sub-cell is of paramount importance for achieving high overall device voltages in TSCs. As discussed, losses in the photovoltage can be reduced by incorporating a graded perovskite carrier directing back surface field resembling architecture in the sub-cell boosting the overall stack performance. As such the discussed architectures represent promising solutions to some of the key design criteria previously stipulated in the literature for high performance TSCs.

While great strides have recently been made in transforming both multi-junction and single-junction PSCs into a commercially viable technology through engineering the device architecture, further research is required both experimentally and theoretically. In recent years PSCs have started to take tentative steps towards new architectures with advanced photonic, carrier extraction and band gap grading properties. The evolution of the architecture can be likened to that of the mature technologies such as Si, CIGs, CZTSe, and InGaAs, which have undergone similar evolutions yielding higher PCEs. However, we note fundamental differences exist in the approach to developing the architecture of the perovskite compared to the pre-existing technologies. In the optimization of inorganic thin film technologies such as Si, extensive modeling of the interaction between the absorber and light has guided design. Contrastingly the development of PSCs has proceeded with a larger emphasis on experimental optimization. A recent example of this difference in approach between the perovskite evolution and previous technologies is the recent report of perovskite p-n homojunctions PSCs.^[189] Following the experimental reporting

of the p-n homojunction structure, subsequent modeling of the structure revealed that the intrinsic carrier densities of the p- and n- type layer were orders of magnitude lower than required to achieve the desired homojunction within the perovskite active region.^[199] It is therefore important that modeling and experimental optimization work together with simulation work guiding design.

While the formation of BHJs and GHJs as discussed in this review are highly promising candidates for reducing losses in the perovskite film and look set to lead the way in PSC performance, the limited number of theoretical studies compared to previous technologies presents a challenge in finding optimal device structures. One reason for this discrepancy is the difficulties associated with modeling the perovskite system itself, with the formation of non-stoichiometric materials posing a challenge in creating model representations of the structure. Additionally, implementing theoretically optimized structures experimentally necessitates a high level of control over the perovskite growth, which is often not possible.

Over the last decade the use of a high throughput approach to optimizing the architecture has been remarkably effective method of achieving rapid gains in PCE in a short amount of time. However, as PSCs look to ever more sophisticated architectures, it becomes increasingly important that design is aided by an improved understanding of the characteristics of device architectures through modeling and characterization. It is also important to remain true to the key advantages of the perovskite material, low cost, simple fabrication, and large area processability, these key factors should be kept in mind as the perovskite device architecture continues its evolution to higher efficiency and more stable devices. In looking to the future, we note the tentative steps being made in defect engineering as a method of doping the perovskite an approach that looks set to further revolutionize the device architecture in the next half decade. Such intentional doping could enable greater control over the positioning of the depletion region within the device further improving carrier generation, extraction and thereby photovoltage. It is also expected that the rapid pace of development of all perovskite tandems combined with the high defect concentration in tin perovskite will encourage further work in photonic structures and light management in a similar manner to silicon technologies. It is evident from this work that innovating and optimizing the device architecture continues to play a key role in addressing stability and improving PCE of perovskite solar cells over a decade on from their first discovery.

Acknowledgements

T.W. acknowledges financial support provided by the doctoral college studentship (DCSA3) at the University of Surrey. W.Z. is pleased to acknowledge financial support from EPSRC New Investigator Award (2018; EP/R043272/1) and H2020-EU grant (2018; CORNET 760949). S.J.S. gratefully acknowledges the support of EPSRC (UK) under grant number EP/N021037/1.

Conflict of Interest

The authors declare no conflict of interest.

Keywords

architecture engineering, bulk heterojunction, graded heterojunction, perovskite, quasi 2D/3D

Received: March 31, 2021

Revised: May 19, 2021

Published online: June 23, 2021

- [1] Z. Li, T. R. Klein, D. H. Kim, M. Yang, J. J. Berry, M. F. A. M. van Hest, K. Zhu, *Nat. Rev. Mater.* **2018**, *3*, 18017.
- [2] M. Cai, Y. Wu, H. Chen, X. Yang, Y. Qiang, L. Han, *Adv. Sci.* **2017**, *4*, 1600269.
- [3] H. Li, W. Zhang, *Chem. Rev.* **2020**, *120*, 9835.
- [4] M. R. Filip, G. E. Eperon, H. J. Snaith, F. Giustino, *Nat. Commun.* **2014**, *5*, 5757.
- [5] M. M. Lee, J. Teuscher, T. Miyasaka, T. N. Murakami, H. J. Snaith, *Science* **2012**, *338*, 643 LP.
- [6] A. Kojima, K. Teshima, Y. Shirai, T. Miyasaka, *J. Am. Chem. Soc.* **2009**, *131*, 6050.
- [7] J.-H. Im, C.-R. Lee, J.-W. Lee, S.-W. Park, N.-G. Park, *Nanoscale* **2011**, *3*, 4088.
- [8] U. Bach, D. Lupo, P. Comte, J. E. Moser, F. Weissörtel, J. Salbeck, H. Spreitzer, M. Grätzel, *Nature* **1998**, *395*, 583.
- [9] J. Burschka, A. Dualeh, F. Kessler, E. Baranoff, N.-L. Cevey-Ha, C. Yi, M. K. Nazeeruddin, M. Grätzel, *J. Am. Chem. Soc.* **2011**, *133*, 18042.
- [10] H.-S. Kim, C.-R. Lee, J.-H. Im, K.-B. Lee, T. Moehl, A. Marchioro, S.-J. Moon, R. Humphry-Baker, J.-H. Yum, J. E. Moser, M. Grätzel, N.-G. Park, *Sci. Rep.* **2012**, *2*, 591.
- [11] J. M. Ball, M. M. Lee, A. Hey, H. J. Snaith, *Energy Environ. Sci.* **2013**, *6*, 1739.
- [12] J. Burschka, N. Pellet, S.-J. Moon, R. Humphry-Baker, P. Gao, M. K. Nazeeruddin, M. Grätzel, *Nature* **2013**, *499*, 316.
- [13] M. Liu, M. B. Johnston, H. J. Snaith, *Nature* **2013**, *501*, 395.
- [14] J.-Y. Jeng, Y.-F. Chiang, M.-H. Lee, S.-R. Peng, T.-F. Guo, P. Chen, T.-C. Wen, *Adv. Mater.* **2013**, *25*, 3727.
- [15] Y. Shao, Z. Xiao, C. Bi, Y. Yuan, J. Huang, *Nat. Commun.* **2014**, *5*, 5784.
- [16] Z. Xiao, C. Bi, Y. Shao, Q. Dong, Q. Wang, Y. Yuan, C. Wang, Y. Gao, J. Huang, *Energy Environ. Sci.* **2014**, *7*, 2619.
- [17] M. Yavari, X. Liu, T. Webb, K. D. G. I. Jayawardena, Y. Xiang, S. Kern, S. Hinder, T. J. Macdonald, S. R. P. Silva, S. J. Sweeney, W. Zhang, *J. Mater. Chem. C* **2021**, *9*, 4367.
- [18] D. Yang, R. Yang, K. Wang, C. Wu, X. Zhu, J. Feng, X. Ren, G. Fang, S. Priya, S. (Frank) Liu, *Nat. Commun.* **2018**, *9*, 3239.
- [19] B. Li, Y. Xiang, K. D. G. I. Jayawardena, D. Luo, J. F. Watts, S. Hinder, H. Li, V. Ferguson, H. Luo, R. Zhu, S. R. P. Silva, W. Zhang, *Sol. RRL* **2020**, *4*, 2000060.
- [20] H. Kim, K.-G. Lim, T.-W. Lee, *Energy Environ. Sci.* **2016**, *9*, 12.
- [21] M. Yavari, M. Mazloum-Ardakani, S. Gholipour, M. M. Tavakoli, N. Taghavinia, A. Hagfeldt, W. Tress, *ACS Omega* **2018**, *3*, 5038.
- [22] P. Zhu, S. Gu, X. Luo, Y. Gao, S. Li, J. Zhu, H. Tan, *Adv. Energy Mater.* **2020**, *10*, 1903083.
- [23] Q. Zhao, R. Wu, Z. Zhang, J. Xiong, Z. He, B. Fan, Z. Dai, B. Yang, X. Xue, P. Cai, S. Zhan, X. Zhang, J. Zhang, *Org. Electron.* **2019**, *71*, 106.
- [24] M. Kim, I. Choi, S. J. Choi, J. W. Song, S.-I. Mo, J.-H. An, Y. Jo, S. Ahn, S. K. Ahn, G.-H. Kim, D. S. Kim, *Joule* **2021**, *5*, 659.
- [25] F. Giordano, A. Abate, J. P. Correa Baena, M. Saliba, T. Matsui, S. H. Im, S. M. Zakeeruddin, M. K. Nazeeruddin, A. Hagfeldt, M. Graetzel, *Nat. Commun.* **2016**, *7*, 10379.
- [26] V. Ferguson, B. Li, M. O. Tas, T. Webb, M. T. Sajjad, S. A. J. Thomson, Z. Wu, Y. Shen, G. Shao, J. V. Anguita, S. R. P. Silva, W. Zhang, *Adv. Mater. Interfaces* **2020**, *7*, 2001121.

- [27] T. J. Macdonald, M. Batmunkh, C.-T. Lin, J. Kim, D. D. Tune, F. Ambroz, X. Li, S. Xu, C. Sol, I. Papakonstantinou, M. A. McLachlan, I. P. Parkin, J. G. Shapter, J. R. Durrant, *Small Methods* **2019**, *3*, 1900164.
- [28] F. Shahvaranfard, M. Altomare, Y. Hou, S. Hejazi, W. Meng, B. Osuagwu, N. Li, C. J. Brabec, P. Schmuki, *Adv. Funct. Mater.* **2020**, *30*, 1909738.
- [29] K.-J. Yang, D.-H. Son, S.-J. Sung, J.-H. Sim, Y.-I. Kim, S.-N. Park, D.-H. Jeon, J. Kim, D.-K. Hwang, C.-W. Jeon, D. Nam, H. Cheong, J.-K. Kang, D.-H. Kim, *J. Mater. Chem. A* **2016**, *4*, 10151.
- [30] A. Morales-Acevedo, *Sol. Energy Mater. Sol. Cells* **2009**, *93*, 41.
- [31] Y.-T. Yen, Y.-K. Lin, S.-H. Chang, H.-F. Hong, H.-Y. Tuan, Y.-L. Chueh, *Nanoscale Res. Lett.* **2013**, *8*, 329.
- [32] G. Yu, J. Gao, J. C. Hummelen, F. Wudl, A. J. Heeger, *Science* **1995**, *270*, 1789.
- [33] A. K. Rath, M. Bernechea, L. Martinez, F. P. G. de Arquer, J. Osmond, G. Konstantatos, *Nat. Photonics* **2012**, *6*, 529.
- [34] F. Tan, S. Qu, W. Zhang, Z. Wang, *Nanoscale Res. Lett.* **2014**, *9*, 593.
- [35] D. A. R. Barkhouse, R. Debnath, I. J. Kramer, D. Zhitomirsky, A. G. Pattantyus-Abraham, L. Levina, L. Etgar, M. Grätzel, E. H. Sargent, *Adv. Mater.* **2011**, *23*, 3134.
- [36] B. Yang, O. Dyck, J. Poplawsky, J. Keum, A. Puzetzy, S. Das, I. Ivanov, C. Rouleau, G. Duscher, D. Geohagan, K. Xiao, *J. Am. Chem. Soc.* **2015**, *137*, 9210.
- [37] M. Jeong, I. W. Choi, E. M. Go, Y. Cho, M. Kim, B. Lee, S. Jeong, Y. Jo, H. W. Choi, J. Lee, J.-H. Bae, S. K. Kwak, D. S. Kim, C. Yang, *Science* **2020**, *369*, 1615.
- [38] J.-H. Im, J. Luo, M. Franckevičius, N. Pellet, P. Gao, T. Moehl, S. M. Zakeeruddin, M. K. Nazeeruddin, M. Grätzel, N.-G. Park, *Nano Lett.* **2015**, *15*, 2120.
- [39] R. Singh, S. R. Suranagi, S. J. Yang, K. Cho, *Nano Energy* **2018**, *51*, 192.
- [40] C.-Y. Chang, B.-C. Tsai, M.-Z. Lin, Y.-C. Huang, C.-S. Tsao, *J. Mater. Chem. A* **2017**, *5*, 22824.
- [41] W. Q. Wu, D. Chen, F. Li, A. R. Pascoe, Y. B. Cheng, R. A. Caruso, *Nano Energy* **2017**, *32*, 187.
- [42] Y. Yu, L. Lei, S. Yang, J. Xie, J. Shao, Q. Cao, S. Zhang, X. Ni, B. Ye, Y. Liu, *ACS Appl. Mater. Interfaces* **2017**, *9*, 23624.
- [43] H. Xiong, G. DeLuca, Y. Rui, Y. Li, E. Reichmanis, Q. Zhang, H. Wang, *Sol. Energy Mater. Sol. Cells* **2017**, *166*, 167.
- [44] A. A. Petrov, N. Pellet, J.-Y. Seo, N. A. Belich, D. Y. Kovalev, A. V. Shevelkov, E. A. Goodilin, S. M. Zakeeruddin, A. B. Tarasov, M. Graetzel, *Chem. Mater.* **2017**, *29*, 587.
- [45] Y.-A. Lu, T.-H. Chang, S.-H. Wu, C.-C. Liu, K.-W. Lai, Y.-C. Chang, Y.-C. Chang, H.-C. Lu, C.-W. Chu, K.-C. Ho, *Nano Energy* **2019**, *58*, 138.
- [46] W. Wu, D. Chen, F. Li, E. Al, *Nano Energy* **2017**, *32*, 187.
- [47] C. J. Pereyra, Y. Di Iorio, M. Berruet, M. Vazquez, R. E. Marotti, *Phys. Chem. Chem. Phys.* **2019**, *21*, 20360.
- [48] J.-F. Liao, W.-Q. Wu, Y. Jiang, D.-B. Kuang, L. Wang, *Sol. RRL* **2019**, *3*, 1800268.
- [49] J. M. Ball, S. D. Stranks, M. T. Hörantner, S. Hüttner, W. Zhang, E. J. W. Crossland, I. Ramirez, M. Riede, M. B. Johnston, R. H. Friend, H. J. Snaith, *Energy Environ. Sci.* **2015**, *8*, 602.
- [50] M. Kim, S. Jang, J. Choi, S. M. Kang, M. Choi, *Nano-Micro Lett.* **2019**, *11*, 53.
- [51] K. Meng, S. Gao, L. Wu, G. Wang, X. Liu, G. Chen, Z. Liu, G. Chen, *Nano Lett.* **2016**, *16*, 4166.
- [52] S. M. Kang, S. Jang, J.-K. Lee, J. Yoon, D.-E. Yoo, J.-W. Lee, M. Choi, N.-G. Park, *Small* **2016**, *12*, 2443.
- [53] S. Zhou, R. Tang, H. Li, L. Fu, B. Li, L. Yin, *J. Power Sources* **2019**, *439*, 227065.
- [54] B. R. C. Vale, E. Socie, A. Burgos-Caminal, J. Bettini, M. A. Schiavon, J.-E. Moser, *J. Phys. Chem. Lett.* **2020**, *11*, 387.
- [55] G. Tong, L. K. Ono, Y. Qi, *Energy Technol.* **2020**, *8*, 1900961.
- [56] M. Baranowski, P. Plochocka, *Adv. Energy Mater.* **2020**, *10*, 1903659.
- [57] M. Curti, J. Schneider, D. W. Bahnemann, C. B. Mendive, *J. Phys. Chem. Lett.* **2015**, *6*, 3903.
- [58] S. Zhou, R. Tang, L. Yin, *Adv. Mater.* **2017**, *29*, 1703682.
- [59] Y. Wang, M. Li, X. Zhou, P. Li, X. Hu, Y. Song, *Nano Energy* **2018**, *51*, 556.
- [60] T. K. Das, P. Ilaiyaraja, C. Sudakar, *Sci. Rep.* **2018**, *8*, 9709.
- [61] P. Ilaiyaraja, T. K. Das, P. S. V Mocherla, C. Sudakar, *J. Phys. Chem. C* **2019**, *123*, 1579.
- [62] Q. Zhang, R. Su, X. Liu, J. Xing, T. C. Sum, Q. Xiong, *Adv. Funct. Mater.* **2016**, *26*, 6238.
- [63] Y. Wang, P. Wang, X. Zhou, C. Li, H. Li, X. Hu, F. Li, X. Liu, M. Li, Y. Song, *Adv. Energy Mater.* **2018**, *8*, 1702960.
- [64] H. Zhang, J. Fan, J. Zhang, *Opt. Quantum Electron.* **2020**, *52*, 195.
- [65] R. Schmager, I. M. Hossain, F. Schackmar, B. S. Richards, G. Gomard, U. W. Paetzold, *Sol. Energy Mater. Sol. Cells* **2019**, *201*, 110080.
- [66] E. C. Garnett, B. Ehrler, A. Polman, E. Alarcon-Llado, *ACS Photonics* **2020**, *8*, 61.
- [67] N. Marinova, W. Tress, R. Humphry-Baker, M. I. Dar, V. Bojinov, S. M. Zakeeruddin, M. K. Nazeeruddin, M. Grätzel, *ACS Nano* **2015**, *9*, 4200.
- [68] S. P. Sreenilayam, É. McCarthy, K. Fleischer, S. Goodnick, S. Bowden, C. Honsberg, D. Brabazon, In *Micro and NanoTechnologies* (Eds.: S. Thomas, Y. Grohens, G. Vignaud, N. Kalarikkal, J. B. T.-N.-O. James), Elsevier, New York **2020**, pp. 337–345.
- [69] H. Zhang, M. Kramarenko, J. Osmond, J. Toudert, J. Martorell, *ACS Photonics* **2018**, *5*, 2243.
- [70] C. Gueymard, *Sol. Energy* **2004**, *76*, 423.
- [71] S. Divitt, L. Novotny, *Optica* **2015**, *2*, 95.
- [72] A. Herman, M. Sarrazin, O. Deparis, *New J. Phys.* **2014**, *16*, 013022.
- [73] R. J. Matson, K. A. Emery, R. E. Bird, *Sol. Cells* **1984**, *11*, 105.
- [74] M. Stolterfoht, C. M. Wolff, Y. Amir, A. Paulke, L. Perdigón-Toro, P. Caprioglio, D. Neher, *Energy Environ. Sci.* **2017**, *10*, 1530.
- [75] K. Wang, C. Liu, P. Du, J. Zheng, X. Gong, *Energy Environ. Sci.* **2015**, *8*, 1245.
- [76] Y. Fang, C. Bi, D. Wang, J. Huang, *ACS Energy Lett.* **2017**, *2*, 782.
- [77] T. Niu, J. Lu, R. Munir, J. Li, D. Barrit, X. Zhang, H. Hu, Z. Yang, A. Amassian, K. Zhao, S. (Frank) Liu, *Adv. Mater.* **2018**, *30*, 1706576.
- [78] F. Zhang, W. Shi, J. Luo, N. Pellet, C. Yi, X. Li, X. Zhao, T. J. S. Dennis, X. Li, S. Wang, Y. Xiao, S. M. Zakeeruddin, D. Bi, M. Grätzel, *Adv. Mater.* **2017**, *29*, 1606806.
- [79] X. Liu, F. Lin, C.-C. Chueh, Q. Chen, T. Zhao, P.-W. Liang, Z. Zhu, Y. Sun, A. K.-Y. Jen, *Nano Energy* **2016**, *30*, 417.
- [80] F. Wu, T. Chen, X. Yue, L. Zhu, *Org. Electron.* **2018**, *58*, 6.
- [81] J. C. Yu, S. Badgujar, E. D. Jung, V. K. Singh, D. W. Kim, J. Gierschner, E. Lee, Y. S. Kim, S. Cho, M. S. Kwon, M. H. Song, *Adv. Mater.* **2019**, *31*, 1805554.
- [82] J. Xu, A. Buin, A. H. Ip, W. Li, O. Voznyy, R. Comin, M. Yuan, S. Jeon, Z. Ning, J. J. McDowell, P. Kanjanaboos, J.-P. Sun, X. Lan, L. N. Quan, D. H. Kim, I. G. Hill, P. Maksymovych, E. H. Sargent, *Nat. Commun.* **2015**, *6*, 7081.
- [83] J. Zhen, W. Zhou, M. Chen, B. Li, L. Jia, M. Wang, S. Yang, *J. Mater. Chem. A* **2019**, *7*, 2754.
- [84] S. Foster, F. Deledalle, A. Mitani, T. Kimura, K.-B. Kim, T. Okachi, T. Kirchartz, J. Oguma, K. Miyake, J. R. Durrant, S. Doi, J. Nelson, *Adv. Energy Mater.* **2014**, *4*, 1400311.
- [85] Q. Wang, Y. Shao, Q. Dong, Z. Xiao, Y. Yuan, J. Huang, *Energy Environ. Sci.* **2014**, *7*, 2359.
- [86] J. Leng, J. Liu, J. Zhang, S. Jin, *J. Phys. Chem. Lett.* **2016**, *7*, 5056.
- [87] J. Jiménez-López, B. M. D. Puscher, D. M. Guldi, E. Palomares, *J. Am. Chem. Soc.* **2020**, *142*, 1236.
- [88] X. Li, M. Ibrahim Dar, C. Yi, J. Luo, M. Tschumi, S. M. Zakeeruddin, M. K. Nazeeruddin, H. Han, M. Grätzel, *Nat. Chem.* **2015**, *7*, 703.
- [89] Y.-N. Zhang, B. Li, L. Fu, L.-W. Yin, *J. Power Sources* **2019**, *419*, 27.

- [90] W. Xu, L. Zheng, T. Zhu, L. Liu, X. Gong, *ACS Appl. Mater. Interfaces* **2019**, *11*, 34020.
- [91] L. Zhu, C. Chen, F. Li, Z. Shen, Y. Weng, Q. Huang, M. Wang, *J. Mater. Chem. A* **2019**, *7*, 1124.
- [92] J. Shao, S. Yang, Y. Liu, *ACS Appl. Mater. Interfaces* **2017**, *9*, 16202.
- [93] Z. Liu, T. He, H. Wang, S. M. Jain, K. Liu, J. Yang, N. Zhang, H. Liu, M. Yuan, *J. Power Sources* **2018**, *401*, 303.
- [94] I. Zimmermann, P. Gratia, D. Martineau, G. Grancini, J.-N. Audinot, T. Wirtz, M. K. Nazeeruddin, *J. Mater. Chem. A* **2019**, *7*, 8073.
- [95] C. Chen, Y. Zhai, F. Li, F. Tan, G. Yue, W. Zhang, M. Wang, *J. Power Sources* **2017**, *341*, 396.
- [96] S. Wang, A. Wang, X. Deng, L. Xie, A. Xiao, C. Li, Y. Xiang, T. Li, L. Ding, F. Hao, *J. Mater. Chem. A* **2020**, *8*, 12201.
- [97] J. M. Ball, A. Petrozza, *Nat. Energy* **2016**, *1*, 16149.
- [98] F. Gao, Y. Zhao, X. Zhang, J. You, *Adv. Energy Mater.* **2020**, *10*, 1902650.
- [99] C.-H. Chiang, C.-G. Wu, *Nat. Photonics* **2016**, *10*, 196.
- [100] Y.-D. Wang, Y. Wang, J.-Y. Shao, Y. Lan, Z.-R. Lan, Y.-W. Zhong, Y. Song, *ACS Energy Lett.* **2021**, *6*, 2030.
- [101] T. Wu, Y. Wang, X. Li, Y. Wu, X. Meng, D. Cui, X. Yang, L. Han, *Adv. Energy Mater.* **2019**, *9*, 1803766.
- [102] F. Zhang, D. Bi, N. Pellet, C. Xiao, Z. Li, J. J. Berry, S. M. Zakeeruddin, K. Zhu, M. Grätzel, *Energy Environ. Sci.* **2018**, *11*, 3480.
- [103] Y. Shao, Y. Fang, T. Li, Q. Wang, Q. Dong, Y. Deng, Y. Yuan, H. Wei, M. Wang, A. Gruverman, J. Shield, J. Huang, *Energy Environ. Sci.* **2016**, *9*, 1752.
- [104] B. Liu, R. Cui, H. Huang, X. Guo, J. Dong, H. Yao, Y. Li, D. Zhao, J. Wang, J. Zhang, Y. Chen, B. Sun, *J. Mater. Chem. A* **2020**, *8*, 3145.
- [105] R. Sandoval-Torrientes, J. Pascual, I. García-Benito, S. Collavini, I. Kosta, R. Tena-Zaera, N. Martín, J. L. Delgado, *ChemSusChem* **2017**, *10*, 2023.
- [106] C.-Y. Chang, C.-P. Wang, R. Raja, L. Wang, C.-S. Tsao, W.-F. Su, *J. Mater. Chem. A* **2018**, *6*, 4179.
- [107] N. Aristidou, C. Eames, I. Sanchez-Molina, X. Bu, J. Kosco, M. S. Islam, S. A. Haque, *Nat. Commun.* **2017**, *8*, 15218.
- [108] N. Aristidou, I. Sanchez-Molina, T. Chotchuangchutchaval, M. Brown, L. Martinez, T. Rath, S. A. Haque, *Angew. Chem., Int. Ed.* **2015**, *54*, 8208.
- [109] C.-T. Lin, S. Pont, J. Kim, T. Du, S. Xu, X. Li, D. Bryant, M. A. McLachlan, J. R. Durrant, *Sustain. Energy Fuels* **2018**, *2*, 1686.
- [110] Y. Wu, X. Yang, W. Chen, Y. Yue, M. Cai, F. Xie, E. Bi, A. Islam, L. Han, *Nat. Energy* **2016**, *1*, 16148.
- [111] G. Xu, R. Xue, W. Chen, J. Zhang, M. Zhang, H. Chen, C. Cui, H. Li, Y. Li, Y. Li, *Adv. Energy Mater.* **2018**, *8*, 1703054.
- [112] K.-H. Hu, Z.-K. Wang, L. Meng, K.-L. Wang, Y. Zhang, L.-S. Liao, *J. Mater. Chem. C* **2019**, *7*, 6391.
- [113] Y. Tu, J. Wu, X. He, P. Guo, T. Wu, H. Luo, Q. Liu, Q. Wu, J. Lin, M. Huang, Z. Lan, S. Li, *J. Mater. Chem. A* **2017**, *5*, 21161.
- [114] J. Han, X. Yin, Y. Zhou, H. Nan, Y. Gu, M. Tai, J. Li, H. Lin, *ACS Appl. Mater. Interfaces* **2018**, *10*, 42328.
- [115] S. R. Ha, W. H. Jeong, Y. Liu, J. T. Oh, S. Y. Bae, S. Lee, J. W. Kim, S. Bandyopadhyay, H. I. Jeong, J. Y. Kim, Y. Kim, M. H. Song, S. H. Park, S. D. Stranks, B. R. Lee, R. H. Friend, H. Choi, *J. Mater. Chem. A* **2020**, *8*, 1326.
- [116] Y. Wu, P. Wang, S. Wang, Z. Wang, B. Cai, X. Zheng, Y. Chen, N. Yuan, J. Ding, W.-H. Zhang, *ChemSusChem* **2018**, *11*, 837.
- [117] P. Chen, E. Wang, X. Yin, H. Xie, M. Que, B. Gao, W. Que, *J. Colloid Interface Sci.* **2018**, *532*, 182.
- [118] Y. Liu, I. Shin, I.-W. Hwang, S. Kim, J. Lee, M.-S. Yang, Y. K. Jung, J.-W. Jang, J. H. Jeong, S. H. Park, K. H. Kim, *ACS Appl. Mater. Interfaces* **2017**, *9*, 12382.
- [119] C. Li, J. Sleppy, N. Dhasmana, M. Soliman, L. Tetard, J. Thomas, *J. Mater. Chem. A* **2016**, *4*, 11648.
- [120] A. Mahata, E. Mosconi, D. Meggiolaro, F. De Angelis, *Chem. Mater.* **2020**, *32*, 105.
- [121] Q. Fu, S. Xiao, X. Tang, Y. Chen, T. Hu, *ACS Appl. Mater. Interfaces* **2019**, *11*, 24782.
- [122] A. Morales-Acevedo, *Energy Procedia* **2010**, *2*, 169.
- [123] M. Troviano, K. Taretto, *Sol. Energy Mater. Sol. Cells* **2011**, *95*, 821.
- [124] O. Lundberg, M. Edoff, L. Stolt, *Thin Solid Films* **2005**, *480–481*, 520.
- [125] J. Mandelkorn, J. H. Lamneck, *Sol. Cells* **1990**, *29*, 121.
- [126] J. G. Fossum, *IEEE Trans. Electron Devices* **1977**, *24*, 322.
- [127] J. Ma, M. Zheng, C. Chen, Z. Zhu, X. Zheng, Z. Chen, Y. Guo, C. Liu, Y. Yan, G. Fang, *Adv. Funct. Mater.* **2018**, *28*, 1804128.
- [128] J. Liu, S. Pathak, T. Stergiopoulos, T. Leijtens, K. Wojciechowski, S. Schumann, N. Kausch-Busies, H. J. Snaith, *J. Phys. Chem. Lett.* **2015**, *6*, 1666.
- [129] S. N. Habisreutinger, T. Leijtens, G. E. Eperon, S. D. Stranks, R. J. Nicholas, H. J. Snaith, *Nano Lett.* **2014**, *14*, 5561.
- [130] C. Xiao, F. Zhang, Z. Li, S. P. Harvey, X. Chen, K. Wang, C.-S. Jiang, K. Zhu, M. Al-Jassim, *Matter* **2020**, *2*, 261.
- [131] H. Taherianfard, G.-W. Kim, F. Ebadi, T. Abzieher, K. Choi, U. W. Paetzold, B. S. Richards, A. Alrhmman Eliwi, F. Tajabadi, N. Taghavinia, M. Malekshahi Byranvand, *ACS Appl. Mater. Interfaces* **2019**, *11*, 44802.
- [132] Z. Li, J. Park, H. Park, J. Lee, Y. Kang, T. K. Ahn, B.-G. Kim, H. J. Park, *Nano Energy* **2020**, *78*, 105159.
- [133] H. Kanda, N. Shibayama, A. J. Huckaba, Y. Lee, S. Paek, N. Klipfel, C. Roldán-Carmona, V. I. E. Queloz, G. Grancini, Y. Zhang, M. Abuhelaiqa, K. T. Cho, M. Li, M. D. Mensi, S. Kinge, M. K. Nazeeruddin, *Energy Environ. Sci.* **2020**, *13*, 1222.
- [134] Y. Zhou, H. Zhong, J. Han, M. Tai, X. Yin, M. Zhang, Z. Wu, H. Lin, *J. Mater. Chem. A* **2019**, *7*, 26334.
- [135] A. Rajagopal, P.-W. Liang, C.-C. Chueh, Z. Yang, A. K.-Y. Jen, *ACS Energy Lett.* **2017**, *2*, 2531.
- [136] S. Zhang, Z. Hu, J. Zhang, X. Jia, J. Jiang, Y. Chen, B. Lin, H. Jiang, B. Fang, N. Yuan, J. Ding, *J. Power Sources* **2019**, *438*, 226987.
- [137] K. Ji, J. Yuan, F. Li, Y. Shi, X. Ling, X. Zhang, Y. Zhang, H. Lu, J. Yuan, W. Ma, *J. Mater. Chem. A* **2020**, *8*, 8104.
- [138] J. Wang, J. Zhang, Y. Zhou, H. Liu, Q. Xue, X. Li, C.-C. Chueh, H.-L. Yip, Z. Zhu, A. K. Y. Jen, *Nat. Commun.* **2020**, *11*, 177.
- [139] J. Ryu, K. Lee, J. Yun, H. Yu, J. Lee, J. Jang, *Small* **2017**, *13*, 1701225.
- [140] H. Bian, D. Bai, Z. Jin, K. Wang, L. Liang, H. Wang, J. Zhang, Q. Wang, S. (Frank) Liu, *Joule* **2018**, *2*, 1500.
- [141] M. Hao, Y. Bai, S. Zeiske, L. Ren, J. Liu, Y. Yuan, N. Zarrabi, N. Cheng, M. Ghasemi, P. Chen, M. Lyu, D. He, J.-H. Yun, Y. Du, Y. Wang, S. Ding, A. Armin, P. Meredith, G. Liu, H.-M. Cheng, L. Wang, *Nat. Energy* **2020**, *5*, 79.
- [142] X. Ling, S. Zhou, J. Yuan, J. Shi, Y. Qian, B. W. Larson, Q. Zhao, C. Qin, F. Li, G. Shi, C. Stewart, J. Hu, X. Zhang, J. M. Luther, S. Duhm, W. Ma, *Adv. Energy Mater.* **2019**, *9*, 1900721.
- [143] H. Zai, C. Zhu, H. Xie, Y. Zhao, C. Shi, Z. Chen, X. Ke, M. Sui, C. Chen, J. Hu, Q. Zhang, Y. Gao, H. Zhou, Y. Li, Q. Chen, *ACS Energy Lett.* **2018**, *3*, 30.
- [144] X. Zheng, J. Troughton, N. Gasparini, Y. Lin, M. Wei, Y. Hou, J. Liu, K. Song, Z. Chen, C. Yang, B. Turedi, A. Y. Alsalloum, J. Pan, J. Chen, A. A. Zhumekenov, T. D. Anthopoulos, Y. Han, D. Baran, O. F. Mohammed, E. H. Sargent, O. M. Bakr, *Joule* **2019**, *3*, 1963.
- [145] Y. Zhang, H. Yang, M. Chen, N. P. Padture, O. Chen, Y. Zhou, *Adv. Energy Mater.* **2019**, *9*, 1900243.
- [146] Q. Zhao, A. Hazarika, X. Chen, S. P. Harvey, B. W. Larson, G. R. Teeter, J. Liu, T. Song, C. Xiao, L. Shaw, M. Zhang, G. Li, M. C. Beard, J. M. Luther, *Nat. Commun.* **2019**, *10*, 2842.
- [147] M. Que, Z. Dai, H. Yang, H. Zhu, Y. Zong, W. Que, N. P. Padture, Y. Zhou, O. Chen, *ACS Energy Lett.* **2019**, *4*, 1970.
- [148] S. Akin, Y. Altintas, E. Mutlugun, S. Sonmezoglu, *Nano Energy* **2019**, *60*, 557.

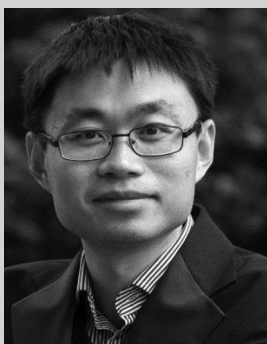
- [149] B. Li, Y. Zhang, L. Zhang, L. Yin, *Adv. Mater.* **2017**, *29*, 1701221.
- [150] C. Liu, M. Hu, X. Zhou, J. Wu, L. Zhang, W. Kong, X. Li, X. Zhao, S. Dai, B. Xu, C. Cheng, *NPG Asia Mater* **2018**, *10*, 552.
- [151] A. Waleed, M. M. Tavakoli, L. Gu, S. Hussain, D. Zhang, S. Poddar, Z. Wang, R. Zhang, Z. Fan, *Nano Lett.* **2017**, *17*, 4951.
- [152] K. T. Cho, S. Paek, G. Grancini, C. Roldán-Carmona, P. Gao, Y. Lee, M. K. Nazeeruddin, *Energy Environ. Sci.* **2017**, *10*, 621.
- [153] D. Luo, W. Yang, Z. Wang, A. Sadhanala, Q. Hu, R. Su, R. Shivanna, G. F. Trindade, J. F. Watts, Z. Xu, T. Liu, K. Chen, F. Ye, P. Wu, L. Zhao, J. Wu, Y. Tu, Y. Zhang, X. Yang, W. Zhang, R. H. Friend, Q. Gong, H. J. Snaith, R. Zhu, *Science* **2018**, *360*, 1442.
- [154] J. C. Yu, J. A. Hong, E. D. Jung, D. Bin Kim, S.-M. Baek, S. Lee, S. Cho, S. S. Park, K. J. Choi, M. H. Song, *Sci. Rep.* **2018**, *8*, 1070.
- [155] X. Zheng, Y. Hou, C. Bao, J. Yin, F. Yuan, Z. Huang, K. Song, J. Liu, J. Troughton, N. Gasparini, C. Zhou, Y. Lin, D.-J. Xue, B. Chen, A. K. Johnston, N. Wei, M. N. Hedhili, M. Wei, A. Y. Alsalloum, P. Maity, B. Turedi, C. Yang, D. Baran, T. D. Anthopoulos, Y. Han, Z.-H. Lu, O. F. Mohammed, F. Gao, E. H. Sargent, O. M. Bakr, *Nat. Energy* **2020**, *5*, 131.
- [156] C. Chen, Z. Song, C. Xiao, D. Zhao, N. Shrestha, C. Li, G. Yang, F. Yao, X. Zheng, R. J. Ellingson, C.-S. Jiang, M. Al-Jassim, K. Zhu, G. Fang, Y. Yan, *Nano Energy* **2019**, *61*, 141.
- [157] C. Wang, C. Xiao, Y. Yu, D. Zhao, R. A. Awni, C. R. Grice, K. Ghimire, I. Constantinou, W. Liao, A. J. Cimaroli, P. Liu, J. Chen, N. J. Podraza, C.-S. Jiang, M. M. Al-Jassim, X. Zhao, Y. Yan, *Adv. Energy Mater.* **2017**, *7*, 1700414.
- [158] C. Xiao, C. Wang, W. Ke, B. P. Gorman, J. Ye, C.-S. Jiang, Y. Yan, M. M. Al-Jassim, *ACS Appl. Mater. Interfaces* **2017**, *9*, 38373.
- [159] H. Sun, K. Deng, J. Xiong, L. Li, *Adv. Energy Mater.* **2020**, *10*, 1903347.
- [160] C. Wang, Z. Song, C. Li, D. Zhao, Y. Yan, *Adv. Funct. Mater.* **2019**, *29*, 1808801.
- [161] Y. Hu, J. Schlipf, M. Wussler, M. L. Petrus, W. Jaegermann, T. Bein, P. Müller-Buschbaum, P. Docampo, *ACS Nano* **2016**, *10*, 5999.
- [162] R. J. E. Westbrook, W. Xu, X. Liang, T. Webb, T. M. Clarke, S. A. Haque, *J. Phys. Chem. Lett.* **2021**, *12*, 3312.
- [163] F. Wang, W. Geng, Y. Zhou, H.-H. Fang, C.-J. Tong, M. A. Loi, L.-M. Liu, N. Zhao, *Adv. Mater.* **2016**, *28*, 9986.
- [164] K. T. Cho, G. Grancini, Y. Lee, E. Oveisi, J. Ryu, O. Almora, M. Tschumi, P. A. Schouwink, G. Seo, S. Heo, J. Park, J. Jang, S. Paek, G. Garcia-Belmonte, M. K. Nazeeruddin, *Energy Environ. Sci.* **2018**, *11*, 952.
- [165] Y. Bai, S. Xiao, C. Hu, T. Zhang, X. Meng, H. Lin, Y. Yang, S. Yang, *Adv. Energy Mater.* **2017**, *7*, 1701038.
- [166] S. Gharibzadeh, B. Abdollahi Nejand, M. Jakoby, T. Abzieher, D. Hauschild, S. Moghadamzadeh, J. A. Schwenzler, P. Brenner, R. Schmager, A. A. Haghighirad, L. Weinhardt, U. Lemmer, B. S. Richards, I. A. Howard, U. W. Paetzold, *Adv. Energy Mater.* **2019**, *9*, 1803699.
- [167] Q. Jiang, Y. Zhao, X. Zhang, X. Yang, Y. Chen, Z. Chu, Q. Ye, X. Li, Z. Yin, J. You, *Nat. Photonics* **2019**, *13*, 460.
- [168] E. H. Jung, N. J. Jeon, E. Y. Park, C. S. Moon, T. J. Shin, T.-Y. Yang, J. H. Noh, J. Seo, *Nature* **2019**, *567*, 511.
- [169] B. Li, Y. Xiang, K. D. G. Imalka Jayawardena, D. Luo, Z. Wang, X. Yang, J. F. Watts, S. Hinder, M. T. Sajjad, T. Webb, H. Luo, I. Marko, H. Li, S. A. J. Thomson, R. Zhu, G. Shao, S. J. Sweeney, S. R. P. Silva, W. Zhang, *Nano Energy* **2020**, *78*, 105249.
- [170] S. Yang, J. Dai, Z. Yu, Y. Shao, Y. Zhou, X. Xiao, X. C. Zeng, J. Huang, *J. Am. Chem. Soc.* **2019**, *141*, 5781.
- [171] J. J. Yoo, G. Seo, M. R. Chua, T. G. Park, Y. Lu, F. Rotermund, Y.-K. Kim, C. S. Moon, N. J. Jeon, J.-P. Correa-Baena, V. Bulović, S. S. Shin, M. G. Bawendi, J. Seo, *Nature* **2021**, *590*, 587.
- [172] M. Hadadian, J.-H. Smätt, J.-P. Correa-Baena, *Energy Environ. Sci.* **2020**, *13*, 1377.
- [173] D. H. Cao, C. C. Stoumpos, O. K. Farha, J. T. Hupp, M. G. Kanatzidis, *J. Am. Chem. Soc.* **2015**, *137*, 7843.
- [174] I. C. Smith, E. T. Hoke, D. Solis-Ibarra, M. D. McGehee, H. I. Karunadasa, *Angew. Chem., Int. Ed.* **2014**, *53*, 11232.
- [175] F. Zhang, H. Lu, J. Tong, J. J. Berry, M. C. Beard, K. Zhu, *Energy Environ. Sci.* **2020**, *13*, 1154.
- [176] N. Li, Z. Zhu, C.-C. Chueh, H. Liu, B. Peng, A. Petrone, X. Li, L. Wang, A. K.-Y. Jen, *Adv. Energy Mater.* **2017**, *7*, 1601307.
- [177] J. Zhao, Y. Deng, H. Wei, X. Zheng, Z. Yu, Y. Shao, J. E. Shield, J. Huang, *Sci. Adv.* **2017**, *3*, eaao5616.
- [178] Y. Zhou, F. Wang, Y. Cao, J.-P. Wang, H.-H. Fang, M. A. Loi, N. Zhao, C.-P. Wong, *Adv. Energy Mater.* **2017**, *7*, 1701048.
- [179] Y. Lin, Y. Bai, Y. Fang, Z. Chen, S. Yang, X. Zheng, S. Tang, Y. Liu, J. Zhao, J. Huang, *J. Phys. Chem. Lett.* **2018**, *9*, 654.
- [180] Y. Kato, L. K. Ono, M. V Lee, S. Wang, S. R. Raga, Y. Qi, *Adv. Mater. Interfaces* **2015**, *2*, 1500195.
- [181] G. Grancini, C. Roldán-Carmona, I. Zimmermann, E. Mosconi, X. Lee, D. Martineau, S. Narbey, F. Oswald, F. De Angelis, M. Graetzel, M. K. Nazeeruddin, *Nat. Commun.* **2017**, *8*, 15684.
- [182] Y. Wei, H. Chu, Y. Tian, B. Chen, K. Wu, J. Wang, X. Yang, B. Cai, Y. Zhang, J. Zhao, *Adv. Energy Mater.* **2019**, *9*, 1900612.
- [183] J. Qing, X.-K. Liu, M. Li, F. Liu, Z. Yuan, E. Tiukalova, Z. Yan, M. Duchamp, S. Chen, Y. Wang, S. Bai, J.-M. Liu, H. J. Snaith, C.-S. Lee, T. C. Sum, F. Gao, *Adv. Energy Mater.* **2018**, *8*, 1800185.
- [184] C. Zuo, A. D. Scully, W. L. Tan, F. Zheng, K. P. Ghiggino, D. Vak, H. Weerasinghe, C. R. McNeill, D. Angmo, A. S. R. Chesman, M. Gao, *Commun. Mater.* **2020**, *1*, 33.
- [185] S. P. Harvey, J. Messinger, K. Zhu, J. M. Luther, J. J. Berry, *Adv. Energy Mater.* **2020**, *10*, 1903674.
- [186] S. P. Harvey, F. Zhang, A. Palmstrom, J. M. Luther, K. Zhu, J. J. Berry, *ACS Appl. Mater. Interfaces* **2019**, *11*, 30911.
- [187] Y. Zhong, M. Hufnagel, M. Thelakkat, C. Li, S. Huettner, *Adv. Funct. Mater.* **2020**, *30*, 1908920.
- [188] J. M. Hoffman, J. Strzalka, N. C. Flanders, I. Hadar, S. A. Cuthriell, Q. Zhang, R. D. Schaller, W. R. Dichtel, L. X. Chen, M. G. Kanatzidis, *Adv. Mater.* **2020**, *32*, 2002812.
- [189] P. Cui, D. Wei, J. Ji, H. Huang, E. Jia, S. Dou, T. Wang, W. Wang, M. Li, *Nat. Energy* **2019**, *4*, 150.
- [190] S. A. L. Weber, I. M. Hermes, S.-H. Turren-Cruz, C. Gort, V. W. Bergmann, L. Gilson, A. Hagfeldt, M. Graetzel, W. Tress, R. Berger, *Energy Environ. Sci.* **2018**, *11*, 2404.
- [191] V. W. Bergmann, S. A. L. Weber, F. Javier Ramos, M. K. Nazeeruddin, M. Grätzel, D. Li, A. L. Domanski, I. Lieberwirth, S. Ahmad, R. Berger, *Nat. Commun.* **2014**, *5*, 5001.
- [192] R. J. E. Westbrook, D. I. Sanchez-Molina, D. J. Manuel Marin-Beloqui, D. H. Bronstein, D. S. A. Haque, *J. Phys. Chem. C* **2018**, *122*, 1326.
- [193] B. Philippe, T. J. Jacobsson, J.-P. Correa-Baena, N. K. Jena, A. Banerjee, S. Chakraborty, U. B. Cappel, R. Ahuja, A. Hagfeldt, M. Odelius, H. Rensmo, *J. Phys. Chem. C* **2017**, *121*, 26655.
- [194] J. Lischner, S. Nemsák, G. Conti, A. Gloskovskii, G. K. Pálsson, C. M. Schneider, W. Drube, S. G. Louie, C. Fadley, *J. Appl. Phys.* **2016**, *119*, 165703.
- [195] E. A. Kraut, R. W. Grant, J. R. Waldrop, S. P. Kowalczyk, *Phys. Rev. Lett.* **1980**, *44*, 1620.
- [196] T. R. Hopper, A. Gorodetsky, J. M. Frost, C. Müller, R. Lovrincic, A. A. Bakulin, *ACS Energy Lett.* **2018**, *3*, 2199.
- [197] K. D. G. I. Jayawardena, R. M. I. Bandara, M. Monti, E. Butler-Caddle, T. Pichler, H. Shiozawa, Z. Wang, S. Jenatsch, S. J. Hinder, M. G. Masteghin, M. Patel, H. M. Thirimanne, W. Zhang, R. A. Sporea, J. Lloyd-Hughes, S. R. P. Silva, *J. Mater. Chem. A* **2020**, *8*, 693.
- [198] L. L. Lanzetta, T. Webb, N. Zibouche, X. Liang, D. Ding, G. Min, R. Westbrook, B. Gaggio, T. Macdonald, M. S. Islam, S. Haque, *Nat. Commun.* **2021**, *12*, 2853.
- [199] T. Kirchartz, D. Cahen, *Nat. Energy* **2020**, *5*, 973.



Thomas Webb, received his Chemistry M.Sc. degree from Imperial College London under the supervision of Professor Saif Haque. He is currently a Ph.D. candidate at the Advanced Technology Institute part of the University of Surrey under the supervision of Dr. Wei Zhang and Professor Stephen J. Sweeney. His research interests focus on heterojunction engineering and enabling commercialization of perovskite solar cells.



Stephen J. Sweeney, is a Professor of Physics based in the Advanced Technology Institute at the University of Surrey. He obtained his Ph.D. in Semiconductor Laser Physics from the University of Surrey. His research interests focus on the characterization and development of novel semiconductor and photonic materials for applications in devices for applications in communications, energy and sensing. Current areas of focus include mid-infrared photonics, photovoltaic technologies and low-cost, high-performance photonic devices.



Wei Zhang, is a senior lecturer in Energy Technology at the Advanced Technology Institute, University of Surrey. He obtained his Ph.D. at the Department of Chemical and Biomolecular Engineering, National University of Singapore (Singapore), working on dye-sensitized solar cells. His current research interest includes high-efficiency and low-cost perovskite photovoltaics, functional nanomaterials (low-dimensional semiconducting metal oxides, plasmonic materials, and photonic crystals), and prospective materials for energy conversion and storage applications.